The Astronomical Journal, 171:289 (34pp), 2026 May https://doi.org/10.3847/1538-3881/ae5109

Here Be SDRAGNs—Spiral Galaxies Hosting Large Double Radio Sources

Jean Tate[1,14], William C. Keel[2], Michael O'Keeffe[2,15], O. Ivy Wong[3,4], Heinz Andernach[5,16], Julie K. Banfield[6], Alexei Moiseev[7], Aleksandrina Smirnova[7], Arina Arshinova[7], Eugene Malygin[7], Elena Shablovinskaya[8], Roman Uklein[7], Stanislav Shabala[9], Ray Norris[10,11], Brooke D. Simmons[12], Rebecca Smethurst[13], Ivan Terentev[1], Chris Molloy[1], and Victor Linares[1]

[1] Radio Galaxy Zoo
[2] Dept. of Physics and Astronomy, University of Alabama, Box 870324, Tuscaloosa, AL 35404, USA; wkeel@ua.edu
[3] CSIRO Space & Astronomy, PO Box 1130, Bentley, WA 6102, Australia
[4] ICRAR-M468, University of Western Australia, Crawley, WA 6009, Australia
[5] Thüringer Landessternwarte, Sternwarte 5, D-07778 Tautenburg, Germany
[6] Research School of Astronomy and Astrophysics, Australian National University, Canberra, ACT 2611, Australia
[7] Special Astrophysical Observatory, Nizhny Arkhyz, Russia
[8] Humboldt Research Fellow, Max Planck Institute for Radio Astronomy, Auf dem Hügel 69, D–53121, Bonn, Germany
[9] School of Mathematics and Physics, University of Tasmania, Private Bag 37, Hobart, TAS 7001, Australia
[10] CSIRO Space & Astronomy, PO Box 76, Epping, NSW 1710, Australia
[11] School of Science, Western Sydney University, Locked Bag 1797, Penrith, NSW 2751, Australia
[12] Physics, Lancaster University, Lancaster, LA1 4YB, UK
[13] Department of Physics, University of Oxford, Denys Wilkinson Building, Keble Road, Oxford, OX1 3RH, UK

Received 2025 September 28; revised 2026 March 6; accepted 2026 March 6; published 2026 April 14

Abstract

We present a sample of large double radio sources hosted by spiral galaxies (spiral double radio active galactic nuclei, SDRAGNs). Candidates were initially selected through the Radio Galaxy Zoo project and subsequently refined using Sloan Digital Sky Survey images. The most promising were targeted in the Zoo Gems Hubble Space Telescope (HST) program, yielding images for 36 candidates. We assess the likelihood that each spiral galaxy is the genuine host of the radio emission, finding 15 new high-probability SDRAGNs. The hosts are seen preferentially close to edge-on. SDRAGNs predominantly show type II Fanaroff–Riley (FR II) radio structures and optical pseudobulges. After accounting for sample selection effects, the radio-jet axes lie preferentially near the poles of the galactic disks; we find a constant probability distribution for intrinsic pole–jet angles $\phi < 30°$, declining to zero at $\phi = 60°$. We have obtained optical spectra for all these newly identified SDRAGNs. Among both previously known and new SDRAGN samples, 8/25 show Seyfert 2 signatures, 6/25 show central star formation, and 5/25 show low-ionization nuclear emission-line region emission strong enough to indicate active galactic nuclei (AGN) activity or shock ionization, broadly similar to radio galaxies in elliptical hosts but with the addition of star formation (diluting or masking weak AGN signatures). SDRAGNs include FR II sources seen at unusually low radio powers, and preferentially occur in significant galaxy overdensities on 1 Mpc scales. Our "false alarms"—systems where HST data show the spiral is not the actual host galaxy—include radio sources seen through large portions of foreground spiral disks, potentially providing useful probes for Faraday rotation studies of disk magnetic fields.

Unified Astronomy Thesaurus concepts: AGN host galaxies (2017); Extragalactic radio sources (508); Spiral galaxies (1560)

Materials only available in the online version of record: machine-readable table

1. Introduction

Giant, massive elliptical galaxies are by far the most common hosts of large-scale, double-lobed radio sources in the local Universe, as shown in numerous studies, from T. A. Matthews et al. (1964) to P. N. Best et al. (2005). Many of these nominally elliptical hosts show morphological features—twisted dust lanes, shells, tails, boxy or twisted and nonconcentric isophotes—indicating recent interactions or merging events, which give plausible ways to channel material to the nucleus. This has been found statistically (T. M. Heckman et al. 1986; N. Roche & S. A. Eales 2000) and in detailed studies of such individual systems as 3C 293 (W. van Breugel et al. 1984; B. H. C. Emonts et al. 2009), 3C 305 (A. Sandage 1966; T. M. Heckman et al. 1982; S. de Koff et al. 2000; N. Jackson et al. 2003), 3C 40 (NGC 547; G. Fasano et al. 1996), 3C 223.0 (E. P. Smith & T. M. Heckman 1989) and 3C 285 (N. Roche &

---

[14] Deceased 2020 November 6. Jean Tate was among the most active volunteers in Galaxy Zoo and Radio Galaxy Zoo, the one whose particular interest in SDRAGNs set the stage for these results. Jean's work set a high standard for the professional astronomers in the project, maintaining online material in such good order that we were able to continue to retrieve and understand even work left in progress. Much of the wording in the first two sections traces back to an SDRAGN draft Jean wrote before the HST observations were approved.

[15] Current address: Social Learning Lab, Stanford University, Stanford, CA 94305, USA.

[16] Permanent address: Universidad de Guanajuato, Departamento de Astronomía, Callejón de Jalisco s/n. Guanajuato 36023, Mexico.

S. A. Eales 2000), as well as the numerous studies of Centaurus A (NGC 5128). We follow J. P. Leahy (1993) in calling these double radio sources associated with galactic nuclei (DRAGNs).

The strong contrast in host galaxies between active galactic nuclei (AGNs) accompanied by large double radio sources and those without such sources, though they may have core emission and jets on smaller scales (that is, within the galaxies), has focused attention on the handful of spiral galaxies hosting large double sources. Beyond the way they stand out in surveys of host galaxies, they might share some set of (rare?) properties which illuminates the conditions needed to produce such large radio jets and lobes. By analogy with DRAGNs, we follow D. D. Mulcahy et al. (2016) and M. Y. Mao et al. (2018) in calling spiral hosts of such double radio sources spiral double radio active galactic nuclei (SDRAGNs). This possibility motivated us to seek possible spiral hosts among radio sources identified in the Radio Galaxy Zoo project (RGZ; J. K. Banfield et al. 2015), and to include some of the best candidates in a Hubble Space Telescope (HST) program of short-exposure imaging, to clarify these galaxies' structures. This paper reports the results, beginning with the construction of a candidate list from RGZ, followed by its winnowing using ground-based imaging surveys, selection for HST imaging, and finally the results of those HST observations and supporting optical spectroscopy.

We concentrate on galaxies whose radio emission extends well beyond the usual bounds of the galaxy's starlight. Small-scale double radio sources are seen around Seyfert nuclei in spiral galaxies (N. M. Nagar et al. 1999; S. Kaviraj et al. 2015), but on scales much smaller than typically associated with DRAGNs. Among the 12 Seyferts at $z < 0.035$ showing such double sources from data in E. Xanthopoulos et al. (2010), N. M. Nagar et al. (1999), I. M. Mutie et al. (2024), and A. Pedlar et al. (1993), the largest projected size is 8.6 kpc on NGC 526A, with a median of 0.97 kpc. These sources often display bending of the jets and arcuate structure to the lobes, both suggesting strong interaction with the dense interstellar medium (ISM) of spiral hosts. These sources contrast with the sizes of typical DRAGNs, and with the previously identified SDRAGNs. During the RGZ search for SDRAGNs, it proved to be a useful heuristic, in the absence of redshifts for many host galaxies, to look for double radio sources projected outside the extent of the host galaxies as shown on optical and near-IR images. The surface-brightness mapping for display is consistent across all images from each survey, and typical detection radii for even the most luminous spirals seldom exceed 15 kpc. The gap between the largest double sources seen in Seyferts (8.6 kpc total extent end-to-end) and the smallest RGZ SDRAGNs (46 kpc) supports the value of this simple criterion. It also eliminates two-sided radio emission off the disk plane from outflows in spirals driven by either AGNs or star formation (N. Duric & E. R. Seaquist 1988; J. I. Harnett et al. 1990; J. F. Gallimore et al. 2006); the double sources we examine are on much larger scales and much more tightly collimated. This dichotomy has driven speculation that the dense, cool ISM prevalent within the disks and nuclei of spirals can disrupt even relativistic jets before they pass from the ISM to the intergalactic or circumgalactic medium outside, where the jet interacting with these more rarefied surroundings can give rise to the large-scale lobes which are the hallmarks of traditional radio galaxies.

Several broad possibilities might be envisioned for how (only) a few spirals produce double radio sources spanning hundreds of kiloparsecs, some discussed in previous work. One possibility is that these systems could result from the unusually large masses of the central supermassive black holes (SMBHs) for spirals, which might accompany unusually luminous classical bulges. Another straightforward possibility is that SDRAGNs result from fortuitous alignment of the jets with the poles of the host-galaxy disks, such that they encounter minimal column densities of dense ISM (a situation that might be more common in spirals lacking classical bulges and less likely to have undergone major merges, which could change the spin of the SMBH; R. S. Beckmann et al. 2024), which would yield galaxies with pseudobulges rather than classical bulges. Alternatively, SDRAGNs may be favored within particular density regimes of the circumgalactic medium, such that observable radio lobes are produced when jets interact with this material. This last possibility may be probed through the group or tidal environments of SDRAGNs. All of these ideas can be evaluated through detailed study of larger samples, such as the one presented here.

While this manuscript was in preparation, an analysis involving much of the same HST data was published by Z. Wu et al. (2022). We highlight comparisons with their results wherever relevant, and adopt their GALFIT decompositions of the host-galaxy structures. Our final list of high-probability SDRAGNs mostly overlaps with that of Z. Wu et al. (2022), but there are significant differences in our results due to newer HST imaging, improved radio data (including low-frequency surveys), the availability of redshifts from optical spectra, and differing morphological classifications for two systems. We identify 15 high-probability SDRAGNs from the RGZ+HST sample.

2. Sample Selection and Observations

2.1. Known SDRAGNs

The term "SDRAGN" is not completely well defined; generally it refers to a host galaxy with spiral optical morphology and a pair of radio lobes approximately symmetrically located on opposite sides of the host and extending well beyond its optical boundary. In other words, we seek classical DRAGNs, but with a spiral galaxy as host. SDRAGN is an empirical rather than physical definition; for example, hosts with double lobes oriented near the line of sight may have them overlap with the host emission and each other, so from our perspective they may be indistinguishable from radio emission entirely within the optical host, e.g., PKS 1814 −637 (R. Morganti et al. 2011) and PKS 1413+135 (G. Lamer et al. 1999). Among well-known SDRAGNs, the lobes may be completely detached (A. Hota et al. 2011) or connected to the core by a bridge of radio emission (e.g., J1649+2635; M. Y. Mao et al. 2015). We seek evidence of actual spiral structure; the number of lenticular (S0) hosts of large double radio sources is a separate question, perhaps less complicated by the dense, cold interstellar material in spirals but often difficult to distinguish from ellipticals with extended stellar halos, as in Fornax A (NGC 1316). Ambiguity remains in, for example, merger remnants, where tidal features may mimic spiral arms, as seen in such systems as CGCG 292-057 (M. Jamrozy et al. 2011) and NGC 5972 (P. Veron & M.-P. Veron-Cetty 1995, reinforced in that case by AGN

Table 1
Previously Identified SDRAGNs

Name	Identification	z	Sep.	LLS	Optical Spectrum	PA (deg)	Inclination (deg)	Type	References
J0315−1906	2MASX J03155208−1906442	0.0677	126	350	Sy 2	87 ± 1	0.0 ± 0.5	Sb	(1), (2)
J0354−1340	6dFGS gJ035432.8−134008	0.0772	172	177	NLSy1	90 ± 20	80 ± 10	(R)SBa	(3)
J0408−6247	NGC 1534	0.0178	755	755	⋯	79 ± 3	21 ± 2	Sa	(4)
J0725+2957	B2 0722+30	0.0197	2.5	12.5	LINER	142 ± 2	9.8 ± 1.5	Sc	(5), (6)
J0836+0532	SDSS J083655.86+053242.0	0.0993	280	280	Sy 2	70 ± 30	80 ± 10	Sc(s)	(7)
J1350−1634	LEDA 896325	0.0877	517	832	Sy 1.8?	161	27.5 ± 2.0	Sb	(8)
J1409−0302	SDSS J140948.85−030232.5 (Speca)	0.1376	312	1300	LINER	21 ± 2	22 ± 2	Sab	(9)
J1633+3520	NGC 6185	0.0343	1844	2450	LINER	4 ± 4	36 ± 3	Sa	(10)
J1649+2635	SDSS J164924.01+263502.5	0.0545	60	85	LINER	120 ± 12	57 ± 5	Sc	(11), (12)
J2318+4314	MCG +07-47-10	0.0169	168	207	SF	235 ± 5	(80 ± 10)	SBc	(13)
J2345−0449	2MASX J23453268−0449256	0.0755	1320	1600	LINER	98 ± 3	24 ± 2	Sb	(14), (15)

References. (1) M. J. Ledlow et al. (2001); (2). W. C. Keel et al. (2006); (3) A. Vietri et al. (2022); (4) N. Hurley-Walker et al. (2015); (5) A. Capetti et al. (2000); (6) B. H. C. Emonts et al. (2009); (7) V. Singh et al. (2015); (8) S. Sethi et al. (2025); (9) A. Hota et al. (2011); (10) M. S. S. L. Oei et al. (2023); (11) M. Y. Mao et al. (2015); (12) V. Singh et al. (2015); (13) D. D. Mulcahy et al. (2016); (14) J. Bagchi et al. (2014); (15) J. Bagchi et al. (2025).

Note. "Sep." denotes the peak-to-peak separation of radio lobes, projected on the sky, in kiloparsecs. "LLS" (largest linear size) is the largest projected size from available radio data, also in kiloparsecs, omitting relic or outer double structure detected at low frequencies. The column "Optical Spectrum" shows the emission-line classification of each nucleus, where "SF" indicates emission lines from star formation and "NLSy1" a narrow-line Seyfert 1. BTA spectroscopic data for J2318+4314 (MCG +07-47-010) are new, described in Section 2.6; SDSS data were retrieved from the SkyServer; and all other spectra are described in the text. The position angle (PA) of the galaxy major axis is in degrees from north through east. Disk inclination is in degrees from edge-on, so 90° is face-on. "Type" is our estimate of each galaxy's Hubble morphological type.

photoionization of gas in the tails). Similarly, dust lanes acquired during mergers can impart disklike features (as in 3C 293 and 3C 305, shown by S. de Koff et al. 2000, where prominent dust lanes cross the central regions at steep angles to the major axis of the starlight distributions). For these reasons, we seek reasonably normal spiral patterns to ensure robust morphological classification. Two of the systems reported in the catalog-matching results of V. Singh et al. (2015) are normal spirals, while the other two show tidal tails and loops indicating recent major mergers (even if a spiral was involved); we therefore do not consider the latter galaxies as SDRAGNs here.

For comparison with the new RGZ sample, we compile data on the few previously identified SDRAGNs in Table 1. In this case, "previous" includes objects reported in the literature (that is, SDRAGNs found outside this RGZ+HST program, up to 2025 August 1), while our analysis was in progress. Along with names used in the literature, we include a short coordinate-based identifier of the same form (JHHMM+DDMM) as used for Zoo Gems objects. Where possible, we remeasure available data for consistency with the new sample. For 0313−192 (J0315−1906, cataloged after the initial detection with J2000 coordinates as 2MASX J03155208−1906442 and WISE J031552.09−190644.2, using catalogs from the 2 μm All-Sky Survey Extended Source listing described by M. F. Skrutskie et al. 2006 and Wide-field Infrared Survey Explorer as reported by E. L. Wright et al. 2010), we retrieved new versions of the HST images from W. C. Keel et al. (2006) to take advantage of improved astrometric accuracy (Section 3.1), and use the same Very Large Array (VLA) data reported by M. J. Ledlow et al. (2001). We also retrieved the archival HST images obtained by J. Bagchi et al. (2025) for J2345−0449 (2MASX J23453268−0449256) and by A. Capetti et al. (2000) for J0725+2957 (B2 0722+30). For the other objects, we use optical FITS images from the Legacy Surveys (A. Dey et al. 2019), using the g band for closest comparison with the HST F475W data, and radio data from the surveys listed in Section 2.3. We obtained new images for J2318+4314 (MCG +07-47-10) which is not covered by current deep optical surveys, as described in Section 2.7. For some of the previous SDRAGNs, the lobe structure is not well detected in the VLA Sky Survey (VLASS) data (M. Lacy et al. 2020), so we adopt radio properties from the discovery papers, some measured at lower frequencies than the VLA surveys. Implicitly, this suggests that the new sample from RGZ has lobe emission that is more prominent than the previous SDRAGNs as a group, at least as filtered through the VLASS surface-brightness and spatial-frequency limits. It also illustrates that increased surface-brightness sensitivity and longer-wavelength observations will show more of these objects, since the lobes typically have steep spectra and are more readily detected at frequencies below the 3 GHz VLA survey band. Notable examples are 2MASX J23453268−0449256, first identified as a giant radio galaxy with a spiral host by H. Andernach et al. (2012); the even larger source surrounding NGC 6185 (J1633+3520; M. S. S. L. Oei et al. 2023), for which the lobes are undetected in the VLASS data; and J0408-6247 (NGC 1534), where the lobes were first detected at 185 MHz (N. Hurley-Walker et al. 2015).

Optical spectra for the three galaxies with designations from the Sloan Digital Sky Survey (SDSS) were retrieved from the SDSS Data Release 15 SkyServer (D. S. Aguado et al. 2019), and for J0354–1340, J1350−1634, and J2345−0449 from the 6dFGS archive (D. H. Jones et al. 2004, 2009). We recovered the optical spectrum of J0315−1906 from Figure 7 of M. J. Ledlow et al. (1998) using the `automeris` web tool.[17] For J1633+3520 (NGC 6185), we obtained the summed spectra from R. A. Jansen et al. (2000). For J0725+2957 (B2 0722+30), we use the William Herschel Telescope long-slit data from B. H. C. Emonts et al. (2009). We obtained a new optical spectrum of J2318+4314 (MCG +07-47-10;

---

[17] https://automeris.io.

Section 2.6). We do not have an optical spectrum of J0408−6247 (NGC 1534).

Double radio sources are often characterized both by projected peak-to-peak lobe separations (Sep.) and largest (detected) angular size (LAS), or its equivalent in linear units, the largest linear size (LLS). The latter is more sensitive to very extended emission but often depends on observational sensitivity, particularly for lobes without distinct terminating hot spots, an issue that is especially important for type I Fanaroff–Riley (FR I; B. L. Fanaroff & J. M. Riley 1974) structures. Given the wide dynamic range in the radio data used here, we favor comparisons based primarily on lobe separation rather than LLS, while recognizing that some of our sources show significant emission beyond the lobe peaks. Both lobe separations and LAS are transformed into projected linear units, where redshifts are available, using a "consensus" cosmology with $H_0 = 70$ km s^{-1} Mpc^{-1}, $\Omega_M = 0.286$, and flat geometry; distances are computed using the JavaScript tool of E. L. Wright (2006). Instead of the angular LAS, we tabulate the LLS for the projected extent transformed to linear units (kiloparsec). For some of the previously identified objects where the discovery papers listed only LAS or LLS values, we estimate lobe separations from the published radio maps in the references listed.

Table 1 includes our derived viewing geometries—major-axis position angle and inclination from edge-on—for the previously reported SDRAGNs. Throughout this paper, we adopt this convention for disk inclination measuring from edge-on, as the error behavior is more intuitive (smaller uncertainties near zero) and the analysis for disk–jet angles likewise is simplified. When dust is present within the disk, we use two complementary approaches: (1) treating the outer edge of the dust lane as outlining a circular feature in the disk plane, and (2) measuring the offset between the centerline of the dust lane and the center of the bulge isophotes. Otherwise, we use isophotes of the disk and outer regions, correcting for finite disk thickness as in, for example, R. B. Tully et al. (1998). The listed uncertainties include a range of values for the ratio r_0 of disk thickness to radius, from 0.1 to 0.2. Three systems are so nearly face-on that we cannot rely on the outer isophotes or resonance rings to be circular at the requisite level; the listed values reflect these additional uncertainties. In J1649+2635 and J1633+3520 (NGC 6185), the derived inclination ranges incorporate the requirement that spiral arms be monotonic in radius as a function of angle, without assuming that they be logarithmic. We also list Hubble types derived by inspection of the HST or Legacy Survey images, to maintain consistency with the new sample. J0725+2957 has FR I morphology (so the lobe separation is poorly defined), and has a substantially smaller LLS than the other systems. However, its radio structure appears better collimated than that of starburst-wind sources, so we include it among the SDRAGNs considered here.

We attempt to distinguish genuine spirals from galaxies that possess prominent stellar disks but lack spiral structure (S0 or lenticular systems). Some hosts of large-scale double sources are known to be S0s, such as NGC 612 (M. P. Véron-Cetty & P. Véron 2001), PKS 1814−627 (R. Morganti et al. 2011), and ESO 514-G03 (Gopal-Krishna et al. 2012), but given their markedly different ISM content compared to spirals, they are outside the scope of this project. Based on the results of A. Vietri et al. (2022), it is likely that additional NLSy1 galaxies will be found to host SDRAGNs. These objects are now routinely cataloged at redshifts $z > 0.4$, where typical ground-based imaging is insufficient to reveal spiral structure; and a significant fraction of them have radio jets, some of which are aligned with large-scale double sources (S. Rakshit et al. 2018).

Some of the radio lobes in these previously identified SDRAGNs are not detected in VLASS data, especially those discovered at lower frequencies, such as with the Giant Metrewave Radio Telescope (GMRT). This suggests that lower-frequency data will be particularly effective in finding additional systems (as is true for traditional DRAGN sources as well). For example, Speca shows potential "relic lobes" spanning nearly 1 Mpc in projection when observed at 325 MHz (A. Hota et al. 2011), while J1350−1634 extends beyond 2 Mpc (S. Sethi et al. 2025).

2.2. Radio Galaxy Zoo Selection of Potential Spiral Host Galaxies

The original RGZ (J. K. Banfield et al. 2015; O. I. Wong et al. 2025) selection of host galaxies used the Faint Images of the Radio Sky at Twenty-cm (FIRST; R. H. Becker et al. 1995) survey along with Australia Telescope Large Area Survey (or ATLAS; R. P. Norris et al. 2006; E. Middelberg et al. 2008) data, with host-galaxy identifications initially based on WISE or Spitzer data, complemented by SDSS imaging. In detail, the web interface presented volunteers with a $3' \times 3'$ field combining data from 3.4 μm WISE, FIRST images, and radio contours. A slider allowed each field to be viewed as a combined WISE/radio image, from radio only (FIRST image plus contours) to WISE only. Once a volunteer finished the classification task, an option allowed discussion of the field in a discussion forum.[18] Each RadioTalk page for a field includes links to larger ($9' \times 9'$) FIRST and WISE images, images from the NRAO VLA Sky Survey (NVSS; J. J. Condon et al. 1998), and optical observations from SDSS Data Releases 10 (C. P. Ahn et al. 2014), 12 (S. Alam et al. 2015), and 13 (F. D. Albareti et al. 2017). A 140-character comment box is supplied, in addition to the aforementioned discussion boards, where more extended commentary on individual sources and classes of sources took place. Selection of SDRAGN candidates was restricted to sky regions covered by FIRST.

A group of RGZ volunteers specifically identified potentially spiral hosts and flagged them for discussion on the project forum. Over time, experience showed that the SDSS *fracdev* parameter, the fraction of galaxy light attributed to a de Vaucouleurs profile bulge, provided a useful quantitative metric for evaluating candidates as well. At the project's end, 215 SDRAGN candidates had been identified, initially divided into three broad likelihood categories, along with a few additional objects drawn from literature sources. These are all listed in Table 12 in Appendix D, to document the starting sample, preserve the initial priority categories, and tabulate quantities important in understanding the selection of both the entire RGZ SDRAGN candidate set and the subset targeted for HST imaging.

---

[18] https://radiotalk.galaxyzoo.org; content frozen as of 2019 May.

2.3. Radio Data

Our analysis in this work uses radio data from the Karl G. Jansky VLA, specifically the FIRST survey and ongoing VLASS (M. Lacy et al. 2020); the Low-Frequency Array (LOFAR; M. P. van Haarlem et al. 2013), via the LOFAR Two-meter Sky Survey (LoTSS; T. W. Shimwell et al. 2017, 2019, 2022); and the Australian Square-Kilometre Array Precursor (ASKAP), using the Rapid ASKAP Continuum Survey (RACS; D. McConnell et al. 2020) near 900 MHz. These are complementary in angular resolution, sensitivity, frequency, and spatial-frequency coverage. For VLASS, where observations continue, we used the "Quick-Look" median of observations in epochs 1–3,[19] which mitigates some artifacts compared to single-epoch products.

2.4. Zoo Gems Target Selection and Observations

As described in W. C. Keel et al. (2022), the list of SDRAGN candidates from RGZ (Appendix B) was winnowed for inclusion in the Zoo Gems program of short-exposure HST images, by having members of the public vote on which objects from a list (already screened for scientific suitability) should be carried forward into a limited target list for HST observations. At this stage, participants had the option of blinking between the optical SDSS image of a field and a version with radio contours overlaid. All potential SDRAGNs had been examined by the first author, to confirm evidence of disk structure in SDSS images before inclusion in the RGZ sample.

Table 12 in Appendix D lists the whole sample of SDRAGN candidates from RGZ, which ones were selected for the HST target list or actually observed, and the magnitude and axial-ratio quantities we considered for observational selection. The HST observations themselves formed part of a pool to be scheduled as fillers chosen for sky location between higher-priority observations, so they were taken from the overall Zoo Gems list essentially at random. As fillers, these observations were short: pairs of 337 s exposures with a small dither offset in between. Among the 299 Zoo Gems input targets, 66 were SDRAGN candidates, of which 36 were observed and 30 were not.

As required for the gap-filler programs, these HST images used the Advanced Camera for Surveys (ACS; H. C. Ford et al. 1998; J. E. Ryon & D. V. Stark 2023). To minimize effects of deteriorating charge transfer efficiency in the ACS images, the target galaxies were located near one corner of the instrument field (29″–40″ from the nearer edge of the two dithered exposures, and 46″ for the nearby system UGC 1797). As a result, one radio lobe often falls outside the HST field of view, as reflected in some of our image overlays. For the image versions we show here, the numerous cosmic-ray residuals remaining after pipeline combination of the two offset images for each object were patched interactively in regions around the target galaxy, by interpolation from surrounding pixel values using the IRAF IMEDIT task.

We chose the F475W filter, similar to the SDSS g passband, to maximize the contrast of any (usually blue) spiral arms in the galaxies. For larger redshifts, F555W might have given similar contrast and better detector efficiency, but fewer than half the sample had known redshifts at the outset.

Table 2 lists the 36 candidate SDRAGN galaxies observed by HST,[20] now that the Zoo Gems program has completed, along with spectroscopic redshifts where they are available. Optical coordinates listed are from the HST images, for the nuclei of possible SDRAGN hosts (Section 3.1). The precision of these coordinates is 0.02″ for bright symmetric bulges; for obscured nuclei, where positions are inferred from the symmetry of surrounding dust-free isophotes, the precision may be as poor as 0.″2. Table 11 lists alternate identifications, including the RGZ internal designations used in online discussions and the short names we use for convenience. Among these galaxies, four (J0016+0226, J1516+0517, J1457+2832, and J613+3018) were observed recently and were not included by Z. Wu et al. (2022). Our morphological classification of J0958+5619 differs from that by Z. Wu et al. (2022), who assign it as a spiral. Based on the dust lane cutting across the galaxy core nearly perpendicular to the possible disk, we consider it more likely that this is the late aftermath of a merger with clumpy debris in the outer regions, some of which appears to be highly ionized and affects the structure in the HST image through the inclusion of [O II] emission in the passband (Appendix C).

2.5. Geometric Selection Effects

Selection effects may influence the input sample of candidate SDRAGNs through both optical and radio properties. In optical imaging, spiral arms are more easily recognized when a galaxy is seen nearly face-on, whereas exponential-disk fitting in SDSS becomes more effective when the disk is nearly edge-on, helping to separate it from a rounder bulge component. The radio structure may not be recognized as a double if the two lobes are projected so close together that they blend in available data; similarly, if the system is viewed too close to the radio axis, a large-scale double source may not be recognized as extending beyond the host galaxy.

The combined set of observed and targeted Zoo Gems SDRAGN candidates therefore implicitly reflects the geometric and magnitude-dependent selection factors operating both in the RGZ candidate selection process and in the construction of the HST target list. We examine the optical selection using the set of all galaxies considered for inclusion in the Zoo Gems SDRAGN category (213 in the SDSS sky coverage), as well as the subset ultimately voted for the target list (66 candidates, of which 64 are within the SDSS). We extract SDSS "model magnitudes" in the r band, along with the axial ratio b/a (SDSS PhotObj parameter *expAB_r*) from an exponential-disk fit and the nominal bulge fraction (*fracdev_r*), using the measured axial ratio rather than the more physical inclination angle, since the axial ratio is available for all candidates. We collect similar data for the heterogeneously selected group of previous SDRAGNs, as well, using SDSS or Legacy Survey r-band magnitudes where available and measuring new axial ratios when necessary. The SDSS axial ratios generally provide good representations of the structures seen in HST images, with the exception of J1721+2624, where the SDSS fit fails to capture outer spiral structure that traces an ellipse with an axial ratio of 0.51.

For comparison, we take the empirical distribution of axial ratios for spiral galaxies in the SDSS presented by

---

[19] http://archive-new.nrao.edu/vlass/HiPS/MedianStack/Quicklook

[20] Available at doi:10.17909/rvae-bn13.

Table 2
HST Observations

Dataset	HST Object Name	α_{2000}	δ_{2000}	Date Observed	z
JDS45K010	SDSS J001627.47+022602.1	00 16 27.476	+02 26 02.25	2022-09-23	0.0583
JDS44T010	SDSS J020904.75+075004.5	02 09 04.755	+07 50 04.53	2021-10-22	0.2552
JDS43Y010	UGC 1797	02 19 58.732	+01 55 49.16	2018-07-03	0.0410
JDS44I010	SDSS J080259.73+115709.7	08 02 59.738	+11 57 09.70	2021-01-10	⋯
JDS44J010	SDSS J080658.46+062453.4	08 06 58.476	+06 24 53.15	2020-05-28	0.0834
JDS45G010	SDSS J081303.10+552050.7	08 13 03.125	+55 20 50.66	2019-12-25	0.2645
JDS44G010	SDSS J082312.91+033301.3	08 23 12.915	+03 33 01.39	2021-03-15	0.0897
JDS44K010	SDSS J083224.82+184855.4	08 32 24.828	+18 48 55.45	2021-09-28	0.1138
JDS45B010	SDSS J083351.28+045745.4	08 33 51.292	+04 57 45.35	2021-03-18	⋯
JDS45I010	SDSS J084759.90+124159.3	08 47 59.901	+12 41 58.96	2021-10-02	0.1745
JDS41L010	B3 0852+422	08 55 49.153	+42 04 20.10	2021-03-14	0.1804
JDS45W010	SDSS J090147.17+164851.3	09 01 47.173	+16 48 51.32	2021-11-13	⋯
JDS45L010	SDSS J090305.84+432820.4	09 03 05.861	+43 28 20.41	2021-03-15	0.3736
JDS43Z010	B3 0911+418	09 14 45.557	+41 37 14.04	2021-12-29	0.1404
JDS45H010	SDSS J091949.07+135910.7	09 19 49.085	+13 59 10.78	2018-05-15	⋯
JDS47L010	SDSS J092605.17+465233.9	09 26 05.183	+46 52 33.68	2021-12-29	0.2181
JDS44R010	B2 0938+31A	09 41 03.617	+31 26 18.56	2020-02-13	0.3940
JDS47H010	SDSS J095605.87+162829.9	09 56 05.861	+16 28 30.13	2020-02-14	0.2745
JDS44P010	SDSS J095833.44+561937.8	09 58 33.433	+56 19 37.80	2020-10-17	0.2422
JDS45T010	SDSS J112811.63+241746.9	11 28 11.617	+24 17 46.82	2019-02-23	0.1153
JDS47K010	SDSS J113648.57+125239.7	11 36 48.578	+12 52 39.48	2021-03-14	0.0345
JDS45E010	SDSS J130300.80+511954.7	13 03 00.803	+51 19 54.70	2021-10-01	0.1164
JDS45A010	IC 4234	13 22 59.871	+27 06 59.00	2020-04-09	0.0344
JDS44X010	SDSS J132809.31+571023.3	13 28 09.247	+57 10 23.97	2019-05-14	0.0211
JDS47J010	SDSS J134900.13+454256.5	13 49 00.137	+45 42 56.41	2019-11-13	⋯
JDS45Z010	B3 1352+471	13 54 36.019	+46 57 01.26	2019-04-28	⋯
JDS44A010	4C +28.38	14 57 53.810	+28 32 18.77	2023-08-25	0.1440
JDS44D010	SDSS J150903.21+515247.9	15 09 03.224	+51 52 47.94	2020-01-14	0.5789
JDS43X010	SDSS 151659.24+051751.5	15 16 59.245	+05 17 51.58	2023-08-25	0.0512
JDS44H010	B2 1611+30	16 13 58.621	+30 18 09.51	2023-09-25	0.1522
JDS45J010	SDSS J163300.85+084736.4	16 33 00.862	+08 47 36.62	2019-07-11	0.2247
JDS45F010	SDSS J163624.97+243230.8	16 36 24.984	+24 32 30.78	2021-06-05	0.1016
JDS44Z010	B2 1644+38	16 46 28.433	+38 31 15.73	2019-07-19	0.1075
JDS44C010	SDSS J16562058+6407529	16 56 20.685	+64 07 52.90	2018-08-24	0.2121
JDS43V010	SDSS J172107.89+262432.1	17 21 07.917	+26 24 31.93	2019-08-22	0.1696
JDS45V010	SDSS J214110.61+082132.6	21 41 10.612	+08 21 32.54	2019-12-11	0.3946

N. D. Padilla & M. A. Strauss (2008). For this entire set of 213 candidates, the axial-ratio distribution is consistent with that from N. D. Padilla & M. A. Strauss (2008), although significant differences with galaxy magnitude are evident (Figure 1). Galaxies brighter than $r = 16$ have a mean $b/a = 0.69$, while for $r > 20$ the mean decreases to 0.41 with a monotonic trend across 2 mag bins. In particular, there is a relative deficit of bright, edge-on candidate galaxies (or an excess of bright, face-on objects). The nine previously identified SDRAGNs are all brighter than $r = 16.1$, with a mean $b/a = 0.57$ and a median of 0.45.

One might see these statistics, and the lack of highly inclined bright and nearby galaxies in Figure 1, as evidence that each of the obvious selection effects above is operating for galaxies at opposite ends of the magnitude range we sample. It therefore makes sense to examine the relation between the orientations of radio sources and galactic disks, taking account of this external selection. Bright objects are preferentially selected in disk orientations that provide limited information on the disk–jet angle, whereas the faintest galaxies provide the most information by reducing the range of one angular variable. We incorporate these factors in our analysis of radio-source axes with respect to galactic disks in Section 6.

2.6. *Optical Spectroscopy*

The most promising SDRAGN candidates without previously published redshifts, including one from the previous list in Table 1, were observed spectroscopically using the SCORPIO-1 (V. L. Afanasiev & A. V. Moiseev 2005, used for J0855+4204) or SCORPIO-2 (V. L. Afanasiev & A. V. Moiseev 2011) systems in long-slit mode at the prime focus of the 6 m telescope (Bol'shoi Teleskop Azimutalnyi, Large Altazimuth Telescope or BTA) of the Special Astrophysical Observatory, Russian Academy of Sciences. These observations were primarily part of a backup program for poor weather conditions, allowing measurements of redshifts and emission-line equivalent widths (EWs) and ratios, though absolute flux values were not always measurable. The resulting redshifts are included in Table 2. These new spectroscopic observations are listed in Table 3, including the position angle of the slit (PA, north through east) and emission-line classification of the nucleus, as in Section 4.3 (where we use "SF" for emission lines indicating star formation, "composite" to denote objects near the boundary between star-forming and AGN spectra, and "Sy 1.9" to indicate a Seyfert narrow-line spectrum with a broad-line component detected at Hα). Among these galaxies, J0958+5619, while not a spiral as shown by the HST image, shows extended emission-line regions (EELRs), including He II off the nucleus, spanning $22''$ (85 kpc) end-to-end. We

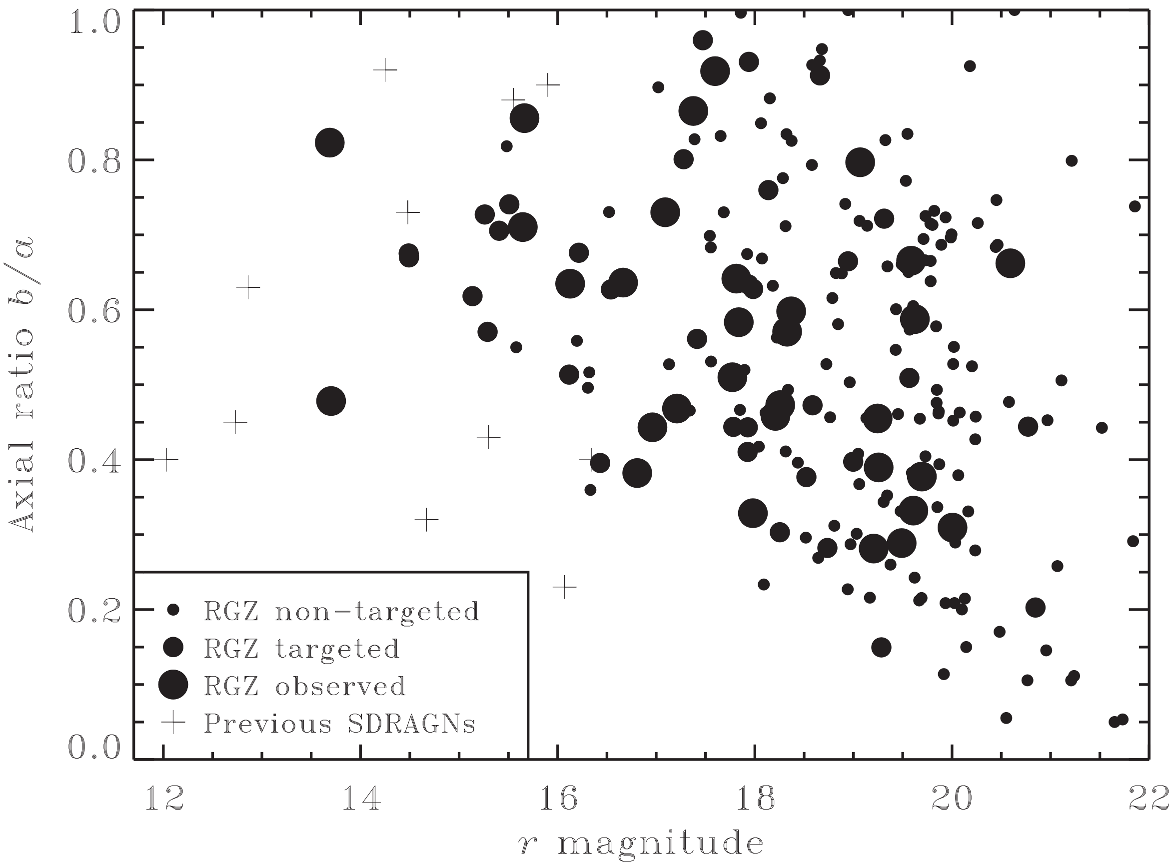

Figure 1. Magnitude in the r band vs. SDSS axial ratio b/a for subgroups of the SDRAGN sample, illustrating selection effects as a function of apparent magnitude. Small filled circles denote galaxies in the sample from which the observing list was drawn but not selected for the HST target list; intermediate filled circles indicate galaxies included in the HST target list but not observed; and large filled circles represent the objects observed and analyzed here. The 11 previously identified SDRAGN systems are represented by plus signs. The brightest RGZ galaxies (12/14 of which are in the HST target sample) are seen systematically more face-on than a random set of SDSS disk systems, whereas the faintest systems are systematically more edge-on.

Table 3
BTA Spectroscopy of Nuclei

Object	Date	Exposure (s)	Nucleus	z	PA (deg)
J0209+0750	2022-09-19	2400	Sy 2	0.2552	122
J0219+0155	2023-07-19	1200	LINER	0.0410	0
J0806+0624	2023-03-14	1800	SF	0.0834	145
J0813+5520	2022-12-30	3600	SF	0.2645	97
J0855+4204	2024-08-11	3600	Quiescent	0.1804	177
J0926+4652	2022-06-03	3000	Sy 2	0.2181	161
J0941+3126	2022-02-07	1800	Sy 2?	0.3940	44
J0956+1628	2022-02-07	1800	Sy 2	0.2745	121
J0958+5619	2016-02-15	1800	Sy 2	0.2422	90
J1128+2417	2023-01-18	2400	H II	0.1153	139
J1303+5119	2023-01-16	3600	H II?	0.1164	60
J1328+5710	2023-01-20	1800	H II	0.0211	114
J1613+3018	2023-09-18	1200	H II	0.1522	60
J1633+0847	2022-03-09	1800	Sy 1.9	0.2247	134
J1636+2432	2023-07-18	4500	SF	0.1016	40
J1656+6407	2023-03-27	3600	SF	0.2121	60
J2141+0821	2022-11-30	1200	Sy 2?	0.3946	110
J2318+4314	2022-10-22	1500	SF	0.0169	139

Note. Nucleus indicates the emission-line classification of the galaxy nucleus, as in Section 4.3. PA gives the position angle of the spectrograph slit, north through east, in degrees.

document these features and their kinematics in Appendix C. With these observations, we now have spectra and redshift values for all new SDRAGNs identified in Sections 3.1.1 and 3.1.2.

2.7. Ground-based Imaging

Among the previously reported SDRAGNs in Table 1, J2318+4314 (MCG +07-47-010) lies outside the imaging coverage of both the SDSS and Legacy Surveys. For a more detailed view of the host-galaxy structure, we obtained new B and R images using the 1 m Jacobus Kapteyn Telescope on the island of La Palma, remotely operated as part of the SARA Observatories (W. C. Keel et al. 2017). From observations on 2022 June 4, we stacked 6×300 s exposures in B and 12×180 s exposures in R. The image quality in the stacked sums was FWHM = $1\farcs2$ (R) and $1\farcs3$ (B). These images are shown in Figure 2, illustrating the prominent grand-design spiral pattern, asymmetric outer structure of the system, and an inner bar extending to a radius of $1\farcs6$ (0.5 kpc).

3. Results

3.1. Host Identifications: Astrometry

3.1.1. Sources with Radio Cores

Where radio cores are detected, we use astrometric matching to assess the likelihood that each observed spiral

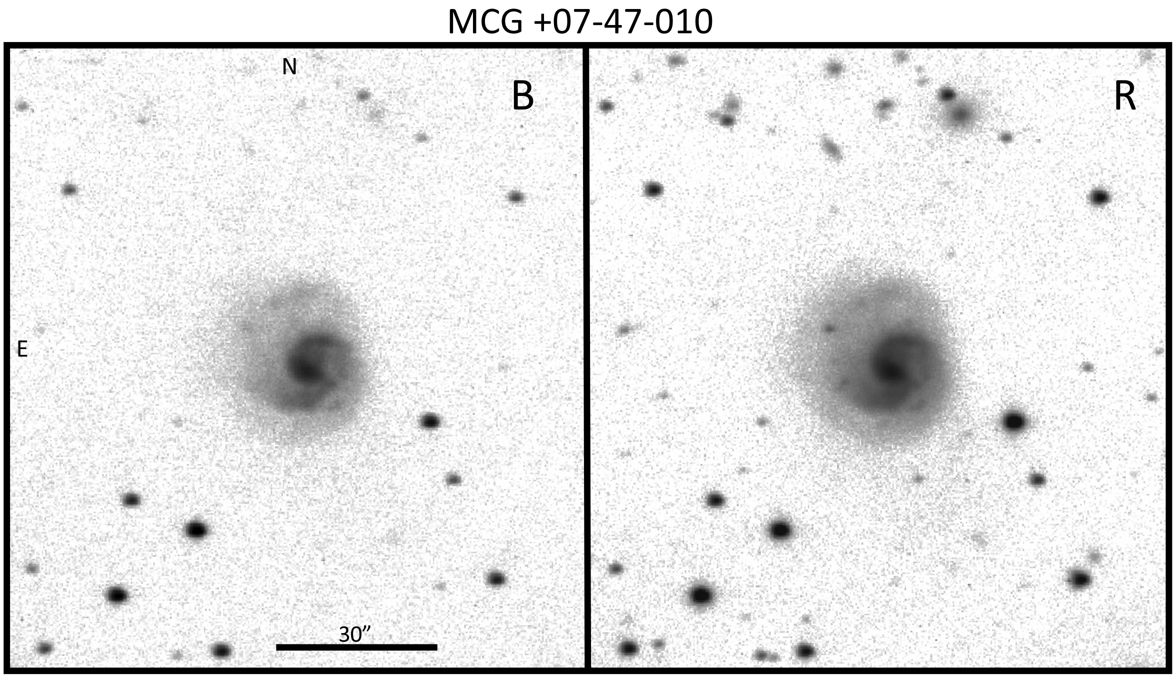

Figure 2. Previously identified SDRAGN J2318+4314 (MCG +07-47-010), shown in *B* and *R* images from the Jacobus Kapteyn Telescope. Each panel is displayed with a logarithmic intensity mapping. North is at the top and east is to the left; the field shown spans 160″ E–W by 172″ N–S.

Table 4
Optical and Radio Core Positions

Object	HST: α_{2000}	δ_{2000}	VLASS α	δ	Offset (arcsec)	FIRST α	δ	Offset (arcsec)
J0209+0750	02 09 04.755	+07 50 04.53	04.739	04.23	0.38	⋯	⋯	⋯
J0219+0155 (UGC 1797)	02 19 58.732	+01 55 49.16	58.756	49.08	0.38	⋯	⋯	⋯
J0847+1241	08 47 59.901	+12 41 58.96	59.89	59.4	0.47	59.889	59.45	0.52
J0855+4204	08 55 49.153	+42 04 20.10	49.085	20.67	0.94	⋯	⋯	⋯
J0926+4652	09 26 05.183	+46 52 33.68	5.186	33.66	0.04	⋯	⋯	⋯
J0941+3126	09 41 03.617	+31 26 18.56	03.620	18.22	0.34	⋯	⋯	⋯
J0956+1628	09 56 05.861	+16 28 30.13	5.855	30.27	0.15	⋯	⋯	⋯
J1322+2706 (IC 4234)	13 22 59.871	+27 06 59.00	59.828	59.06	0.57	59.882	59.08	0.17
J1516+0517	15 16 59.245	+05 17 51.58	59.254	51.77	0.23	⋯	⋯	⋯
J1633+0847	16 33 00.857	+08 47 36.56	⋯	⋯	⋯	00.832	36.60	0.37
J1646+3831	16 46 28.433	+38 31 15.73	28.373	16.43	1.00	⋯	⋯	⋯
J1656+6407	16 56 20.685	+64 07 52.90	20.641	52.89	0.29	⋯	⋯	⋯
J1721+2624	17 21 07.917	+26 24 31.93	07.931	32.24	0.36	07.914	32.10	0.17

galaxy is the true AGN host. The absolute coordinate accuracy of HST image products retrieved from MAST has been considerably improved through the incorporation of Gaia data, both in the coordinates of guide stars and directly in the images when Gaia objects are included, as set out by B. McLean et al. (2020) and by J. Mack.[21] Where dust lanes affect the peak position of a nucleus in the HST images, we use the center of the surrounding isophotes to obtain a better estimate of the nucleus location.

In Table 4, we compare the positions of the optical nuclei of candidate SDRAGNs with both radio cores and spiral morphologies, as derived from HST images, with available radio data of sufficient sensitivity and resolution to distinguish core sources from surrounding structure. This comparison omits galaxies that are either not spirals or are so far from the radio positions ($>1''$) as to be ruled out as the true AGN hosts. The astrometry is based on VLASS products combining first- and second-epoch observations, which correct astrometric biases present in the first-epoch QuickLook reductions. For cores detected in VLASS but not listed in the VLASS source catalog, we derive positions from their peaks in the FITS cutout images. We compare the positions of the four core sources also included in the FIRST source catalog. We compare the optical and radio positions in Table 4, listing only the seconds and arcseconds components of the radio coordinates for brevity. As a heuristic guide to the expected astrometric precision of the radio surveys, we follow J. J. Condon (1997) in using the estimated FWHM/(2 × SNR), except for values from the FIRST source catalog,[22] which recommends positional uncertainties given by (observed source size) × 1/(SNR + 0.05). The largest position offsets seen here for isolated core sources, $0\farcs5$, occur for systems with

---

[21] https://outerspace.stsci.edu/display/HAdP/Improvements+in+HST+Astrometry.

[22] See https://sundog.stsci.edu/first/catalogs/version 14, December 17).

obscured nuclei whose locations are inferred from unobscured isophotes; these offsets are less than 1.7 times the combined HST and radio uncertainties. We use values from the VLASS source catalog via CIRADA[23] when the source is included; otherwise, for lower-signal-to-noise-ratio (S/N) sources, we measure positions from the VLASS image cutouts. In almost all cases, the error contribution from the S/N in the VLA surveys is larger than the expected contribution from HST data, even in those cases where the position of the obscured nucleus must be estimated from surrounding isophotes. In B3 0852+422, we see an inner $7\farcs9$ double source with excess emission between the lobes, which we identify with the radio core, whose position is uncertain at the $1\farcs0$ level due to confusion with the small-scale lobes. The VLASS data for B2 1644+38 are affected by side-lobe artifacts, giving a similar uncertainty. Globally, the mean position offset between optical nuclei and radio cores for all VLASS sources in Table 4 is $0\farcs42$, and $0\farcs31$ for sources in the FIRST catalog. Additional physical contributions to these offsets may arise if, for example, unresolved small-scale jets occur in the radio surveys, so the apparent radio core location will be a centroid of this more complex structure, offset from the true core location. The 13 galaxies in Table 4 form our highest-probability sample of new SDRAGNs, for which confusion with distant background systems is least likely.

3.1.2. Sources without Detected Radio Cores

Secure identification of a host galaxy is inevitably more uncertain when no radio core is detected, since double sources may be asymmetric in intensity, distance from the core, and direction from the core. A useful (if difficult to quantify) heuristic using radio contour maps is to accept an identification if the optical nucleus lies between the lowest contours of the radio lobes at their closest approach to one another; that is, near the minimum-intensity location along the ridgeline of radio emission between the lobes. This is less useful when the two lobes are separated by distances much larger than their individual sizes. An independent estimate of the plausible degree of source bending can sometimes be inferred from the host's location with respect to galaxy environment; for example, wide-angle tail sources are most common in dense regions rather than in cluster outskirts or lower-density regions (A. F. Garon et al. 2019).

Among the Zoo Gems SDRAGN candidates, we identify five likely genuine SDRAGNs for which no radio core is detected in VLASS data: J0016+0226, J0806+0624, J1128+2417, J1613+3018 (B2 1611+38), and J1636+2432. As detailed in the notes on individual sources, two of these have more compelling faint, red host candidates located closer to the axis between the lobes than the candidate SDRAGNs; two spirals remain the best-detected host candidates (J0806+0624 and J1636+2432); and one system, J0016+0226, remains ambiguous on both grounds. None of these objects shows significant AGN components in their optical spectra, which is to be expected given the lack of detected radio cores, though this deprives us of a possible additional clue as to the host identifications. In the analysis that follows, we include J0806+0624 and J1636+2432 among the SDRAGNs; together with the objects with detected radio cores from the previous section (Table 4), they make up our sample of 15 RGZ SDRAGNs.

4. Galaxy Identification and Properties

Figure 3 shows the 15 spiral galaxies identified in Sections 3.1.1 and 3.1.2 as the RGZ SDRAGN sample. Contours from the VLASS and LoTSS data are overlaid on SDSS color images to show the location, extent, and structure of the radio emission. Due to the widely differing sizes of the radio sources, the angular scale varies between objects, as indicated. In the case of J1322+2706 (IC 4234), structure within the source makes contour representations difficult to interpret; therefore, we show its low-resolution LoTSS data in grayscale in Figure 4, along with a schematic depiction of two partially overlapping elliptical and filamentary lobes along our line of sight.

4.1. Optical Morphologies

The optical structures are better seen in Figure 5, where the radio contours are omitted and the intensity scales are tailored for each galaxy's size and surface brightness. We present morphological classifications for the SDRAGN candidates in Table 5, using the extended Hubble system, along with disk orientations and inclination angles derived from the HST images and the morphological features underlying these classifications. The derived inclinations are with respect to edge-on, such that 90° indicates a face-on disk. As in the case of J0315–1906 (W. C. Keel et al. 2006), our classifications incorporate the classic observation (from continuity across galaxy samples with different inclination angles) that edge-on spirals have dust lanes coextensive with the observed stellar disk, while dust lanes in S0 systems are more restricted in radial extent, often forming an annulus (A. Sandage & G. A. Tammann 1987; A. Sandage & J. Bedke 1994; R. J. Buta et al. 2007). All the hosts we identify as edge-on spirals satisfy this criterion. Spiral features identified mainly via attenuation of background starlight are noted as "dust arms."

Bars are common among spiral galaxies, with roughly one-third showing large-scale bars, one-third having weak or small bars, and one-third lacking detectable bars altogether. Bars are clearly not overrepresented among SDRAGN hosts. Only two of these SDRAGNs, both among the previously known subset, host bars large enough to appear in standard Hubble classifications: J0354–1340, classified as type (R)SBa, and J2318+4314 (MCG +07-47-10), classified as type SBc. Among the previous SDRAGNs, J1633+3520 (NGC 6185) shows a small nuclear bar as well as a faint, possibly tidal external arm, while the boxy isophotes in J0315–1906 may indicate a central bar viewed not only edge-on but end-on. Among the RGZ SDRAGNs, the number of hosts seen close to edge-on or at high redshifts limits the detectability of potential bar signatures. We therefore attempt to classify the presence or absence of bars for only the eight objects viewed more than 12° from edge-on. Only one of the RGZ SDRAGNs shows a small-scale bar, J0806+0624.

4.2. Galaxy Orientations

The disk inclinations in Table 5 indicate a sample rich in systems seen almost edge-on, in contrast to what is found in, for example, optically selected Seyfert galaxies (W. C. Keel 1980; C. D. P. Lagos et al. 2011; H. M. Tovmassian & O. Yam 2011). Several selection biases may contribute to this trend. To the extent that the radio-source axes are perpendicular to the disks, projection effects would reduce their

---

[23] https://cirada.ca/vlasscataloguequl0

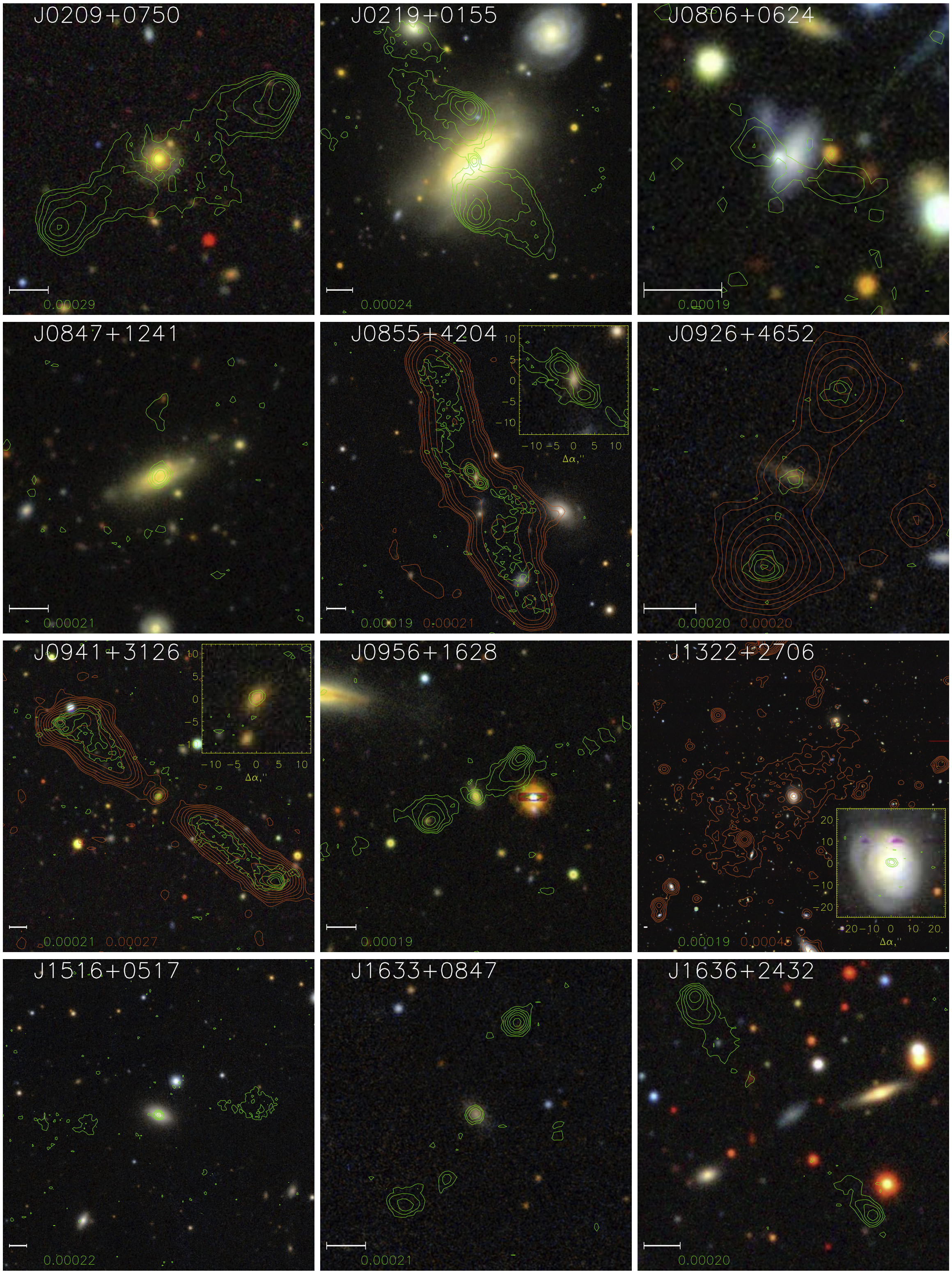

Figure 3. Montage of radio survey contours overlaid on SDSS *gri* images for the 15 probable SDRAGN candidates (with and without radio cores) from the RGZ +Zoo Gems sample. North is at the top and east is to the left; horizontal scale bars indicate 5″. Some double sources are so large that the galaxy cannot be well shown (and core contours are affected by smoothing at this scale); for these, we include an enlarged "core" region as well. Radio data are from the VLASS median of epochs 1–3 (green contours) and LoTSS (orange contours). Radio contours are spaced by factors of 2 in brightness, starting with the values in jansky per beam shown in the numbers in matching colors at the bottom of each panel. These represent values 1.8–2.5 times the rms noise level, set to minimize the appearance of interferometric artifacts, over ranges appropriate for showing important radio structures while reducing clutter. The SDSS images are shown in the R. Lupton et al. (2004) "sinh" mapping to display detail over a wide dynamic range. Coordinate-based designations are as in Table 11 in Appendix B.

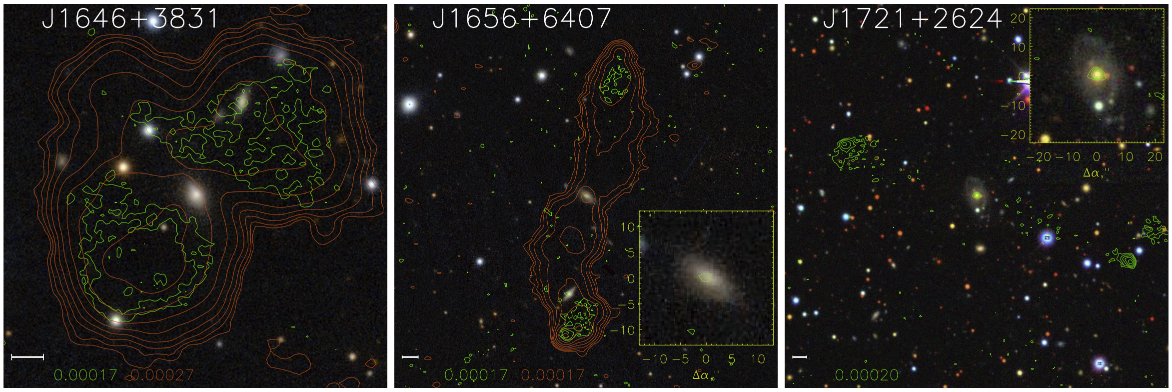

Figure 3. (Continued.)

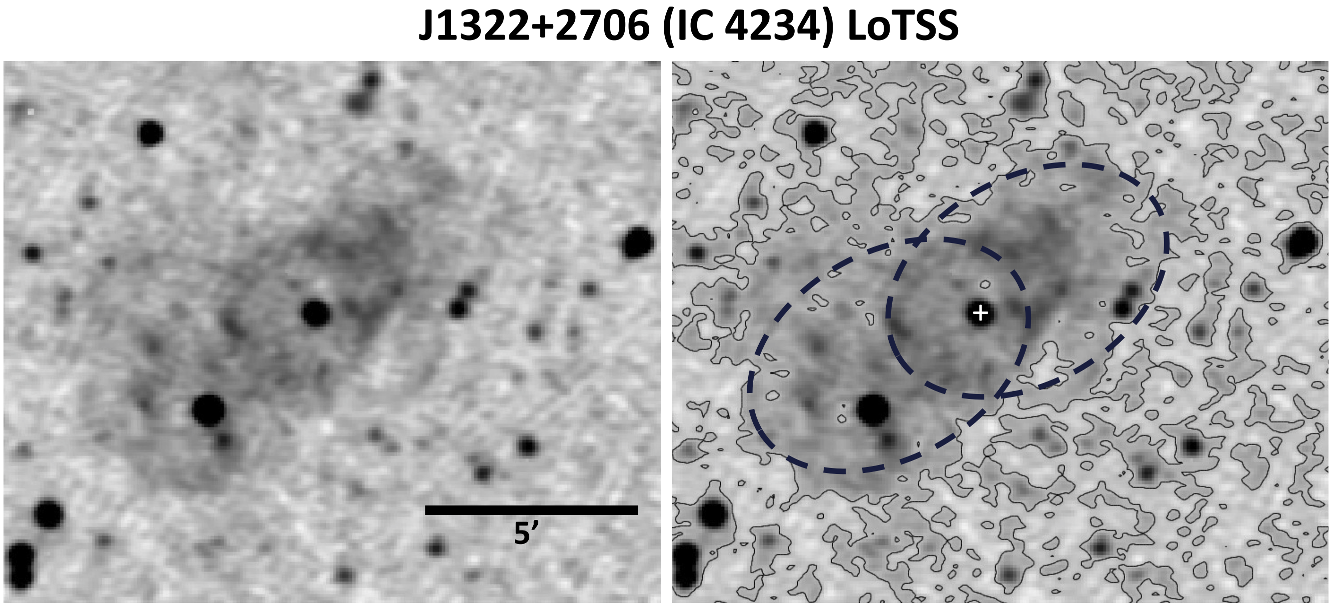

Figure 4. Low-resolution LoTSS image of J1322+2706, shown in grayscale to illustrate the radio structure. The left panel shows a negative linear intensity mapping, with 5′ scale bar. The right panel shows the same mapping with a contour at the local $1-\sigma$ level of 0.125 mJy per beam, and a schematic interpretation of two elliptical, filamentary lobes seen in projection. The white cross shows the optical and radio nucleus; the size of the optical galaxy detected with HST (see Figure 5) falls within the point-spread function of the radio nucleus here.

angular extent and possibly blend them into single sources at moderate resolution, so they would no longer be selected as double sources. For the optical images, selection based on SDSS image parameters for the largest exponential-disk fractions becomes more accurate for faint galaxies which are seen closer to edge-on (K. L. Masters et al. 2010). This effect is further enhanced by attenuation from centrally concentrated dust within the disk and resolution limitations for distant galaxies, both of which tend to make the disk appear more prominent in the outer isophotes (increasing the apparent scale length while contributing less to the central surface brightness). This effect acts in the opposite sense to the more commonly encountered dust effect, in which inclined spirals are excluded from nominally flux-limited samples due to extinction within the disk. As noted in Section 2.5, the distribution of projected axial ratios in this sample suggests that this effect dominates the selection for fainter galaxies.

4.3. Optical Spectra and AGN Signatures

The collected optical spectra of the nuclei of previously identified SDRAGNs are shown in Figure 6, while those of the newly identified systems are shown in Figures 7 and 8. In some cases, these spectra represent substantial parts of the host galaxies; projected effective aperture diameters (for noncircular extraction regions, the diameter of a circle with the same area) range from 3 to 13 kpc for the Zoo Gems SDRAGNs and from 0.5 to 11 kpc for the previously identified objects. This introduces significant dilution of nuclear emission-line signatures, both through the inclusion of surrounding starlight, which reduces the EWs, and through mixing with emission from star-forming regions common in spiral galaxies and gas ionized by hot, evolved stars (low-ionization emission regions, or LIERs, as defined by F. Belfiore et al. 2016, sometimes known as “retired galaxies,” and distinguished from low-ionization nuclear emission regions, or LINERs, which include weak AGNs). AGN classifications based on these optical spectra are therefore robust, as they persist despite these diluting effects, although more modest optical AGNs may exist in objects with other spectroscopic classifications. Since LIER emission powered by hot, evolved stars (F. Belfiore et al. 2016) scales with the included starlight for old populations, we follow R. Cid Fernandes et al. (2011) in

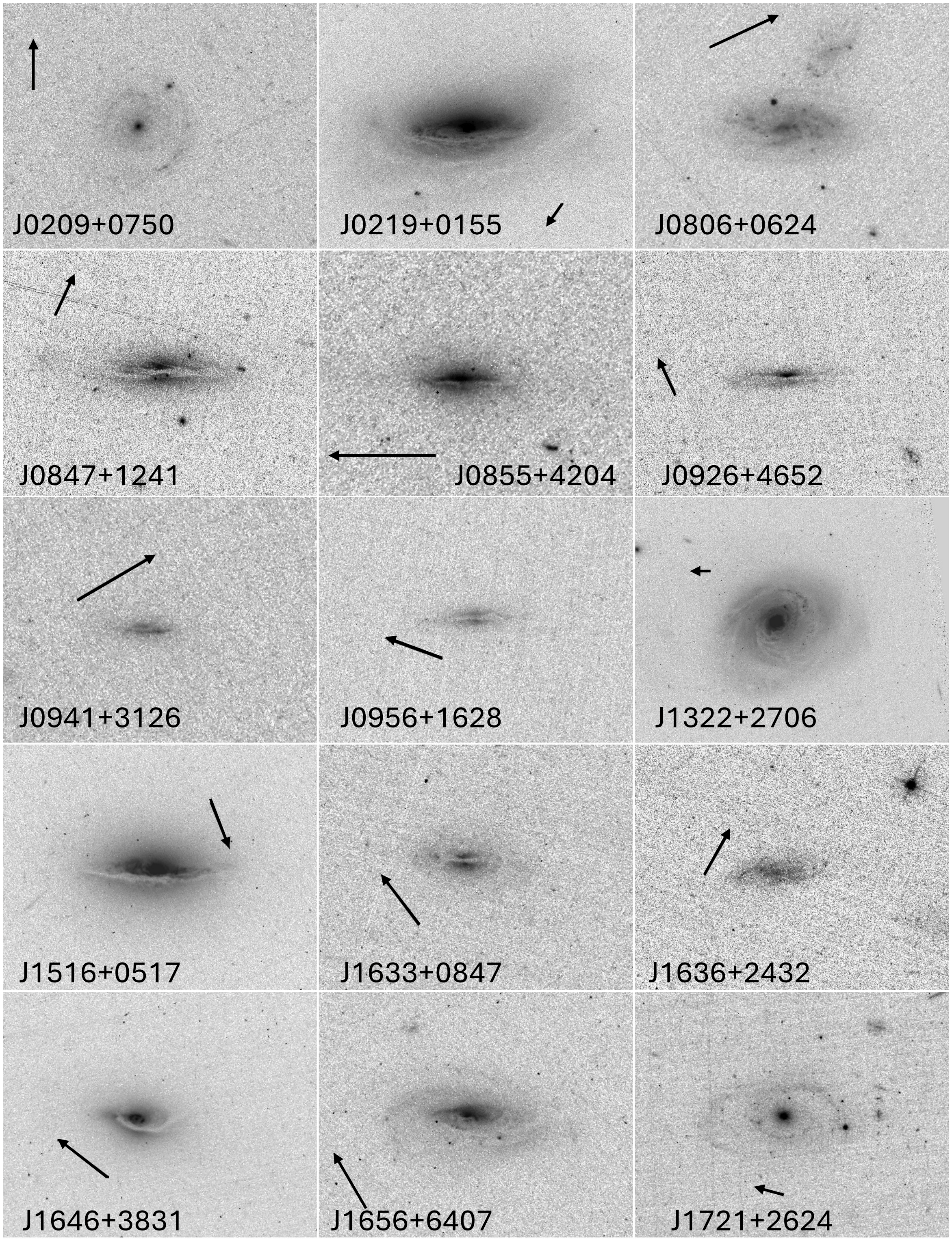

Figure 5. HST/ACS F475W images of all 15 RGZ SDRAGNs from the HST sample, in R.A. order. Various linear scales and intensity mappings, in each case offset log with a common base level, are used to show the structure of each galaxy. Each scale arrow shows 5″ and points north; images are rotated so that the projected major axes are horizontal for ease of morphological comparison. The image of J1721+2624 was smoothed with a 3 pixel (0.″15) median filter to show the galaxy structures more clearly. Some images show low-level residual background structure appearing as streaks along the original row orientations.

adopting an Hα EW criterion >3 Å to identify ionization contributions that clearly come from other sources (star formation and AGNs).

Table 6 summarizes important emission-line ratios for both previously reported SDRAGNs and the new RGZ sample. We omit J0354–1349, where the broad-line region contribution dominates the Balmer lines, so narrow-line ratios are essentially indeterminate. For J1350–1634, we measured the archival 6dFGS spectrum; a multiple-Gaussian fit to the Hα +[N II] region suggests the broad-line region contributes only

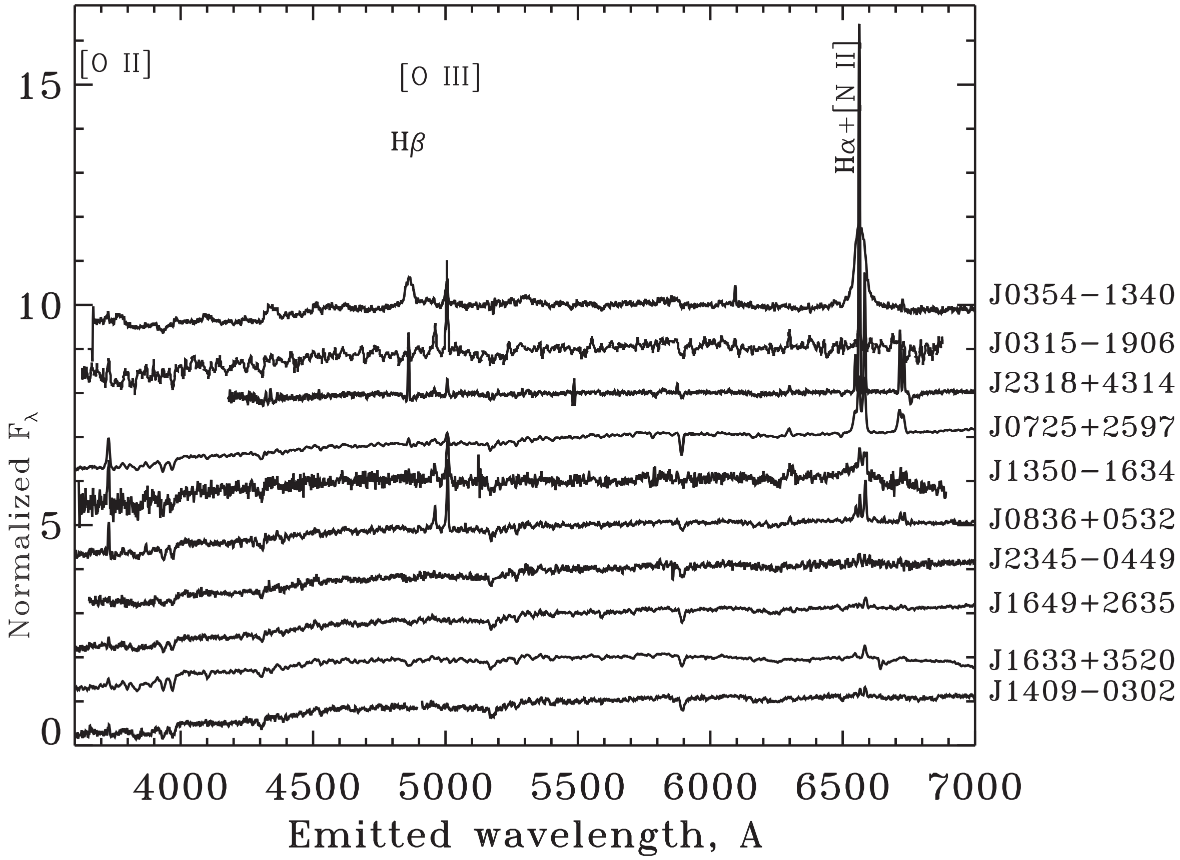

Figure 6. Optical spectra of the nuclei of previously known SDRAGNs from the sources described in Section 2.1. Each spectrum is normalized to the mean flux in the 5400–5600 Å range in the emitted frame, and each is offset in zero level by 1.0 unit from the one below for clarity. Labels at right show the adopted coordinate names as in Table 1; objects are ordered vertically to reduce overlap of emission lines. The locations of the most prominent emission lines are marked at the top. An empirical, approximate sensitivity correction was applied to the 6dFGS spectra.

Table 5
Host-galaxy Hubble Types and Orientations

Galaxy	Type		PA (deg)	Features
J0209+0750	Scd	77 ± 13	134 ± 15	Discontinuous arms, outer one ringlike with knots (like NGC 2805).
J0219+0155 (UGC 1797)	Sab	13 ± 3	127 ± 2	Dust arms, dusty inner disk, outer 20° dust warp, companion.
J0806+0624	Sc	28 ± 2	153 ± 2	Inconspicuous bulge, multiple arms, small bar.
J0847+1241	Sbc	2 ± 1	113 ±	Prominent bulge, bifurcated dust lane, edge-on.
J0855+4204	Sab	6 ± 1	178 ± 2	Prominent bulge, uneven dust lane, edge-on, like M104.
J0926+4652	Sb	2 ± 2	150 ± 2	Prominent bulge, thick dust lane tilted with respect to starlight.
J0941+3126	Sab	1 ± 1	147 ± 2	Prominent bulge, thick, extensive and warped dust lane and plume, like NGC 4402.
J0956+1628	Sb	24 ± 2	1 ± 1	Prominent bulge, uneven dust lane, like NGC 891.
J1322+2706 (IC 4234)	Sab	68 ± 22	20 ± 10	Prominent bulge, dusty arms.
J1516+0517	Sb	9 ± 3	67.3 ± 1	Dust disk, spiral features, some may be extraplanar.
J1633+0847	Sa	1 ± 1	48 ± 2	Prominent bulge, thick arcuate dust lane with likely star-forming regions.
J1636+2432	Scd	15 ± 1	125 ± 3	Diffuse arms.
J1646+3831	Sa pec	40 ± 3	30 ± 5	Central ring, tail or companion, heavy dust arm plus three ordinary ones.
J1656+6407	Sab	20 ± 1	60 ± 2	Prominent bulge, warped dust lanes, disk warp.
J1721+2624	Sc(r)	28 ± 2	19 ± 3	Prominent bulge, long arms connecting to inner ring, low surface brightness.

about 20% to the blend, which we attempt to correct in the listed line properties. For objects observed in SDSS, we adopt line measurements from either the Portsmouth or GalSpecLine processing (since these are available for different subsets of SDSS galaxies). Values for J0315−1906 are taken from M. J. Ledlow et al. (1998). For the objects with 6dFGS spectra, EWs and ratios of closely spaced lines were measured from the data-release spectra, correcting for typical stellar absorption in Hα (EW = 1.8 Å). For BTA spectra, we used Gaussian fits to 7 pixel slices along the slit, with members of the Hα+[N II] and Hβ+[O III] sets constrained to have the same FWHM. The redshifts of J0941+3126 and J0855+4204 place the red lines outside our observed spectral range. The wide redshift range spanned by this sample introduces significant aperture effects

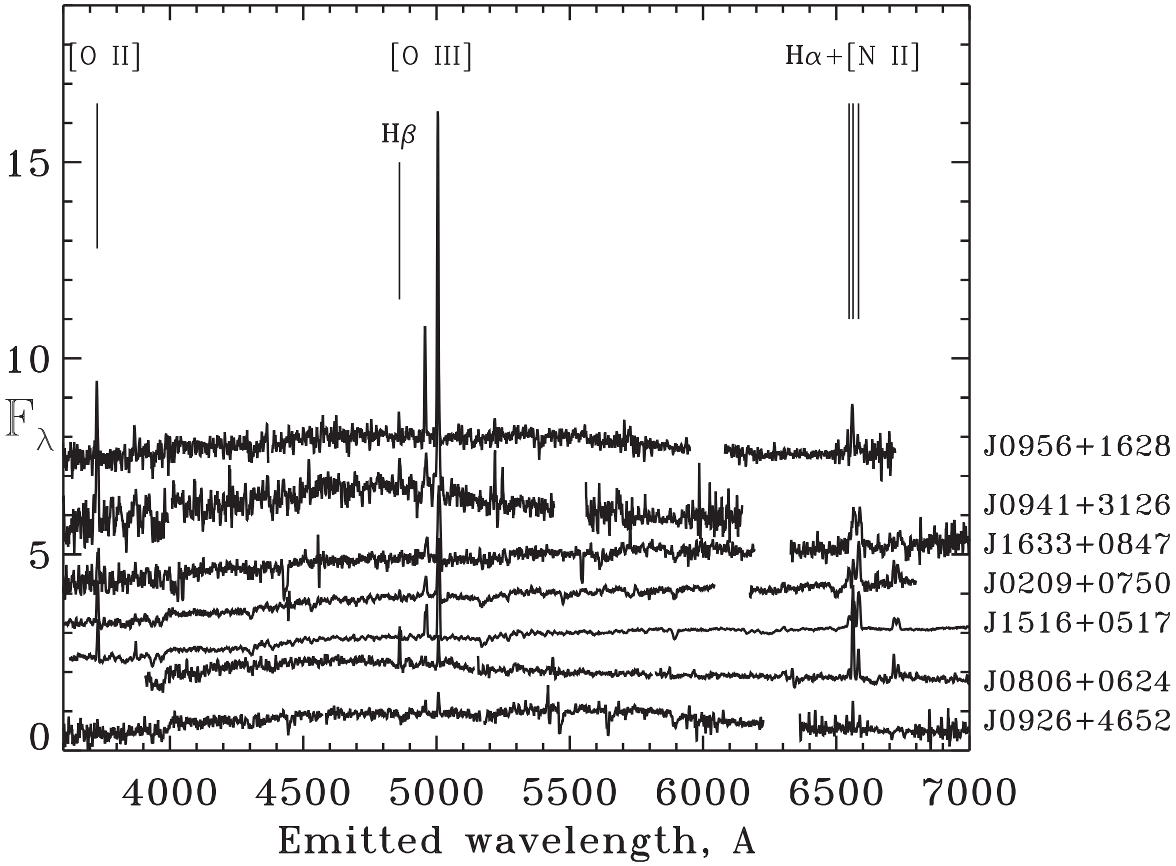

Figure 7. Optical spectra of the nuclei of newly recognized SDRAGNs from the SDSS data and BTA observations described in Section 2.6, showing the seven objects with the strongest line emission. Each spectrum is normalized to the mean flux in the 5400–5600 Å range in the emitted frame, and each is offset in zero level by 1.0 unit from the one below for clarity (2.0 units for J0956+1628 at the top). Labels at right show the truncated identifiers as in Table 11, ordered vertically by [O III] EW to reduce overlap of emission lines. Gaps in the plotted spectra show the wavelengths affected by uncorrected telluric *A*-band absorption or residuals from sky subtraction near strong [O I] airglow lines. Wavelengths of the most prominent emission lines are marked at the top.

in detecting AGN emission; in particular, surrounding star formation can mask LINER emission at levels common among early-type radio galaxies with low-excitation (or LERG) emission (P. N. Best & T. M. Heckman 2012). The final column tabulates the effective diameter included in each measurement, the diameter of a circular region with the same projected area as the region observed for each object (which is rectangular for long-slit spectra). We use the classification criteria of J. A. Baldwin et al. (1981) as updated by G. Kauffmann et al. (2003) and L. J. Kewley et al. (2001). Figure 9 shows the location of these nuclei in two Baldwin–Phillips–Terlevich (BPT) diagrams, for which the lines involved were strong enough to be well measured in most of these nuclei. We use a straightforward division at [O III] $\lambda5007/\mathrm{H}\beta = 3$ to divide LINERs from traditional AGNs. The sample is dominated by classified AGNs, plus one not shown here because its broad Balmer lines are so dominant: the narrow-line Seyfert 1 (Sy 1) J0354−1349. For many of these galaxies, Hβ is so weak as to be measured poorly or not at all; in these cases, we estimate its intensity using a typical Balmer decrement $\mathrm{H}\alpha/\mathrm{H}\beta = 4$, following the mean value for narrow-line AGNs in the SDSS from K.-X. Lu et al. (2019). This yields a conservative estimate of AGN contribution, since additional reddening also affects the [O III] lines, making them stronger relative to Hβ and moving their data point upward in Figure 9. Somewhat surprisingly, from initial visual inspection of the spectra only three likely LINERs are included, one near the boundary with star-forming regions, while the nuclear spectrum of J2318+4314 (MCG +07-47-10) is dominated by star formation. Only one of the new Zoo Gems SDRAGN candidates, J0855+4204, may have emission weak enough to fall in the "retired galaxy" or LIER category, where the gas can be ionized by hot, evolved stars (Hα EW <3 Å; R. Cid Fernandes et al. 2011). For this object, red lines of Hα and [N II] were not observed, but the [O II] $\lambda3727$ EW = 9.5 Å suggests EW(Hα) ≈3 Å. J0855+4204 is omitted from Figure 9, as only [O II] emission was detected. Among the previous discoveries, only J1649+2635 and J1633+3520 (NGC 6185) are classified as LIERs.

Roughly half of both prior and "new" SDRAGNs show emission-line ratios dominated by star formation. The spectroscopic signatures of some AGNs are almost certainly reduced in these data, both by dust obscuration and by dilution from starlight included within large projected apertures. For AGNs with the low-ionization, weak (low-EW) emission lines characteristic of many radio galaxies in early-type galaxies (ETGs), the large projected apertures at larger redshift will mingle the nuclear emission with surrounding star formation in most spiral hosts, moving the combined emission-line ratios toward the composite or star-forming regions of the BPT diagrams. In addition, for a sample with so many spirals viewed edge-on, the effects of dust lanes obscuring the nuclear regions become important; the intrinsic locations of such nuclei in the BPT diagrams are dominated by surrounding

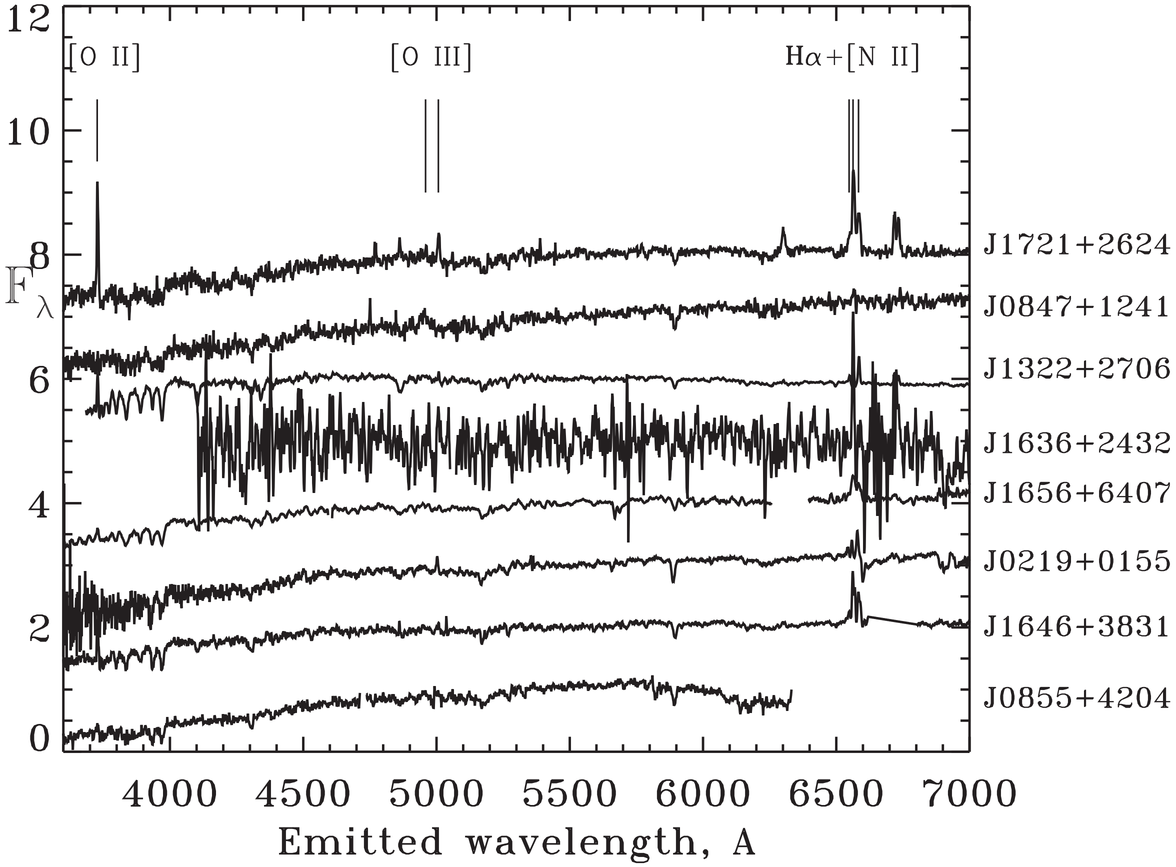

Figure 8. Optical spectra of the nuclei of newly recognized SDRAGNs from the SDSS data and BTA observations described in Section 2.6, showing the seven objects with the weakest line emission. Each spectrum is normalized to the mean flux in the 5400–5600 Å range in the emitted frame, and each offset by 1.0 unit in flux from the one below for clarity. Labels at right show the truncated identifiers as in Table 11, ordered vertically by [O III] EW to reduce overlap of emission lines. Gaps in the plotted spectra show the wavelengths affected by uncorrected telluric *A*-band absorption, residuals from sky subtraction near strong [O I] airglow lines, or SDSS data gaps. Wavelengths of the most prominent emission lines are marked at the top.

emission, so the fractional contribution of AGNs overall is at least what these diagrams imply, and quite possibly greater, since so many host radio cores commonly associated with optical AGN signatures.

In both the previously known and newly identified SDRAGN samples, few broad-line (Sy 1) spectra appear. Among the previous detections, J0354−1340 is classified as a narrow-line Seyfert 1 (NLSy 1; A. Vietri et al. 2022; see Figure 6). In the new sample, we identify a weak broad Hα component in J1633+0847, which would make this a Seyfert 1.9 (Sy 1.9) according to the widely used criteria of D. E. Osterbrock (1981). We note that the detection of weak broad components depends sensitively on the S/N of the data and the contrast of AGN emission lines against the starlight continuum. Overall, there are three Seyfert spectra among the previously reported SDRAGNs and six among the new sample, giving a fraction of $2/9 = 22\%$ of type 1 objects (including Sy 1.9). Among “classical” DRAGNs in ETGs (that is, the great majority of radio galaxies in the local Universe), broad-line radio galaxies (BLRGs) are associated exclusively with FR II radio structures (see C. Tadhunter 2016 and references therein). Since none of the new SDRAGN sources exhibits FR I morphology (Section 6), the observed incidence of BLRG (Sy 1) signatures is lower than the 21%–36% quoted by C. Tadhunter et al. (2016) for FR II galaxies in the 3CR and 2-Jy samples.

We can also compare the fraction of broad-line AGNs to samples selected from hard X-rays, e.g., the BAT AGN Spectroscopic Survey (BASS) sample selected at 14–95 keV (M. Koss et al. 2017), and from spectroscopy of optically complete (or representative) galaxy samples (the CfA and SDSS samples). Both the CfA Seyfert sample (J. P. Huchra et al. 1982) and SDSS sample at $z < 0.33$ (L. Hao et al. 2005) fortuitously match very closely in the fraction of Type I AGNs among Seyferts, at 30%. The BASS spectra are of high enough quality to be subdivided more finely; summing subtypes, 27% are in the broad-line region (BLR)-dominated Sy 1 or 1.2 categories, and 34% have weaker BLR emission in Sy 1.5–1.9. In the same way as for the identification of Sy 1.9 nuclei, these fractions are sensitive to the S/N of the optical spectra and to the contrast of the AGN emission lines against the starlight continuum, which in turn decreases with increasing measurement aperture. There may also be preferential inclusion of narrow-line objects seen through the surrounding obscuring torus, to the extent that the jets are perpendicular to the current accretion disk, an effect further amplified by having some host disks edge-on, such that disk dust hides all but the outer parts of the narrow-line region. Such effects of distant obscuration within the host galaxy are seen in narrow-line images of J0315−1906 (W. C. Keel et al. 2006), while the dust structures seen in HST images of large AGN samples (e.g., M. A. Malkan et al. 1998) show additional examples of what might be termed

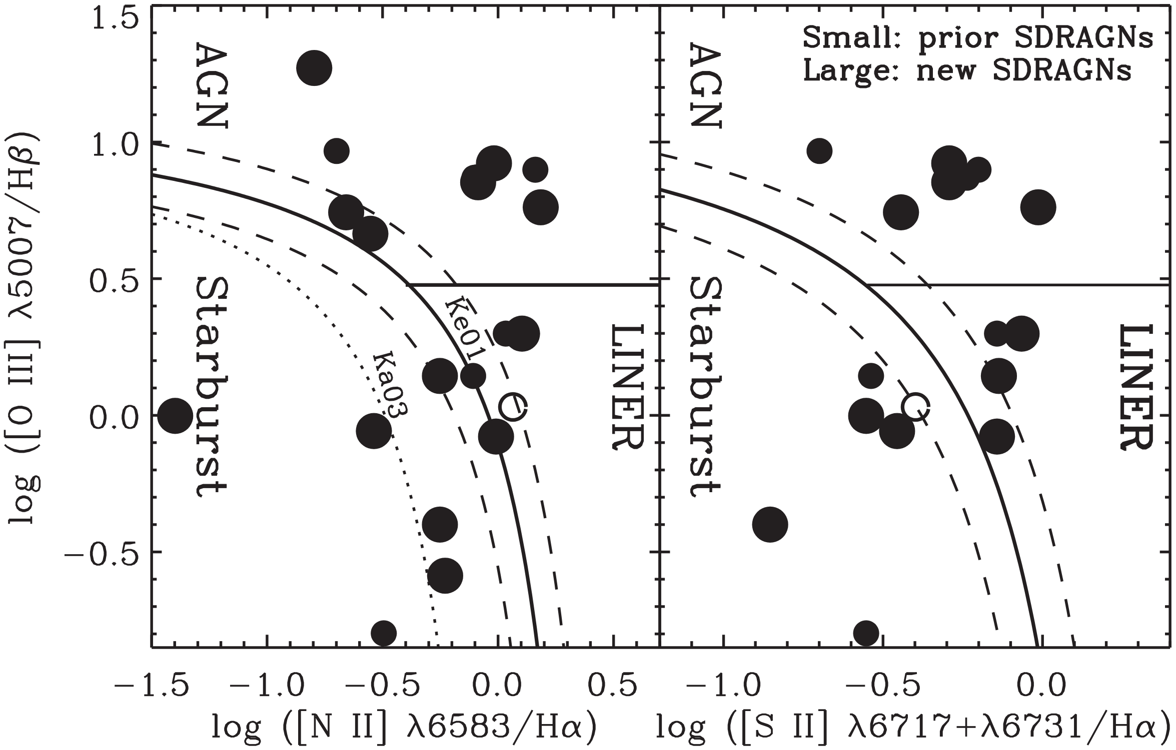

Figure 9. Two BPT diagrams illustrating the classification of SDRAGN nuclear spectra from optical data. "Ke01" and "Ka03" indicate the theoretical starburst lines from L. J. Kewley et al. (2001) and G. Kauffmann et al. (2003), respectively. For the Ke01 lines, the stated 10% uncertainty is indicated by dashed lines about the reference curve. Data for one of the two previously identified SDRAGNs with Hα EW < 3 Å, and thus potential candidates for "retired galaxy" emission, are shown with open circles; this system lies well below the maximum-starburst boundary, making it unlikely to be confused with an AGN. The second previously identified SDRAGN with weak emission, J1633+3520 (NGC 6185), has only an upper limit for [O III] and is therefore not plotted.

Table 6
Optical Emission-line Ratios

Galaxy	[N II] λ6583/Hα	[S II] λλ6717, 6731/Hα	[O III] λ5007/Hα	[O III] λ5007/Hβ	[O II] λ3727/[O III] λ5007	Hα EW (Å)	Aperture (kpc)
Previous SDRAGNs							
J0315−1906	0.20	0.20	2.33	8.18	0.055	9.6	2.1
J0725+2957	1.2	0.8	⋯	1.5	2.2	16.2	0.3
J0836+0532	1.45	0.63	1.99	9.9	0.44	5.6	5.5
J1350−1634	0.79	0.58	1.86	>3.0	0.61	9.0	11.0
J1409−0302 (Speca)	0.78	0.29	0.35	⋯	3.88	3.0	7.3
J1633+3520 (NGC 6185)	1.81	1.13	<0.29	⋯	>9.9	1.8	5.1
J1649+2635	1.16	0.40	0.54	⋯	7.90	2.1	3.2
J2318+4314 (MCG +07-47-10)	0.32	0.28	0.04	⋯	4.05	54.9	0.5
J2345−0449	0.46	⋯	<0.05	⋯	⋯	4.9	9.7
⋯	⋯	⋯	⋯	⋯	⋯	⋯	⋯
RGZ+HST SDRAGNs							
J0209+0750	1.53	0.97	1.45	7.70	0.71	8.9	13.2
J0219+0155	0.98	0.72	0.21	⋯	⋯	3.7	0.65
J0806+0624	0.29	0.35	0.35	0.79	⋯	25.0	5.1
J0847+1241	0.22	0.36	1.39	⋯	0.37	3.61	8.9
J0855+4204	⋯	⋯	⋯	⋯	>4.0	⋯	2.7
J0926+4652	0.28	⋯	1.16	⋯	0.33	8.1	6.7
J0941+3126	⋯	⋯	⋯	5.37	0.79	⋯	10.2
J0956+1628	0.16	⋯	4.69	16.45	0.22	24.5	8.0
J1322+2706	1.27	0.86	0.50	1.44	3.42	5.0	2.1
J1516+0517	0.96	0.51	2.10	4.87	0.61	11.2	3.0
J1633+0847	0.82	0.51	1.79	15.26	0.09	15.9	6.9
J1636+2432	0.04	0.28	0.25	⋯	⋯	9.0	1.8
J1646+3831	0.59	⋯	0.12	0.33	3.00	5.42	6.0
J1656+6407	0.56	0.14	0.10	⋯	1.85	11.7	6.6
J1721+2624	0.56	0.73	0.35	0.89	3.14	16.2	8.7

"accidental Seyfert 2s," where the BLR is hidden from optical view by distant dust in the host disk rather than circumnuclear structures. The unusual number of edge-on disks seen in the new SDRAGN sample surely plays a role in the obscuration of their optical AGN signatures from our vantage point. HST isophotes indicate that the true nucleus is at least partially obscured by disk dust in 8/15 of the new SDRAGNs, including the Sy 1.9 J1633+0847, three Seyfert 2 (Sy 2) nuclei, one LINER, and one star-forming nucleus. This leaves ample scope for additional broad-line nuclei to be hidden by dust within the disks of these host galaxies.

A few systems exhibit optical spectral properties not fully captured in the tabulated data. The BTA spectrum of J0855+4204 shows a quiescent stellar population with only [O II] securely detected in emission (Hα and [N II] fall beyond the observed spectral range at $z = 0.18$). J1322+2706 and J1656+6407 show high-order Balmer absorption lines, suggesting poststarburst stellar populations. J0219+0155 and J1721+2624 are LINERS with large EWs and strong [O I] λ6300 emission, placing them in the AGN subclass among LINERS.

4.4. Bulge Properties

One obvious speculation about spirals hosting powerful double radio sources is that they might contain unusually massive central black holes (M. J. Ledlow et al. 2001; W. C. Keel et al. 2006). However, this would typically imply the presence of luminous bulges, which are not observed among SDRAGNs. In fact, GALFIT decompositions by Z. Wu et al. (2022) show very few classical bulges, with the RGZ+HST sample dominated by pseudobulges.

An obvious comparison set of AGNs in spiral hosts is provided by Seyfert nuclei, which are mostly found in spirals. These have long been found to be more common in the "earlier" parts of the spiral sequence; for example spirals with Seyfert nuclei have median type indices of $T = 0$ (Sa) for Sy 1 galaxies in the IRAS 12μm sample (L. K. Hunt & M. A. Malkan 1999) and $T = 2$ (Sab) for Sy 2. In contrast, both SDRAGN samples, while spanning the whole range from Sa to Scd, have median types within the Sb ($T = 3$) bin. This comparison is consistent with the results of image decomposition, which indicate that their bulges (whether classical or pseudo) are relatively faint (in terms of bulge-to-total luminosity ratio, B/T) compared to those of typical Seyfert hosts.

4.5. Nonspiral Host Galaxies

Some host galaxies in the HST images, despite secure identifications from core radio emission, are not spirals. Since the input sample was selected for possible spirals while excluding normal elliptical systems, these outliers are morphologically interesting in themselves. They include elliptical galaxies with dust rings oriented around the projected minor axis, suggesting prolate forms, as well as ellipticals with other kinds of dust distributions and tailed merger remnants. J0802+1157, for example, is a two-tailed merger remnant with multiple bright knots and dust lanes in its main body; the VLASS data do not clearly identify the geometry of its radio source.

The combination of improved astrometry using Gaia data, HST imaging, and multiband Legacy Survey and WISE data shows that some actual hosts are distant background ETGs. In several of these cases, the extended radio source is seen through the disk of a foreground spiral, potentially allowing Faraday rotation studies of the magnetic fields in these disks. The best candidates for such Faraday investigations are J0813+5520 (foreground spiral at $z = 0.2645$), J0901+1648, J0903+4328 (foreground $z = 0.3736$), J1136+1252 (foreground $z = 0.0345$), J1328+5710 (foreground $z = 0.0211$), and J1509+5152 (likely background $z = 0.5789$).

5. Galaxy Environments

5.1. Galaxy Distributions

The structure of large-scale radio sources is shaped by interactions between emerging jets and the surrounding diffuse environment, from circumgalactic to truly intergalactic scales. We examine the environments of SDRAGNs using the galaxy distribution as a proxy for this diffuse material that shapes the radio emission. Specifically, we consider tracers based on spectroscopic redshifts, cataloged galaxy groups and clusters, and photometric redshifts, all within projected radii of 1 Mpc from the SDRAGNs.

The wide redshift range of known SDRAGNS, $z = 0.017$–0.394, limits our ability to compile uniform information on their megaparsec-scale galaxy surroundings. Using spectroscopic redshifts and cluster identifications tabulated in NED[24] or the Legacy Survey, and adopting criteria of $\Delta z < 0.005$ or $\Delta v < 1500$ km s^{-1} for physical association within a projected distance of 1 Mpc, we derive the numbers of associated galaxies listed in Table 7. A radius of 1 Mpc is appropriate for group environments, and sensitive to cluster-scale structure while not diluting the effects of groups. In this table, the number of galaxies within 1 Mpc in projection at matching redshift is denoted $N_{\rm gal}$, and the most distant of these is projected at a distance $R_{\rm max}$ from the SDRAGN. Listed cluster or group associations are centered at projected radius R and radial velocity Δv relative to the SDRAGNs. This is our most complete set of data for $z < 0.1$, where photometric redshifts in the *ugriz* system are insensitive and deep surveys may give spurious results for bright galaxies either through local background subtraction altering the fluxes, segmentation breaking single galaxies into multiple detections, or even saturation removing galaxies from a catalog. For $z < 0.2$, where group and cluster identifications are more complete, 4/10 RGZ SDRAGNs and 4/11 previously identified SDRAGNs fall in groups or clusters in both location and redshift.

For $z > 0.1$, as spectroscopic redshifts become sparse, we incorporate photometric redshifts, which now have estimated accuracy $\sigma_z = 0.05$ at $r = 22$ and $\sigma_z = 0.1$ for $r = 23.0$. Using the facilities of NOIRLab's DataLab (M. J. Fitzpatrick et al. 2014; R. Nikutta et al. 2020), we retrieved corresponding sets of galaxy coordinates, r-band magnitudes, photometric redshifts $z_{\rm phot}$ and their $\pm 1\sigma$ ranges, and spectroscopic redshifts $z_{\rm spec}$, where known, from the Legacy Survey Data Release 10 products, within cones of angular radius projecting to 1 Mpc at the SDRAGN's distance. After rejecting bright objects with $r < 16$ due to contamination by improperly measured very bright systems, we constructed a redshift distribution in each field, using $z_{\rm spec}$ where available. Respecting the accuracy of $z_{\rm phot}$, we examined these distributions when binned in widths of $\Delta z = 0.025$. While peaks corresponding to overdensities are

---

[24] https://ned.ipac.caltech.edu/.

Table 7
Galaxy Environments of RGZ and Previously Identified SDRAGNs

Object	z	Scale[a] (**arcsec Mpc^{-1}**)	$N_{\rm gal}$	$R_{\rm max}$ (Mpc)	ρ^c	Cluster/Group	R (Mpc)	Δv (km s^{-1})
RGZ/Zoo Gems								
J0209+0750	0.2552	250	0	⋯	−0.8	⋯	⋯	⋯
J0219+0155	0.0410	1227	3	0.87	⋯	Unnamed	0.32	400
J0806+0624	0.0834	634	1	0.88	0.2	⋯	⋯	⋯
J0847+1241	0.1745	335	1	0.91	2.9	⋯	⋯	⋯
J0855+4204	0.1804	326	1[a]	0.06	⋯	⋯	⋯	⋯
J0926+4652	0.2181	281	0	⋯	⋯	⋯	⋯	⋯
J0941+3126	0.3940	186	0	⋯	⋯	⋯	⋯	⋯
J0956+1628	0.2745	237	0	⋯	0.4	⋯	⋯	⋯
J1322+2706	0.0344	1451	7	0.41	⋯	MSPM 1412	0.06	402
J1516+0517	0.0512	994	21	0.95	1.4	WHL J151704.0+051522	0.16	86
J1633+0847	0.2247	275	0	⋯	−0.2	⋯	⋯	⋯
J1636+2432	0.1016	531	6	0.95	4.0	⋯	⋯	⋯
J1646+3831	0.1075	505	2	0.40	⋯	⋯	⋯	⋯
J1656+6407	0.2121	287	0	⋯	⋯	⋯	⋯	⋯
J1721+2624	0.1696	343	6	0.72	4.5	FSVS_ CL J172110+262919	0.84	213
Previous								
J0315−1906	0.0677	766	16	0.80	2.5	Abell 428	0.13	253
J0354−1340	0.0772	680	0	⋯	1.4	⋯	⋯	⋯
J0408−6247	0.0178	2747	15	0.94	⋯	LGG 110	0.24	53
J0725+2957	0.0197	2488	4	0.07	⋯	⋯	⋯	⋯
J0836+0532	0.0993	542	3	0.50	4.2	⋯	⋯	⋯
J1350−1634	0.0877	606	0	⋯	−0.5	⋯	⋯	⋯
J1409−0302	0.1376	408	6	0.76	1.8	MPSM 9045	0.42	185
J1633+3520	0.0343	1455	7	0.72	⋯	⋯	⋯	⋯
J1649+2635	0.0545	937	0	⋯	0.7	⋯	⋯	⋯
J2318+4314	0.0169	2890	8	0.92	⋯	CIZA J2318.6+4257	0.35	147
J2345−0449	0.0755	693	9	0.99	2.1	⋯	⋯	⋯

Note. "Scale" gives the projected image scale in arcseconds per megaparsec. $N_{\rm gal}$ gives the number of galaxies within $\Delta z < 0.005$ of the SDRAGN from spectroscopic data, of which the most distant within 1 Mpc in projection is seen at a projected separation $R_{\rm max}$ in megaparsecs. The density parameter ρ is the overdensity within a photometric redshift bin of width $\Delta z = 0.025$, from local galaxy density $\frac{n_{\rm gal} - \bar{n}}{\bar{n}}$, where $\bar{n}$ is normalized for large-scale variations in depth with z. When an associated cluster or group is present, R gives the projected separation of the SDRAGN from the cluster center, and Δv gives its redshift offset from the cluster mean.

[a] Galaxy serendipitously appearing on our spectrograph slit.

apparent in these distributions, we went on to estimate large-scale overdensities (of the set of galaxies included at each redshift) by treating the number of galaxies at redshifts outside density peaks as a purely heuristic power law in redshift. This includes contributions from differing survey depths between pieces of the Legacy Survey, increasing volume elements at higher redshift, and changes in the parts of the galaxy luminosity function sampled at various redshifts. We divide the distribution of galaxy number with redshift by this power law, ranging from $z^{0.9}$ to $z^{1.5}$, to estimate the amplitude of galaxy over- or underdensities at the redshifts of SDRAGNs. Legacy Survey data are not available at the locations of four of the Zoo Gems SDRAGNs as well as two of the "previous" SDRAGNs. These overdensity amplitudes ($\rho = \frac{n_{\rm gal} - \bar{n}}{\bar{n}}$ in Table 7, lacking values for $z < 0.1$ or objects outside the Legacy Survey coverage) are certainly underestimates, given the limited redshift resolution of photometric redshifts; the typical width of density peaks in redshift suggests that uncertainties of ± 0.05 are consistent with the data.

Even with these limitations, the photometric redshift distributions show that SDRAGNs are systemically located in regions of galaxy overdensity as measured in redshift, while the number of these spirals associated with clusters or rich groups also stands out. The mean values of our overdensity parameter ρ are 1.55 for the RGZ SDRAGNs, 1.74 for the previous SDRAGNs, and 1.47 for all SDRAGNs with $z > 0.1$ covered in the Legacy Survey. Even with the large line-of-sight smoothing imposed by the accuracy of photometric redshifts ($\sigma_z = 0.05$ translates to 215 Mpc in depth), the sample as a whole occupies, in the mean, the densest third of galaxy environments. Since the presence and observability of radio lobes depend on interaction with the surrounding medium, so radio luminosity correlates with the density of the surrounding medium (M. G. H. Krause et al. 2019), we broadly expect that SDRAGNs should occur preferentially in the densest regions occupied by spirals. Similarly, SDRAGNs are likely to be in gaseous environments less dense than the whole DRAGN population based on their host properties, which would be expected to manifest as lower radio powers for SDRAGNs compared to DRAGNS as a whole (R. J. Turner et al. 2023), consistent with the comparisons presented in Section 6.

5.2. Interaction Histories

A galaxy's interaction history is implicitly related to the local galaxy density, and more specifically can affect the presence of bulges and disks. Among both the RGZ and previously known SDRAGN samples, prominent tidal tails or broader fans are rare. As seen in Figure 5, only J1646+3831 shows bright features likely to be tidal in origin or indeed indicative of a disrupted companion. We do not expect to see remnants of major mergers in this sample because we select specifically for spiral patterns, which are wiped out by most such mergers. Nonetheless, given the commonly discussed connection between interactions and AGN activity, it is noteworthy that the RGZ SDRAGNs show signs of only weak recent encounters. It is equally noteworthy that many of the SDRAGNs seen close to edge-on show warped dust lanes, which can result from a weaker tidal disturbance and persist for several billion years. These include 1°–15° offsets between the observed orientations of stellar and dust disks, arcuate dust lanes that depart from the stellar plane in the same sense on both sides, and dust lanes split perpendicular to the disk—structures which often imply a thin dust distribution with a warp along the line of sight (T. Y. Steiman-Cameron et al. 1992; R. A. Nicholson et al. 1992; A. C. Quillen et al. 2006). Among systems viewed within 24° of edge-on, where dust lanes are well silhouetted, 9/10 of the RGZ SDRAGNs (Table 5) and 2/5 of the previously known SDRAGNs show such disturbed dust, suggesting weak interactions within the past 1–2 Gyr. (Two of the previous SDRAGNs with undisturbed dust, J0825+2957 and J2345−0449, have HST imaging available, so the kinds of warps seen in other systems would likely be detected in them.) We concentrate on warps visible in dust lanes, which are detectable only over the front half of the disk where backlighting is most effective. Although the statistics on warped *stellar* disks are extensive, our data do not always have sufficient S/N in the outer regions to detect them, even where we can trace dust lanes. Warped dust lanes will be observed less often even when in the same galaxies as stellar warps because of the a foreground/background distinction; dust warps are prominent only from certain directions where backlighting enhances the projected deviation from the stellar disk (which, unlike the dust, is seen more nearly integrated along the line of sight from both front and back sides of the galaxy). Among edge-on disks, the incidence of stellar warps is substantial, with reported occurrence fractions ranging from 12% (S. Laine et al. 2014) to 65% (R. de Grijs 1997; V. P. Reshetnikov et al. 2016), and there is evidence that their incidence increases in denser environments (V. P. Reshetnikov et al. 2016). Very roughly, warped dust disks should be observed 4 times less frequently than warped stellar disks in random samples of edge-on spirals, due to these front/back and angle effects.

The prevalence of pseudobulges among SDRAGNs, which suggests that the galaxies have not undergone major mergers, contrasts with the evidence for minor interactions within the past 1–2 Gyr, which would leave the kinds of disturbed dust distributions we see.

6. Radio-source Properties

6.1. Radio Power and Size Comparisons

We measured spatially integrated fluxes for the 15 RGZ SDRAGN candidates (Section 3.1) and determined the spectral index between 150 and 1400 MHz using lower-frequency LoTSS, TGSS, and RACS data. Table 8 lists the 1400 MHz flux density, the spectral index $\alpha_{150-1400}$ (in the sense $S_\nu \propto \nu^\alpha$), and the corresponding power at 1400 MHz in the emitted frame. For J1350–1634 and J1516+0517, the spectral-index fits also incorporate 151–158 MHz data from GLEAM (R. B. Wayth et al. 2015; N. Hurley-Walker et al. 2017). For comparison, Table 9 provides the LLS and 1400 MHz power for the previously identified SDRAGNs, where suitable values are available. As a representative comparison set of "ordinary" DRAGNs, overwhelmingly with host galaxies of early Hubble type, we use the FIRST sample from H. Miraghaei & P. N. Best (2017), comprising 1329 double sources with known host redshifts and 1400 MHz flux density greater than 40 mJy.

Table 8
Integrated Radio Properties of RGZ SDRAGNs

Object	z	$S_{1400\mathrm{MHz}}$, NVSS (mJy)	$\alpha_{150-1400}$	log $P_{1400\mathrm{MHz}}$ (W Hz^{-1})
J0209+0750	0.2552	395 ± 10	−0.71	25.87
J0219+0155	0.0410	555 ± 20	−0.59	24.33
J0806+0624	0.0834	5.3 ± 0.5	−0.30	22.94
J0847+1241	0.1745	11.3 ± 0.6	−1.0	23.98
J0855+4204	0.1804	177 ± 6.0	−0.66	25.18
J0926+4652	0.2181	10.7 ± 0.9	−0.75	24.15
J0941+3126	0.3940	225 ± 6	−0.76	26.05
J0956+1628	0.2745	88 ± 3	−0.64	25.28
J1322+2706	0.0344	50 ± 15	<-1.0	23.14
J1516+0517	0.0512	456 ± 15	−0.70	24.45
J1633+0847	0.2247	40 ± 5	−0.48	24.73
J1636+2432	0.1016	60 ± 2	−0.71	24.18
J1646+3831	0.1075	390 ± 13	−0.62	25.05
J1656+6407	0.2121	74 ± 3	−0.63	24.96
J1721+2624	0.1696	193 ± 8	−0.67	25.16

Broadly, the three-way comparison among typical DRAGNs, previous SDRAGNs, and RGZ+HST SDRAGNs shows that the distributions of SDRAGNs in power and LLS are similar to the overall DRAGN population, the RGZ SDRAGNs extend to larger z and $P_{1400\mathrm{MHz}}$ than the previous SDRAGNs, and the boundary between FR I and FR II sources appears at lower $P_{1400\mathrm{MHz}}$ for SDRAGNs than for general samples of double sources.

As also found by Z. Wu et al. (2022), the new Zoo Gems SDRAGN sample is dominated by FR II radio-source morphologies (1974). We find no FR I structures, and identify two radio morphologies that lack both hot spots and center-brightened jets and might be regarded as transitional between FR I and FR II. These are J1322+2706 (IC 4234), where LOFAR data show what may be two filamentary lobes partially overlapping in projection, much like the structure of Fornax A, and J1646+3831, with similar structure detected in VLASS data. Neither shows the kind of center-brightened twin jets that define FR I sources. J0219+0155 (UGC 1797) shows symmetric hot spots with additional, collimated but more diffuse emission at larger radii. All previous known SDRAGNs, except the FR I case J0725+2957 (B2 0722+30), have FR II morphologies, based on published maps and our reexamination of the 1400 MHz VLA data on J0315–1906 from M. J. Ledlow et al. (1998); its jet is one-sided and the peak lobe emission on each side is well separated from the core. The FR I/II difference has long been viewed as mostly driven by jet power, reflected in radio output, with FR II sources typically at log $P_{1400\mathrm{MHz}}$ (W Hz^{-1}) >23.93; examining this division, M. J. Ledlow & F. N. Owen (1996) found that the dividing value depends on host-galaxy properties, occurring at higher radio power for more optically luminous

Table 9
Integrated Radio Properties of Previously Identified SDRAGNs

Object	z	log $P_{1400\mathrm{MHz}}$ (W Hz^{-1})	LLS (kpc)	Data Source
J0315−1906	0.0677	24.00	350	V. Singh et al. (2015)
J0354−1350	0.0722	23.18	177	log $L_{5\ \mathrm{GHz}}$ (W Hz^{-1}) =22.87, assume $\alpha = -0.8$ (A. Vietri et al. 2022)
J0408−6247	0.0178	22.65	755	log $L_{325\ \mathrm{MHz}}$ (W Hz^{-1}) =23.99, $\alpha = -2.1$ (N. Hurley-Walker et al. 2015)
J0725+2957	0.0197	23.69	12.5	log $L_{408\ \mathrm{MHz}}$ (W Hz^{-1}) =24.11, assume $\alpha = -0.8$ (B. H. C. Emonts et al. 2009)
J0836+0532	0.0993	24.18	280	V. Singh et al. (2015)
J1350−1634	0.0877	24.72	832	S. Sethi et al. (2025)
J1409−0302	0.1376	24.85	1300	log $L_{325\ \mathrm{MHz}}$ (W Hz^{-1}) =25.36, $\alpha = -0.8$ (A. Hota et al. 2011)
J1633+3520	0.0343	⋯	2450	M. S. S. L. Oei et al. (2023)
J1649+2635	0.0545	24.03	85	V. Singh et al. (2015)
J2318+4314	0.0169	22.05	207	D. D. Mulcahy et al. (2016)
J2345−0449	0.0755	24.40	1600	V. Singh et al. (2015)

host galaxies. However, the extensive LoTSS sample analyzed by L. Clews et al. (2025) brings such a straightforward distinction into question, while still suggesting a role for the local environment in whether jets disrupt within the host galaxy or not. Excluding from either FR category the two RGZ SDRAGNs that do not fit the typical FR I/II description, FR II morphologies are seen at unusually low power $P_{1400\mathrm{MHz}}$; the only distinct FR I source is the previous SDRAGN J0725+2957 at log $P_{1400\mathrm{MHz}}$ (W Hz^{-1}) = 23.69. There are an additional three FR II sources (out of a total of 23 of both FR types) among SDRAGNs below this nominal division, one as low as log $P_{1400\mathrm{MHz}}$ (W Hz^{-1}) = 22.65. While the FR I/II luminosity division is not as well defined as once believed (B. Mingo et al. 2019; L. Clews et al. 2025), the presence of such low-power FR II sources in this small sample suggests that, in this way, SDRAGNs differ from the broader population of DRAGNS. It may be relevant, as B. Mingo et al. (2019) speculate under a paradigm where jet disruption in the surrounding medium shapes the FR I/II division, that FR II sources can occur at lower power in unusually low-density environments. We may address this possibility using galaxy environments in Section 5; since SDRAGNs occur preferentially in denser environments than average, this mechanism alone will not account for their preponderance of FR II structures even at lower power. The numerous Seyfert nuclei in spirals form a useful comparison sample of AGN in similar host galaxies. Their extended radio emission has been identified either as broad outflows, sometimes with a component driven by a circumnuclear starburst, or jets reaching only to scales of a few kiloparsecs and oriented randomly with respect to the galactic disk (A. L. Kinney et al. 2000). We might speculate (following earlier work such as J. F. Gallimore et al. 2006) that disruption of the jets in gas-rich disks, particularly for jets propagating near the disk plane, can be so complete that few FR I structures survive, while those jets that persist outside the host-galaxy ISM remain highly collimated and produce FR II structures.

The "previous" SDRAGNs are found at lower redshifts, and have correspondingly lower radio power, than our RGZ+HST sample, which was found in a project specifically examining many radio galaxies for spiral structure. Both samples span a similarly wide range in LLS as FIRST sources in general (where redshifts are known). We attribute this to the RGZ project carrying out a systematic visual as well as algorithmic search for spiral hosts, and to the use of HST images to verify spiral structure (or eliminate candidates). The RGZ SDRAGNS have mean $z = 0.163$ (median 0.169) compared to the previous SDRAGNs with mean $z = 0.063$ (median 0.068). Similarly, the RGZ SDRAGNs have mean $P_{1400\mathrm{MHz}}$ (W Hz^{-1}) = 24.63, while previous SDRAGNs have mean log $P_{1400\mathrm{MHz}}$ (W Hz^{-1}) = 23.87, a luminosity ratio of 5.7, close to the ratio of 6.7 expected for the same flux limits simply based on the mean redshifts.

In contrast, the RGZ SDRAGNs have smaller source sizes (LLS) according to several straightforward metrics, although the small sample sizes mean that the formal probability of being drawn from the same distribution, using the conservative two-sample Kolmogorov–Smirnov test, is still significant (≈30% when the direction of the difference is not specified beforehand). The median projected separations are 280 kpc for the 11 previously identified SDRAGNs versus 146 kpc for the new HST sample of 15; while the geometric mean values are 319 kpc for the previous sample versus 144 kpc for the new one. The extreme values differ in the same direction: Three of the four smallest-separation sources occur in the new HST sample (the outlier is J0725+2957, an FR I source where the lobe separation is small and ill-defined), while the two largest were previously found. Similar behavior is seen for the largest projected size (median LLS 212 kpc for the new sample versus 350 for the previous sample), with the three largest values among the previous SDRAGNs and two of the three smallest in the new sample. To some extent, these differences result from selection at different frequency bands. Several of the previously known objects show radio lobes only when observed at frequencies lower than the 3 GHz band used for VLASS. Indeed, of the two previous SDRAGNS with lobe separations exceeding 1 Mpc, the lobes of J1633+3520 (NGC 6185) were detected in LOFAR data at 144 MHz (M. S. S. L. Oei et al. 2023), while those of J2345–0449 were found in NVSS data at 45″ resolution (H. Andernach et al. 2012) and further examined using GMRT data at 325 MHz (J. Bagchi et al. 2014). For consistency, the sizes in Table 1 do not include sets of outer lobes detected only at much lower frequencies than. the NVSS: the outermost "relic" lobes of J1409−0302 (Speca) detected only at 325 MHz (A. Hota et al. 2011), and the outer pair of lobes in J1350−1634, detected at 200 and 887 MHz (S. Sethi et al. 2025).

Given the small size of even the full SDRAGN sample, we do not attempt to calculate a radio luminosity function, especially in view of the optical selection effects discussed in Section 2.5. However, we do note that the ranges of $P_{1400\mathrm{MHz}}$ and LLS are similar between SDRAGNs and ordinary

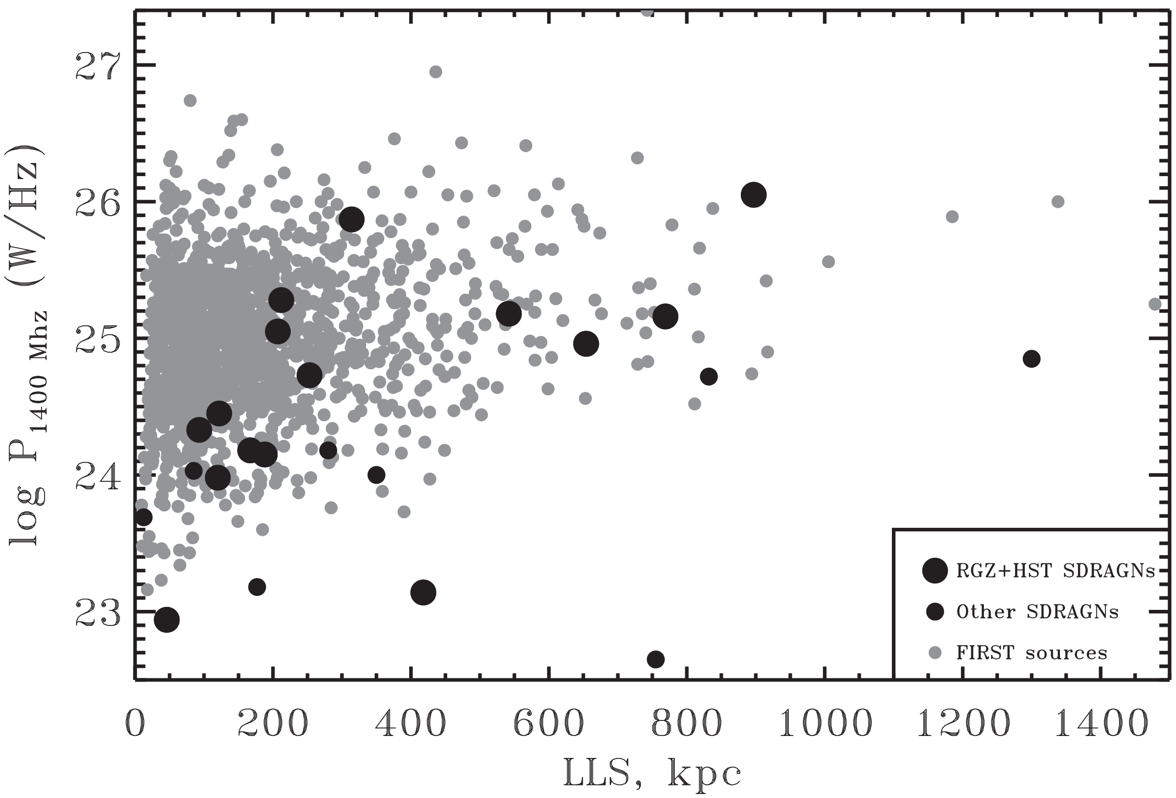

Figure 10. Distribution of the SDRAGN samples in 1400 MHz power and LLS. The new RGZ+HST SDRAGNs are shown as large black circles, smaller black circles show those previously known SDRAGNs for which flux information is available, and a comparison set of 1329 FIRST sources from H. Miraghaei & P. N. Best (2017) is shown as small gray circles. Other SDRAGNs are systematically at lower radio power than our new sample, consistent with their lower redshifts and brighter optical magnitudes. Two previous SDRAGNs are not shown: J1633+2635 would lie beyond the right edge at 2450 kpc, but its 1400 MHz power remains very poorly constrained, while J2318+4314 would lie below the bottom at 207 kpc, with log $P_{1400\mathrm{MHz}} = 22.05$.

Table 10
Core–Lobe Separations and Orientations

Object	Core ID	PA (deg)	Sep_1 (arcsec)	PA (deg)	Sep_2 (arcsec)	θ_1 (deg)	θ_2 (deg)	Sep (kpc)	LLS (kpc)
J0209+0750	Radio	−60.7 ± 1	36.1	124.3 ± 1	32.0	⋯	⋯	269	314
J0219+0155	Radio	4.7 ± 1	22.0	182.6 ± 1	19.7	32	35	32.7	93
J0806+0624	Optical	68.1 ± 5	5.2	243.0 ± 5	9.1	5	0	28.2	46
J0847+1241	Radio	4 ± 2	16.1	182 ± 2	15.2	19	21	94.5	120
J0855+4204	Optical	39 ± 2	4.6	220.3 ± 3	3.8	49	48	25	542
J0926+4652	Radio	−29 ± 2	18.4	162.6 ± 2	18.4	11	1	132	188
J0941+3126	Radio	53.5 ± 1	71.9	234.8 ± 1	83.4	3	3	829	897
J0956+1628	Radio	−49.8 ± 1	20.6	117.7 ± 1	17.3	8	19	159	212
J1322+2706	Radio	114 ± 5	137	−52 ± 5	198	7	7	190	418
J1516+0517	Radio	−82 ± 2	58.7	98 ± 1	38.6	59	59	99	122
J1633+0847	Radio	−24.7 ± 1	26.6	142.4 ± 1	28.9	17	4	197	253
J1636+2432	Optical	39.7 ± 2	43.4	218.4 ± 1	35.3	4	3	146	167
J1646+3831	Optical	161 ± 4	30	−46 ± 3	54	41	16	116	207
J1656+6407	Radio	−10.6 ± 1	70.1	170.7 ± 1	88.0	19	10	572	654
J1721+2624	Radio	68.8 ± 1	103.2	246.4 ± 1	121.5	41	43	654	769

Note. For each radio lobe, we give the position angle (PA) in degrees, north through east, and associated projected separation of the lobe peak from the galaxy nucleus. The projected angle between the implied poles of each galactic disk and the jets (1 and 2) are shown as θ_1 and θ_2. Projected lobe separations "Sep" and LLS values are shown for reference.

DRAGNs. This is illustrated in Figure 10, which compares these samples in the power–size plane. The FIRST sample's 40 mJy flux limit results in a small sampling volume at the lowest $P_{1400\mathrm{MHz}}$ values represented by SDRAGNs, as seen by the points at the bottom of the diagram. Otherwise, the joint ranges of $P_{1400\mathrm{MHz}}$ and LLS are quite similar, with a hint that large LLS values may be more common among SDRAGNs.

6.2. Orientations of Jets and Host-galaxy Disk

The dense interstellar gas in spirals compared to ellipticals might suggest that jets escape from spirals preferentially where the column densities are lowest, near the poles of the disk, a conjecture we can test using the combined SDRAGN samples. For the RGZ SDRAGNs, Table 10 lists geometrical properties

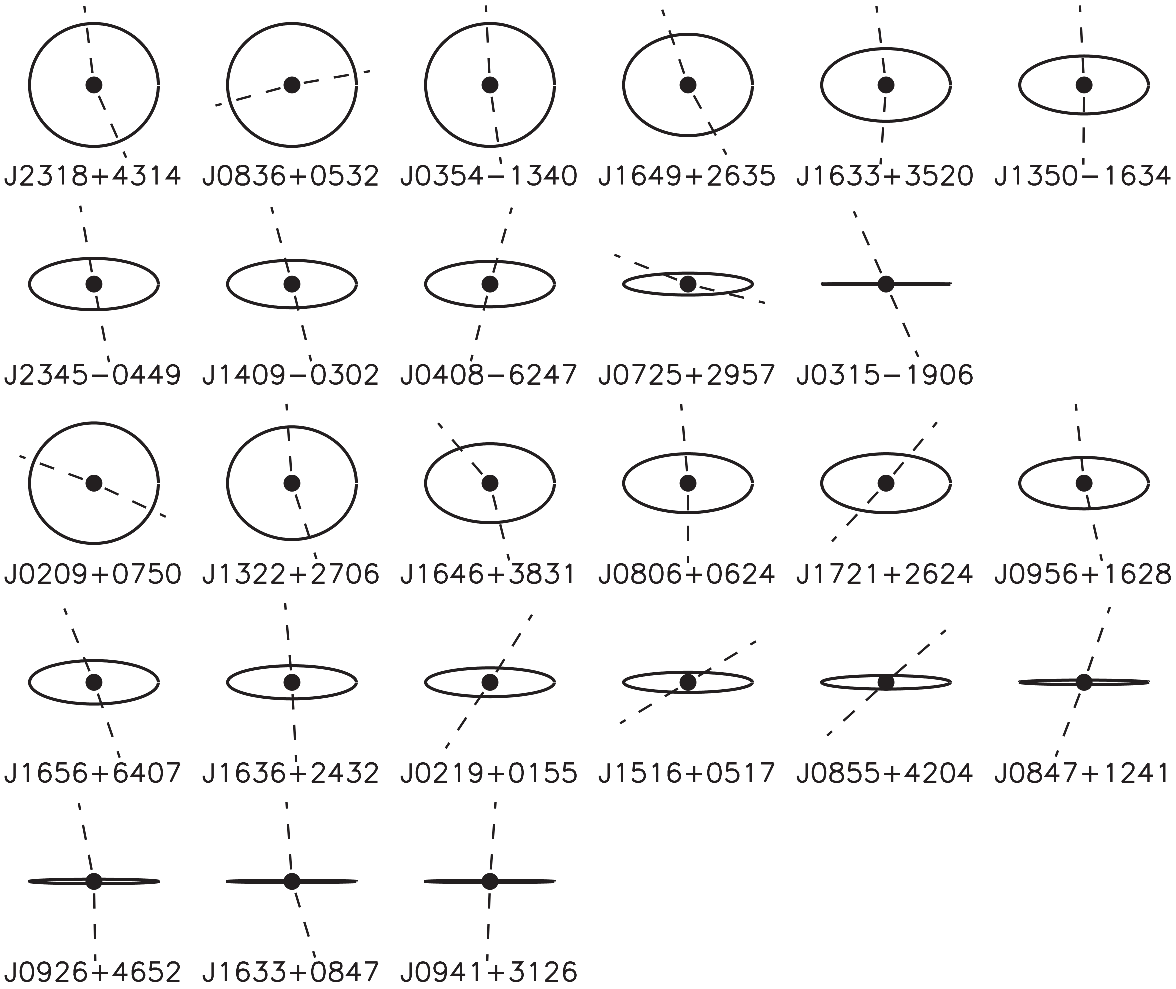

Figure 11. Graphical summary of the galaxy disk–radio jet orientations in the previously known SDRAGN sample (upper two rows) and the new RGZ SDRAGNs (lower three rows). Ellipses indicate the viewing geometry of each galactic disk (showing the adopted disk viewing angle, not the isophotal shapes), and dashed lines show the directions of the radio jets, inferred from the radio structures and pointing toward hot spots where present, even if these are not centered within the lobes, as an indicator of the most recent outflow direction. For clarity, each sample is sorted by observed disk inclination, from face-on to edge-on.

of the radio-lobe sources (separation of peaks from the core and position angle of this separation) along with the angles θ_1, θ_2 between poles of the galactic disks and each radio source (in the sense that zero indicates radio sources exactly aligned with the galaxy poles in projection). As indicated, some core positions use the optical location of the galaxy nucleus when the radio core is undetected or potentially confused with interferometric artifacts. The orientations are summarized visually, together with those of the previously known SDRAGNs, in Figure 11. These data allow us to examine the alignments between radio sources and host galaxies, since projection effects operate in different ways for various combinations of disk orientation and the (unknown) angle between the radio axis and line of sight. When we see the disks edge-on, the second angle can be treated as random and independent of the disk inclination.

Especially for the edge-on host galaxies, inspection shows that the orientation of the double source (and, by implication, jets) favors directions roughly perpendicular to the galactic disks. We can examine this quantitatively using geometry similar to the approach of C. J. Clarke et al. (1998), as extended by A. L. Kinney et al. (2000). We define the inclination i in Table 5 to be zero for edge-on galaxies, making the smaller inclination uncertainties in these systems clear, and 90° for face-on galaxies. Since the distribution of host-galaxy inclinations shows clear selection effects, we adopt a numerical approach to generate the probability distribution of the projected angle θ between the radio jets and the poles of the host-galaxy disks as simple parameters of the proposed distribution of the true angle ϕ. Using the probabilities at the observed values of i and θ, we estimate the range of acceptable distributions of ϕ. In doing this, we can combine old and new SDRAGN samples, as well as compare their separate outcomes for consistency. (The ranges of lobe separation and LAS are so wide for both old and new sets of SDRAGNs that neither quantity shows any correlation with disk inclination, nor would we plausibly expect such correlations given this sample size and range of radio sizes.)

Galaxies seen nearly edge-on convey the most information on the distribution of ϕ. If the distribution is populated only up to a limiting angle $\phi_{\max}$, there will be no systems in a region with $\theta > \theta_c$,[25] where

$$\theta_c = \tan^{-1}\frac{\tan(\phi_{\max})}{\sqrt{\cos^2(i) - \tan^2(\phi_{\max})\sin^2(i)}},$$

---

[25] Derived in response to another query, by user intelligenti pauca at https://math.stackexchange.com/questions/3728462/cone-projected-tangent-angle.

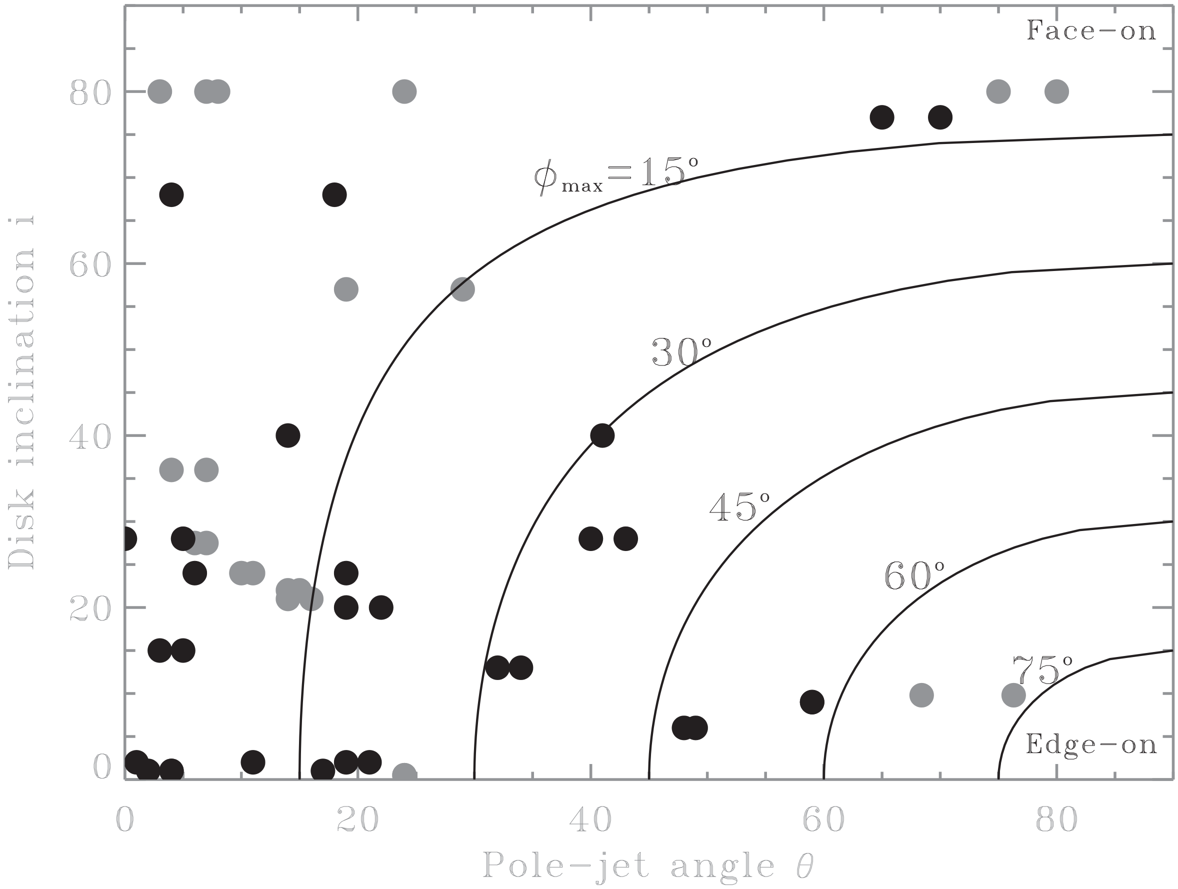

Figure 12. Distribution of the SDRAGN samples in disk inclination i and projected angle θ between the jet direction and the poles of the galactic disk. New RGZ SDRAGNs are shown as black-filled circles, and jets in previously known SDRAGNS are marked in gray. Individual jets are shown, usually giving two symbols per galaxy, except where the two jet directions are very close to 180° apart. Overlaid curves show the edges of distributions with a cutoff $\phi_{\rm max}$ in the physical distribution of pole–jet angle ϕ; regions below and to the right of each curve will be empty for the indicated $\phi_{\rm max}$. We analyze the objects with $i < 30°$, where projection effects are weakest. The "outlier" jets beyond $\phi_{\rm max} = 60°$ belong to J0725+2957, the only clear FR I source in either SDRAGN sample; the implications of including it or excluding this system in the analysis are described in the text.

which ranges from $\theta_c = \phi_{\rm max}$ at $i = 0$ to $\theta_c = 90°$ at $i = 90° - \phi_{\rm max}$. Comparison with the observed distribution of θ, i for both old and new SDRAGNs (Figure 12) gives a robust conclusion that $\phi_{\rm max} \approx 60°$ for both samples. While not a strong constraint in angle itself, this implies that roughly half of the possible solid angles for jet escape from the AGN are not seen in these samples. At face value, the previous sample satisfies $\phi_{\rm max} < 35°$. The bunching of points at small θ suggests that most systems are better aligned than these limits.

In greater detail, we can constrain the distribution of ϕ by comparing the distributions in Figure 12 with numerical realizations of simple models for the probability distribution $P(\phi)$. To do this, we use the HEALPix (K. M. Górski et al. 2005) divisions of the sphere into equal-area regions, providing convenient sets of unit-vector directions that evenly sample the sphere in solid angle.[26] We use these unit vectors to represent possible jet directions from the AGN, assigning each a weight given by a desired probability distribution in ϕ. We rotate these unit vectors to correspond to observed galactic disk inclination i, project them onto the sky plane, and derive the predicted distribution of projected pole–jet angle θ incorporating the weightings corresponding to trial distributions $P(\phi)$ and, for some purposes, differing solid angles $\propto\cos(i)$ where galactic disks are seen with inclination i. It is most convenient, remaining close to observed quantities, to consider the distributions in the (i, θ) plane. Populating 1° bins in both i and θ, we find it sufficient to use the HEALPIX order-7 sampling (196,608 points with spacing 0.45°). Slices of this plane in restricted ranges of i can be examined to isolate regimes most sensitive to $P(\phi)$ or to allow for selection effects depending on galaxy inclination.

Without assuming a form for $P(\phi)$, a simple analysis shows a grouping of jet alignments toward small ϕ. Annular ranges of ϕ project to regions in the i, θ plane that are weighted toward the largest occupied values of θ, so inward reconstruction from the largest occupied θ is feasible for systems near edge-on (we adopt $i < 30°$). One takes the outermost occupied annulus, matches the density of galaxies to its peak, and subtracts the expected contribution at smaller θ from the relevant values of ϕ, and steps inward in annuli of ϕ. Combining previous and new sets of SDRAGNs, and considering each jet rather than a mean for each galaxy, we have 30 (32 including the lone FR I source) measures with $i < 30°$, and divide these into three bins of nearly equal population: $\theta < 15°$, $15° < \theta < 30°$, and $30° < \theta < 60°$. We initially consider the sample without the single, outlying FR I source J0725+2957 (which is also the physically smallest source in projection, and for these reasons might possibly belong to a different population). Matching the

---

[26] We used the FITS files listing the coordinates from https://lambda.gsfc.nasa.gov/toolbox/pixelcoords.html.

number of jets in the outermost bin of θ and carrying out this procedure for the three bins yields fractions of jets in the three bins of ϕ as follows: 0.13 : 0.42 : 0.44 (and zero for $\phi > 60°$). These ratios imply that the fraction of jets per unit solid angle is peaked toward small values, since the solid angle included in an annulus on a sphere with inner (outer) radius ϕ_1 (ϕ_2) is $2\pi(\cos\phi_1 - \cos\phi_2)$. Specifically, for the same three annuli, the relative numbers of jets per unit solid angle are 1: 0.95 : 0.7. Given the sparse statistics, this result is consistent with a simple model in which the probability $P(\phi) =$ constant for $\phi < 30°$ and decreases linearly to zero over the range 30–60°. Fitting only those systems where the host galaxy is seen nearly edge-on avoids issues with the selection effects described in Section 2.5; it is this part of the galaxy distribution which is more sensitive to the distribution of jet–pole angles. Including the lone FR I system J0725+2957 in this fit produces somewhat paradoxical results. In order to have a significant probability of seeing a galaxy at $\theta = 75°$ in a sample of this size, without overpredicting the fraction of sources between $\theta = 30°$–$60°$, not only must $\phi_{\max}$ be at least 75°, but the drop-off for $\phi > 30°$ has to be much steeper than our assumed linear ramp, or begin at $\theta < 30°$. The current sample size does not allow a more detailed fit to the distribution $P(\phi)$, but it clearly indicates a preference for jets to emerge within 30° of the poles of the galactic disks.

This alignment of large-scale emission with the poles of the host-galaxy disk matches the alignment of (a small sample of) spirals with very-long-baseline-interferometry-scale jets analyzed by S. Kaviraj et al. (2015), but contrasts with the essentially random alignments of kiloparsec-scale emission (well within the disk radius) found for Seyfert galaxies in spiral hosts by A. L. Kinney et al. (2000). The preferential occurrence of near edge-on galaxies in this SDRAGN sample contrasts with the lack of such systems (especially for broad-line AGNs) in optically selected samples (W. C. Keel 1980; C. D. P. Lagos et al. 2011; H. M. Tovmassian & O. Yam 2011).

The analysis above, using a disk-inclination limit that respects the selection factors going into the sample, suggests a stronger trend toward radio jets perpendicular to the disks than found by Z. Wu et al. (2022). They note that this trend is strongest in galaxies with pseudobulges rather than classical bulges, since two of the three least-aligned systems in their subsample are the only ones with core Sérsic index $n > 2$, indicating classical bulges and histories including major mergers. The combination of pseudobulges and alignment of the radio jets with the poles of the host disk may indicate that important factors in the occurrence of SDRAGNs relate more to directly the SMBH spin than to (the more intuitively influential) SMBH mass. Simulations show that the spins of central black holes that have grown without major mergers are more aligned with host axes than in the general population, although the alignment for the whole sample of merger-free hosts is weaker than might have been expected (R. S. Beckmann et al. 2024; R. Smethurst et al. 2024); the angular momentum changes of gas infalling from directions out of the host plane, though substantial, may be outweighed by effects during the merger of two black holes originally at the cores of the merging galaxies.

These results are also consistent with simulations showing that jets of moderate power, in the range affected by buoyancy in a stratified ISM, can be reoriented toward the poles of a disk (E. J. Hodges-Kluck & C. S. Reynolds 2011; P. M. Yates-Jones et al. 2021). In this scenario, the host galaxy contributes to the orientation of double radio sources in a more active way than disruption of jets within the disk, and reorients some of them in directions favoring escape from the host ISM. Some SDRAGNs may show evidence of this process, where the radio-source structures on the smallest resolved scales near the nuclei in the VLA maps (Figure 3, especially in J0219+0155, J0855+4204, and J0941+3126) are less aligned with the host-disk poles than on larger scales.

7. Conclusions

We have analyzed HST images, radio structures, and optical spectra for spiral galaxies hosting large-scale double radio sources (spiral double radio active galactic nuclei, or SDRAGNs), including 11 previously known systems and 15 newly identified from RGZ and HST short-exposure data. Thirteen of the new identifications are of high probability, based on astrometric association of a radio core with the optical galaxy nucleus, while the remaining two rely on their location between the radio lobes in cases where a radio core has not been detected.

We identify selection effects with galaxy inclination operating within the SDRAGN samples, in opposite directions for brighter galaxies (seen preferentially face-on) and fainter ones (preferentially edge-on). We attribute these differences to the ability to resolve spiral structure in face-on galaxies, compared with the improved sensitivity of bulge/disk decomposition for edge-on galaxies. By subdividing the plane of galaxy inclination and angular offset between host-galaxy orientation and radio jets to isolate combinations most sensitive to the intrinsic distribution of angles ϕ between radio jets and the axes of the galactic disks, we find that radio jets in SDRAGNs preferentially escape near the disk poles. The admittedly sparse statistics are consistent with a probability distribution $P(\phi) =$ constant from 0° to 30°, declines to zero by $\phi > 60°$.

Both the previously known and newly identified subsets of SDRAGNs show distinct properties. SDRAGNs are seen preferentially close to edge-on, partly as a result of selection effects. They occur throughout the sequence of Hubble types from Sa to Scd, and most host pseudobulges rather than classical bulges (Z. Wu et al. 2022). FR II radio structures predominate, as do narrow-line (type 2) Seyfert spectra among their optical AGNs. Strong interactions or mergers are rare, but disturbed dust lanes are not. SDRAGNs are found in denser galaxy environments than average, even with the limited accuracy of photometric redshifts.

The prevalence of pseudobulges suggests that the central SMBHs have grown primarily via internal secular processes rather than through major mergers, leading to closer alignment between their spin axes and those of the host disks (both leading to accretion disks and jets aligned with the host properties as well) than found for random galaxy samples. As a result, jets emerging near the poles of the host disk and its interstellar material encounter less material to disrupt them, in contrast to the kiloparsec-scale jets seen in many spirals with Seyfert nuclei. Warped dust disks suggest that weak interactions a few billion years ago are common, perhaps increasing the flow of material to the SMBH accretion disk. The wide range of Hubble stages, and the low bulge luminosities in some systems, suggest that SMBH mass alone is not the most important factor in the occurrence of SDRAGNs.

Taken together, these factors suggest that the rarity of SDRAGNs compared to DRAGNS may result from a combination of individually rare properties, beginning with alignment between the jets and poles of the host-galaxy disk. Further large and well-quantified samples, such as those from cross-correlating Euclid and LOFAR sources (L. Bisigello et al. 2025), should allow for this idea to be tested, and further refine our understanding of how galaxies produce these large-scale radio sources.

Acknowledgments

This research is based on observations made with the NASA/ESA Hubble Space Telescope obtained from the Space Telescope Science Institute, which is operated by the Association of Universities for Research in Astronomy, Inc., under NASA contract NAS 5-26555. These observations are associated with program 15445.

Some SDRAGN candidates were identified by additional Radio Galaxy Zoo participants 1001GLEN, 958bacsal, A1001, aeolus, andymarrison, antikodon, aufelipe, axrldn, AZoo-Keeper0001, bartinhogoool, basst82, BoazWildcat, Brucea, cafeeciencia, Cardiffian, civilsparky, Claude Cornen, Corcaroli, cserfalvi, csunjoto, dude1818, ElisabethB, Emmabray, equidad1, Explorer15, firejuggler, gavinrider. graham d, Gweilouk, HannaViolet, Hruk, infoservador, jesse.rehm, jessicamh, jiipee, jo-luc, joconnell, leonie_van_vliet, lethalparadox0, Martin_Sexton, mbstone12, mdwilber, Milkybear, nico775, Olly314, ongole.geeth, OrlandoGR, Peter van Zuylen, planetari7, planetaryscience, Ptd, rezoloot, Rickss, SG1966, sharqua, southernclaw, tcwang, teamaynard, theyak330, Tony Wei, Ushiromiya Xyrius, WeBs in space, WizardHowl, wpatelunas, xDocR, and zutopian. This publication has been made possible by the participation of more than 8700 volunteers in the Radio Galaxy Zoo project. Their contributions are individually acknowledged at rgzauthors.galaxyzoo.org. We thank Rolf Jansen for a FITS version of the NGC 6185 optical spectrum and supporting information, B. Emonts for FITS versions of WHT spectra of B2 0722+30, and Frazer Owen for finding copies of the optical spectra of J0315–1906. This research has made use of the NASA/IPAC Extragalactic Database (NED), which is funded by the National Aeronautics and Space Administration and operated by the California Institute of Technology.

The National Radio Astronomy Observatory is a facility of the National Science Foundation operated under cooperative agreement by Associated Universities, Inc. This research has made use of the CIRADA cutout service at cutouts.cirada.ca, operated by the Canadian Initiative for Radio Astronomy Data Analysis (CIRADA). CIRADA is funded by a grant from the Canada Foundation for Innovation 2017 Innovation Fund (Project 35999), as well as by the Provinces of Ontario, British Columbia, Alberta, Manitoba, and Quebec, in collaboration with the National Research Council of Canada, the US National Radio Astronomy Observatory and Australia's Commonwealth Scientific and Industrial Research Organisation. LOFAR data products were provided by the LOFAR Surveys Key Science project (LSKSP, lofar-surveys.org/) and were derived from observations with the International LOFAR Telescope (ILT). LOFAR (van Haarlem et al. 2013) is the Low Frequency Array, designed and constructed by ASTRON. It has observing, data processing, and data storage facilities in several countries, which are owned by various parties (each with their own funding sources), and which are collectively operated by the ILT foundation under a joint scientific policy. The efforts of the LSKSP have benefited from funding from the European Research Council, NOVA, NWO, CNRS-INSU, the SURF Co-operative, the UK Science and Technology Funding Council, and the Jüich Supercomputing Centre.

This work is partly based on observations obtained with the 6 m telescope of the Special Astrophysical Observatory of the Russian Academy of Sciences carried out with the financial support of the Ministry of Science and Higher Education of the Russian Federation. The renovation of the telescope equipment is currently provided within the national project "Science and Universities." The work on AGN spectroscopy was performed as part of the SAO RAS government contract, approved by the Ministry of Science and Higher Education of the Russian Federation.

The Legacy Surveys project is honored to be permitted to conduct astronomical research on Iolkam Du'ag (Kitt Peak), a mountain with particular significance to the Tohono O'odham Nation. The Legacy Surveys consist of three individual and complementary projects: the Dark Energy Camera Legacy Survey (DECaLS; Proposal ID #2014B-0404; PIs: David Schlegel and Arjun Dey), the Beijing-Arizona Sky Survey (BASS; NOAO Prop. ID #2015A-0801; PIs: Zhou Xu and Xiaohui Fan), and the Mayall *z*-band Legacy Survey (MzLS; Prop. ID #2016A-0453; PI: Arjun Dey). DECaLS, BASS, and MzLS together include data obtained, respectively, at the Blanco telescope, Cerro Tololo Inter-American Observatory, NSF's NOIRLab; the Bok telescope, Steward Observatory, University of Arizona; and the Mayall telescope, Kitt Peak National Observatory, NOIRLab. NOIRLab is operated by the Association of Universities for Research in Astronomy (AURA) under a cooperative agreement with the National Science Foundation.

This project used data obtained with the Dark Energy Camera (DECam), which was constructed by the Dark Energy Survey (DES) collaboration. Funding for the DES Projects has been provided by the U.S. Department of Energy, the U.S. National Science Foundation, the Ministry of Science and Education of Spain, the Science and Technology Facilities Council of the United Kingdom, the Higher Education Funding Council for England, the National Center for Supercomputing Applications at the University of Illinois at Urbana-Champaign, the Kavli Institute of Cosmological Physics at the University of Chicago, Center for Cosmology and Astro-Particle Physics at the Ohio State University, the Mitchell Institute for Fundamental Physics and Astronomy at Texas A&M University, Financiadora de Estudos e Projetos, Fundacao Carlos Chagas Filho de Amparo, Financiadora de Estudos e Projetos, Fundacao Carlos Chagas Filho de Amparo a Pesquisa do Estado do Rio de Janeiro, Conselho Nacional de Desenvolvimento Cientifico e Tecnologico and the Ministerio da Ciencia, Tecnologia e Inovacao, the Deutsche Forschungsgemeinschaft, and the Collaborating Institutions in the Dark Energy Survey. The Collaborating Institutions are Argonne National Laboratory, the University of California at Santa Cruz, the University of Cambridge, Centro de Investigaciones Energeticas, Medioambientales y Tecnologicas-Madrid, the University of Chicago, University College London, the DES-Brazil Consortium, the University of Edinburgh, the

Eidgenossische Technische Hochschule (ETH) Zurich, Fermi National Accelerator Laboratory, the University of Illinois at Urbana-Champaign, the Institut de Ciencies de l'Espai (IEEC/CSIC), the Institut de Fisica de Altes Energies, Lawrence Berkeley National Laboratory, the Ludwig Maximilians Universitat Munchen and the associated Excellence Cluster Universe, the University of Michigan, NSF's NOIRLab, the University of Nottingham, the Ohio State University, the University of Pennsylvania, the University of Portsmouth, SLAC National Accelerator Laboratory, Stanford University, the University of Sussex, and Texas A&M University.

BASS is a key project of the Telescope Access Program (TAP), which has been funded by the National Astronomical Observatories of China, the Chinese Academy of Sciences (the Strategic Priority Research Program "The Emergence of Cosmological Structures," grant No. XDB09000000), and the Special Fund for Astronomy from the Ministry of Finance. BASS is also supported by the External Cooperation Program of Chinese Academy of Sciences (grant No. 114A11KYSB20160057) and Chinese National Natural Science Foundation (grant No. 11433005).

The Legacy Survey team makes use of data products from the Near-Earth Object Wide-field Infrared Survey Explorer (NEOWISE), which is a project of the Jet Propulsion Laboratory/California Institute of Technology. NEOWISE is funded by the National Aeronautics and Space Administration. The Legacy Surveys imaging of the DESI footprint is supported by the Director, Office of Science, Office of High Energy Physics of the U.S. Department of Energy under Contract No. DE-AC02-05CH1123; by the National Energy Research Scientific Computing Center, a DOE Office of Science User Facility under the same contract; and by the U.S. National Science Foundation, Division of Astronomical Sciences under Contract No. AST-0950945 to NOAO. This research uses services or data provided by the Astro Data Lab, which is part of the Community Science and Data Center (CSDC) program of NSF NOIRLab. NOIRLab is operated by the Association of Universities for Research in Astronomy (AURA), Inc. under a cooperative agreement with the U.S. National Science Foundation.

Facilities: HST (ACS), BAT, SARA, Astro Data Lab.

Software: IRAF (D. Tody 1986, 1993), IDL.

Appendix A
Radio Galaxy Zoo Cross-identifications

To facilitate searches in the RGZ forum discussions, Table 11 lists SDSS identifiers (used in the form SDSS J001627.47+022602.1) for all RGZ candidate SDRAGN host galaxies along with the RGZ identifiers, used in the format RGZ J020904.7+075004, and the internal RGZ alphanumeric identifiers, where these exist. RGZ coordinate names are based on KD-tree collection of locations input by volunteers; in some cases the algorithm did not converge so there is no such identifier. Due to galaxy structure, the final digits of the SDSS and RGZ coordinates do not always coincide, so we list both sets here. The table also lists the short identifier used in the text for convenience.

The precedence of catalogs used for other object names was guided by STScI coordinate resolution during Astronomer's Proposal Tool target input for Zoo Gems, deleting the hyphens required by that tool to avoid embedded spaces. This follows the common convention of preference for NGC and IC catalogs over SDSS names, and B2 and B3 radio catalogs over longer coordinate-based names.

Table 11
Host-galaxy Cross-identications and Names

Short name	SDSS	Other Name	RGZ Coordinates	Identifier
J0016+0226	J001627.47+022602.1	⋯	⋯	b001
J0209+0750	J020904.75+075004.5	⋯	J020904.7+075004	b010
J0219+0155	J021958.73+015548.7	UGC 1797	J021958.8+015555	c042
J0802+1157	J080259.73+115709.7	⋯	J080259.7+115710	a301
J0806+0624	J080658.46+062453.4	⋯	J080658.4+062453	c125
J0813+5520	J081303.10+552050.7	⋯	J081302.9+552051	b016
J0823+0330	J082312.91+033301.3	⋯	J082312.9+033301	d170
J0832+1848	J083224.82+184855.4	⋯	J083224.8+184855	c102
J0833+0457	J083351.28+045745.4	⋯	J083352.3+045814	b027
J0847+1241	J084759.90+124159.3	⋯	J084759.8+124159	c043
J0855+4204	J085549.15+420420.1	B3 0852+422	J085549.1+420420	b039
J0901+1648	J090147.17+164851.3	⋯	J090147.1+164851	c084
J0903+4328	J090305.84+432820.4	⋯	J090306.2+432817	c034
J0914+4137	J091445.53+413714.3	B3 0911+418	J091445.5+413714	a072
J0919+1359	J091949.07+135910.7	⋯	J091948.1+135951	a205
J0926+4652	J092605.17+465233.9	⋯	J092605.2+465232	c118
J0941+3126	J094103.62+312618.7	B2 0938+31A	J094103.6+312618	a248
J0956+1628	J095605.87+162829.9	⋯	J095605.8+162830	a221
J0958+5619	J095833.44+561937.8	⋯	J095833.4+561937	d093
J1128+2417	J112811.63+241746.9	⋯	J112811.6+241746	a300
J1136+1252	J113648.57+125239.7	⋯	⋯	c114
J1303+5119	J130300.80+511954.7	⋯	J130300.7+511954	d110
J1322+2706	J132259.87+270659.1	IC 4234	⋯	s008
J1328+5710	J132809.31+571023.3	⋯	J132809.1+571025	a346
J1349+4542	J134900.13+454256.5	⋯	J134901.5+454259	c103
J1354+4657	J135436.02+465701.4	B3 1352+471	J135435.8+465658	b177
J1457+2832	J145753.81+283218.7	4C +28.38	⋯	b203
J1509+5152	J150903.21+515247.9	⋯	⋯	a154
J1516+0517	J151659.24+051751.5	⋯	⋯	c051
J1613+3018	J161358.61+301809.4	B2 1611+30	⋯	a325
J1633+0847	J163300.85+084736.4	⋯	J163300.8+084736	a287
J1636+2432	J163624.97+243230.8	⋯	J163625.5+243226	b238
J1646+3831	J164628.41+383116.0	B2 1644+38	J164628.4+383115	s014
J1656+6407	J165620.58+640752.9	⋯	J165622.0+640633	s015
J1721+2624	J172107.89+262432.1	⋯	⋯	b252
J2141+0821	J214110.61+082132.6	⋯	J214110.6+082132	d106

Appendix B
Notes on Individual Sources and Identifications

SDSS J021958.73+015548.7 (UGC 1797). Z-symmetry in radio suggests precessing jets.

SDSS J080259.73+115709.7. VLASS data show complex radio structure, not a symmetric core+double. The galaxy is a two-tailed merger or merger remnant.

SDSS J080658.46+062453.4. No radio core detected, late-type spiral well centered between lobes, double radio source perpendicular to disk. Probable SDRAGN. However, a blue starlike object, SDSS J080658.59+062453.2 ($r = 20.05$), might be a background QSO hosting that radio double.

SDSS J081303.10+552050.7. Radio core outside the spiral galaxy. The actual host galaxy may not appear in the HST image, while a very red object is detected just west of the spiral in Legacy Survey data.

SDSS J082312.91+033301.3. Elliptical galaxy with multiple dust rings. Late merger remnant? Radio core, no clear double source.

SDSS J083224.82+184855.4. Double source is very asymmetric. HST image shows galaxy merger with tails and dust lanes.

SDSS J083351.28+045745.4. Complex or multiple radio sources, targeted galaxy is not obviously the AGN host.

SDSS J084759.90+124159.3. Core source only in VLASS, well aligned with edge-on spiral core. RACS shows diffuse sources $\approx 18''$N of the spiral and $\approx 1'$E of it. Too faint to say whether they may be separate sources. Diffuse emission leaves the possibility that two double are superimposed.

SDSS J085549.15+420420.1 (B3 0852+422). Z-like radio symmetry suggests precessing jets.

SDSS J090147.17+164851.3. No radio core associated with spiral. FIRST+VLASS source $0\farcs4$ from compact galaxy NW (similarly close to the interlobe line), making it the likely host identification. It is cataloged as CWISE J090146.92+164853.1 by F. Marocco et al. (2021), with a WISE W12 color index of +0.84.

SDSS J091445.53+413714.3 (B3 0911+418). The host galaxy shares features with Cen A, so we infer that it represents an advanced merger with one spiral precursor rather than an SDRAGN. The stellar component appears nearly circular, with asymmetric outer isophotes, and is crossed by a thick dust lane that is twisted and accompanied by additional dust patches on the SE side. The VLASS radio structure shows an FR II source, unlike Cen A, with an axis projected about 47° to the pole of the dust lane. At $z = 0.140$, the projected size of the radio source corresponds to 204 kpc.

SDSS J091949.07+135910.7. Weak radio core associated with dim elliptical galaxy.

SDSS J092605.17+465233.9. Symmetric double source, radio core coincident with nucleus of highly inclined spiral.

SDSS J094103.62+312618.7 (B2 0938+31A). Radio core coincident with nucleus of edge-on spiral, twisted dust lane. Double source is very prominent in LoTSS.

SDSS J095833.44+561937.8. Complex radio source, galaxy appears prolate with dust lane.

SDSS J112811.63+241746.9. No radio core, face-on spiral galaxy not quite on source axis.

SDSS J113648.57+125239.7. Nearest galaxy has very late Hubble type. Starlike object projected within 1″ of radio core, possibly contributing to SDSS fiber spectrum, is a more likely host identification.

SDSS J130300.80+511954.7. Two superimposed double sources?

SDSS J134900.13+454256.5. Asymmetric double, host galaxy unclear.

SDSS J135436.02+465701.4 (B3 1352+471). Late-type spiral or disk, bulge very faint. 1.″8 from centerline of coreless double. Faint red object (r = 24.10, z_{ph} = 1.068) DESI J208.6491+46.9510 is about 3″ WNW of the candidate SDRAGN and is a much more likely host for the E–W FR II source. The DESI object is also detected as CWISE J135435.81+465703.8 with a WISE W12 color index of 16.42 – 15.96 = 0.46.

SDSS J163300.85+084736.4. Radio core matches nucleus of M104-like edge-on spiral. Double source very asymmetric or superimposed with another source. There is a faint radio bridge in RACS, and the SE lobe is extended close to the source major axis. VLASS shows the lobe to consist of several peaks, gradually bending from the source major axis due E. Further SE there is a separate FR II source oriented perpendicular to the SDRAGN.

SDSS J163624.97+243230.8. Inclined late-type spiral right on axis at center of double source, no detected radio core. There is another possible host closer to the NE lobe, WISEA, which is faint but uncataloged in Pan-STARRS, though it is listed as DESI J249.1075+24.5446 on legacysurvey.org in DESI DR9 with z_{ph} = 0.873, aka WISEA J163625.79+243240.4 with W12 = 16.67 – 16.54 = 0.13, which would make it an FR II of 600 kpc; not unusual.

SDSS J172107.89+262432.1. RACS shows a diffuse radio bridge connecting the outer hot spots.

SDSS J214110.61+082132.6. Small double source, not centered on distorted galaxy.

Appendix C
Extended Emission-line Regions in SDSS J095833.44+561937.8

Our BTA long-slit spectrum of the radio galaxy SDSS J095833.44+561937.8 (J0958+5619) shows high-ionization emission lines spanning 22″ (85 kpc at $z = 0.24$). The emission regions, roughly symmetric east and west of the nucleus, are detectable in the g-band image from the Legacy Survey, and overlap in angle from the nucleus with the inner double radio source, but not with the other double and hot spots. The host is a normal-looking ETG with a very close companion in the HST image; we speculate that these emission clouds contributed to its appearing disklike in the original selection from SDSS images. At this redshift, our spectrum does not extend to the Hα region, so we cannot examine the clouds' location in the common BPT diagrams. However, the high [O III]/Hβ and He II/Hβ ratios in the brightest parts suggest either AGN photoionization or interaction with the radio jets. Two velocity components overlap in projection near the nucleus, separated by 180 km s^{-1}. The emission properties are shown in Figure 13.

We generated an [O III] image from Legacy Survey data, using the g- and z-band images to estimate the continuum to be subtracted from the r-band image containing [O III], varying the scaling to minimize residual starlight, following the approach from W. C. Keel et al. (2012). The detailed spatial correspondence of faint filaments in the ACS image with [O III] emission suggests that some of the extended component in the HST F475W image comes from [O II] emission in this EELR, redshifted to 4627 Å.

The emission lines are double-peaked near the nucleus; we sum the two [O III] components for line ratios since we do not have enough information to deblend the [O II] components. The velocity profile could be interpreted as showing a small central counterrotating zone.

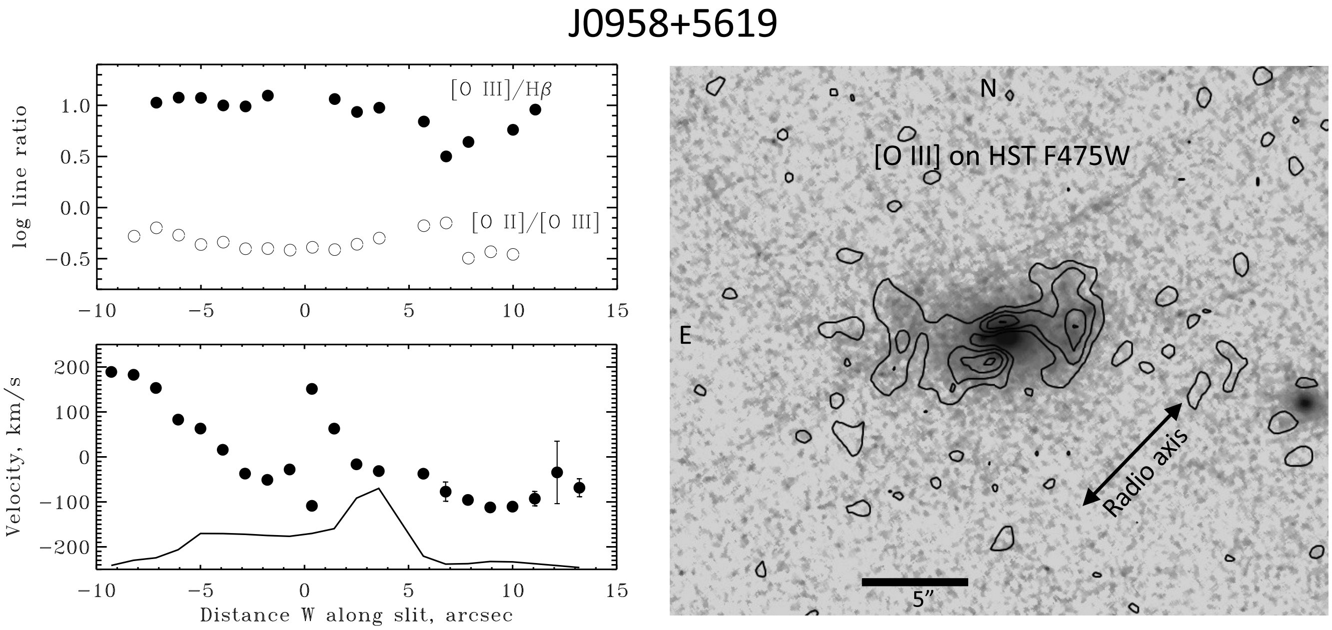

Figure 13. Extended ionized-gas structures in J0958+5619. Emission-line ratios (upper left) and radial-velocity changes relative to the mean (left) are shown along the east–west spectroscopic slit. For orientation, the velocity panel includes a trace of [O III] intensity along the slit, with zero at the bottom. Radial velocities combine both [O III] lines; the line profile is double at the center and was deblended as a pair of Gaussian profiles. Velocity error bars in most locations are smaller than the plotted points. The spectrum was summed over 3 pixel (1.″07) spans along the slit for these measurements. The image to the right overlays contours of [O III] emission derived from Legacy Survey broadband images on the HST/ACS F475W image, showing how the brightest [O III] features off the nucleus align with structures in the HST image. The double-headed arrow indicates the orientation of the radio-source axis, offset from the nucleus for clarity.

Appendix D

Starting Sample of Radio Galaxy Zoo SDRAGN Candidates

Table 12 lists the SDRAGN candidates from RGZ that were submitted to the voting used to select the final Zoo Gems target objects. Since the RGZ Talk discussion remains available online, we include the internal identifiers assigned by Jean Tate wherever possible. Broadly, identifiers beginning with *a*, *b*, or *c* are listed in that order of priority, with *s* used for some special cases. An object's status is listed as "Targ" if it was selected for the Zoo Gems target list and "Obs" if it was observed by the completion of this project. For galaxies covered by the SDSS imaging survey, this table also lists the quantities used to evaluate observation selection effects. The *r*-band magnitude is taken from the SDSS *modelMag_r* parameter, the axial ratio b/a uses the SDSS *expAB_r* value from an exponential-disk fit to each image, and the column labeled "Bulge" gives the bulge intensity fraction using *fracDev_r*.

Table 12
Candidate SDRAGN Systems and Data Status

Identifier	R.A. (deg)	Decl. (deg)	r	b/a	Bulge	Status	Internal	Cross-ID
SDSS J001627.47+022602.1	4.11447	2.43394	15.65	0.71	1.00	Obs	⋯	⋯
2MASX J01352563−0044467	23.85693	−0.74649	16.43	0.40	0.72	Targ	s023	⋯
SDSS J014200.38+054204.7	25.50160	5.70131	20.46	0.69	1.00	⋯	c132	⋯
SDSS J015744.20+024044.9	29.43420	2.67916	19.48	0.33	0.35	⋯	a316	⋯
SDSS J020904.75+075004.5	32.26980	7.83459	17.60	0.92	1.00	Obs	b010	⋯
⋯	34.99472	1.93022	13.70	0.48	0.73	Obs	c046	UGC 1797
SDSS J023832.67+023349.1	39.63614	2.56364	17.13	0.53	1.00	⋯	a098	⋯
⋯	52.15210	−28.69870	⋯	⋯	⋯	Targ	⋯	PKS 0236−288
2MASX J03283652−2841554	53.62400	−27.29090	⋯	⋯	⋯	⋯	s017	⋯
2MASX J07523474+3550235	118.14466	35.83983	16.31	0.50	0.54	⋯	s002	⋯
SDSS J075529.95+520450.6	118.87480	52.08072	17.86	1.00	0.11	⋯	b012	⋯
SDSS J080217.94+112535.0	120.57476	11.42641	17.02	0.90	0.23	⋯	a036	⋯
SDSS J080259.73+115709.7	120.74889	11.95270	17.98	0.33	0.76	Obs	a301	⋯
SDSS J080658.46+062453.4	121.74362	6.41484	18.26	0.47	0.00	Obs	c125	⋯
SDSS J081300.95+555235.1	123.25022	55.87772	16.32	0.52	0.21	⋯	a112	⋯
SDSS J081303.10+552050.7	123.26293	55.34743	19.62	0.59	0.10	Obs	b016	⋯
2MASX J08193601+5717523	124.90023	57.29787	16.33	0.36	0.53	⋯	s004	⋯
SDSS J082227.34+314059.2	125.61395	31.68313	19.73	0.73	0.00	⋯	a263	⋯
⋯	125.80381	3.55038	15.66	0.86	1.00	Obs	⋯	⋯
SDSS J082333.58+112946.1	125.88992	11.49616	19.43	0.60	0.46	⋯	b020	⋯
SDSS J083132.73+384940.3	127.88640	38.82788	19.85	0.49	0.34	⋯	b025	⋯
SDSS J083224.82+184855.4	128.10342	18.81540	16.13	0.63	1.00	Obs	c102	⋯
SDSS J083351.28+045745.4	128.46368	4.96262	19.07	0.80	0.00	Obs	b027	⋯
SDSS J083405.37+453439.2	128.52240	45.57757	18.96	0.50	0.58	⋯	a142	⋯
SDSS J083454.61+452949.2	128.72757	45.49701	19.53	0.67	0.15	⋯	a231	⋯
SDSS J084438.68+364307.8	131.16117	36.71884	17.85	0.47	0.06	⋯	b032	⋯
SDSS J084759.90+124159.3	131.99959	12.69983	17.21	0.47	0.17	Obs	c043	⋯
SDSS J084948.35+425536.9	132.45148	42.92692	20.16	0.33	0.00	⋯	b035	⋯
SDSS J085138.23+564224.9	132.90932	56.70692	21.73	0.05	0.00	⋯	b036	⋯
SDSS J085512.85+442532.1	133.80358	44.42560	19.73	0.40	0.22	⋯	a299	⋯
SDSS J085549.15+420420.1	133.95479	42.07225	18.21	0.46	0.60	Obs	b039	B3 0852+422
SDSS J085935.14+371023.1	134.89645	37.17310	19.45	0.46	0.34	⋯	c131	⋯
SDSS J090147.17+164851.3	135.44655	16.81425	18.33	0.57	0.04	Obs	c084	⋯
SDSS J090305.84+432820.4	135.77435	43.47233	19.21	0.28	0.28	Obs	c034	⋯
SDSS J091129.36+284014.3	137.87234	28.67064	19.78	0.64	0.10	⋯	b040	⋯
SDSS J091249.24+544509.4	138.20518	54.75264	19.67	0.45	0.00	⋯	a256	⋯
SDSS J091251.98+210218.9	138.21659	21.03859	20.03	0.21	0.00	⋯	c122	⋯
⋯	138.68975	41.62065	15.26	0.73	0.93	Obs	a072	B3 0911+418
SDSS J091523.47+084737.7	138.84782	8.79381	20.77	0.11	0.00	⋯	a254	⋯
SDSS J091949.07+135910.7	139.95449	13.98632	20.59	0.66	0.00	Obs	a205	⋯
SDSS J092605.17+465233.9	141.52156	46.87609	18.25	0.30	0.55	Obs	c118	⋯
SDSS J092659.94+405804.1	141.74979	40.96782	20.96	0.15	1.00	⋯	b046	⋯
SDSS J092754.96+351040.8	141.97904	35.17803	20.14	0.15	0.08	⋯	a310	⋯
SDSS J092929.50+195349.7	142.37292	19.89715	18.82	0.65	0.13	⋯	b047	⋯
SDSS J093852.70+524943.9	144.71960	52.82888	17.68	0.73	0.06	⋯	a025	⋯
SDSS J093856.16+092801.6	144.73401	9.46713	18.28	0.78	0.00	⋯	b050	⋯
SDSS J093856.30+151923.7	144.73460	15.32326	20.01	0.45	0.00	⋯	c098	⋯
SDSS J094103.62+312618.7	145.26510	31.43854	19.61	0.33	0.21	Obs	a248	B2 0938+31A
SDSS J094124.02+394441.8	145.35009	39.74496	16.12	0.51	1.00	Targ	s005	⋯
SDSS J094348.17+363540.8	145.95075	36.59468	18.44	0.40	0.24	⋯	a309	⋯
SDSS J095605.87+162829.9	149.02446	16.47500	19.26	0.39	0.24	Obs	a221	⋯
SDSS J095833.44+561937.8	149.63935	56.32717	17.81	0.64	1.00	Obs	gp102	⋯
SDSS J095846.43+260951.9	149.69349	26.16442	19.31	0.34	0.01	⋯	a271	⋯
SDSS J101316.03+171715.0	153.31681	17.28752	20.97	0.45	0.00	⋯	b063	⋯
SDSS J101529.72+550401.2	153.87385	55.06700	19.99	0.70	0.44	⋯	c117	⋯
⋯	153.99977	4.95476	14.49	0.67	0.51	Targ	⋯	Mkn 719
SDSS J101704.05+081744.9	154.26690	8.29582	16.92	0.45	0.38	Targ	a056	⋯
SDSS J102148.49+171926.3	155.45207	17.32398	18.74	0.28	0.00	Targ	c019	⋯
SDSS J102444.01+460011.4	156.18341	46.00318	20.03	0.29	0.23	⋯	b066	⋯
SDSS J102609.45+144932.7	156.53941	14.82576	17.41	0.56	0.43	Targ	b067	⋯
SDSS J102747.03+100600.7	156.94599	10.10020	21.07	0.26	0.00	⋯	a174	⋯
SDSS J103258.48+475437.3	158.24369	47.91037	19.93	0.21	0.00	⋯	b071	⋯
SDSS J103409.34+073610.9	158.53894	7.60304	21.11	0.51	0.00	⋯	a345	⋯

Table 12
(Continued)

Identifier	R.A. (deg)	Decl. (deg)	*r*	*b*/*a*	Bulge	Status	Internal	Cross-ID
SDSS J103514.94+023203.6	158.81229	2.53434	17.90	0.52	0.55	⋯	a275	⋯
⋯	159.13283	2.36225	15.51	0.74	0.09	Targ	⋯	VII Zw 090
SDSS J103635.49+483425.5	159.14791	48.57376	19.13	0.46	0.17	⋯	a183	⋯
SDSS J103932.12+461205.3	159.88384	46.20149	16.54	0.63	0.38	Targ	a090	B3 1036+464
SDSS J104018.62+281518.5	160.07761	28.25515	19.57	0.57	0.28	⋯	b076	⋯
SDSS J104151.75+483149.1	160.46564	48.53033	20.26	0.72	0.00	⋯	b077	⋯
SDSS J104201.36+090606.1	160.50569	9.10170	19.73	0.67	0.00	⋯	b079	⋯
SDSS J104459.45+280459.1	161.24773	28.08308	19.17	0.22	0.74	⋯	a222	⋯
SDSS J104616.66+181842.8	161.56945	18.31189	19.62	0.24	0.00	⋯	c101	⋯
SDSS J105023.13+035250.1	162.59639	3.88061	19.78	0.67	1.00	⋯	b085	⋯
SDSS J105452.02+552112.2	163.71677	55.35340	17.65	0.83	0.40	⋯	b091	⋯
⋯	165.56534	29.12368	15.41	0.71	1.00	Targ	b095	B2 1059+29
SDSS J111801.98+193209.1	169.50826	19.53586	18.37	0.83	0.00	⋯	b099	⋯
SDSS J111956.19+072710.2	169.98416	7.45286	20.24	0.46	1.00	⋯	b100	⋯
SDSS J112526.53+014301.5	171.36056	1.71711	19.31	0.72	1.00	Targ	⋯	⋯
SDSS J112626.44+083821.4	171.61017	8.63930	17.56	0.53	0.00	⋯	b102	⋯
SDSS J112811.63+241746.9	172.04847	24.29636	17.38	0.87	0.41	Obs	a300	⋯
SDSS J112932.83+595518.3	172.38682	59.92175	18.97	0.29	0.02	⋯	a312	⋯
SDSS J113032.02+104725.7	172.63345	10.79049	19.56	0.65	0.13	⋯	b104	⋯
SDSS J113231.69+250352.7	173.13208	25.06466	19.97	0.31	0.31	⋯	a217	⋯
SDSS J113648.57+125239.7	174.20239	12.87772	17.09	0.73	0.14	Obs	c114	⋯
SDSS J113711.82+263335.5	174.29927	26.55988	18.58	0.93	0.00	⋯	c073	⋯
SDSS J113814.89+323238.6	174.56206	32.54408	15.58	0.55	1.00	⋯	b107	⋯
SDSS J114252.21+580814.6	175.71755	58.13741	18.64	0.27	0.00	⋯	b109	⋯
⋯	177.49463	41.20262	17.78	0.44	1.00	Targ	⋯	B3 1147+414
SDSS J115029.33−021918.3	177.62222	−2.32177	18.11	0.46	0.84	⋯	s007	⋯
SDSS J115259.71+332531.1	178.24880	33.42531	18.07	0.67	0.33	⋯	a329	⋯
SDSS J115412.09+302241.7	178.55039	30.37826	19.49	0.66	0.24	⋯	b116	⋯
SDSS J115437.43+114858.9	178.65599	11.81638	18.92	0.74	1.00	⋯	b117	⋯
SDSS J115449.12+450006.4	178.70471	45.00179	19.94	0.72	0.51	⋯	a344	⋯
SDSS J115634.73+081652.5	179.14473	8.28125	19.53	0.77	0.00	⋯	b118	⋯
SDSS J115935.45+323749.7	179.89772	32.63050	19.70	0.38	0.28	⋯	b121	⋯
SDSS J120058.72+313321.7	180.24467	31.55604	18.52	0.38	0.90	Targ	⋯	3C 268.2
SDSS J120204.64+081240.8	180.51935	8.21134	19.32	0.39	0.00	⋯	b122	⋯
SDSS J120232.58+361402.8	180.63579	36.23413	20.44	0.68	0.22	⋯	a261	⋯
SDSS J120301.43+235319.9	180.75599	23.88887	17.94	0.63	1.00	Targ	a087	⋯
SDSS J120339.20+275537.2	180.91335	27.92700	19.28	0.15	0.09	Targ	a297	⋯
SDSS J120603.08+635731.4	181.51284	63.95872	19.14	0.71	0.00	⋯	b123	⋯
SDSS J120625.91+210039.0	181.60796	21.01085	18.76	0.46	0.55	⋯	c039	⋯
SDSS J120733.36+633540.4	181.88903	63.59457	20.20	0.52	0.12	⋯	b126	⋯
SDSS J121124.78+062531.9	182.85326	6.42553	19.87	0.39	0.15	⋯	c025	⋯
SDSS J121135.87+354417.4	182.89949	35.73818	15.14	0.62	1.00	Targ	⋯	KUG 1209+36
⋯	183.18710	37.52882	17.98	0.63	1.00	Targ	⋯	B3 1210+378
SDSS J121257.95+250925.4	183.24147	25.15706	18.14	0.76	0.64	Targ	a188	⋯
SDSS J122324.74+070301.9	185.85311	7.05054	17.93	0.44	0.34	Targ	⋯	⋯
SDSS J122423.61+204937.9	186.09841	20.82721	19.55	0.83	1.00	⋯	b130	⋯
SDSS J122640.22+253855.5	186.66760	25.64876	17.47	0.96	0.00	Targ	a069	⋯
SDSS J122640.85+325937.2	186.67024	32.99369	20.24	0.28	0.13	⋯	b131	⋯
SDSS J122705.12+194917.9	186.77135	19.82165	19.59	0.38	0.26	⋯	a303	⋯
SDSS J123119.74+112242.9	187.83227	11.37859	18.84	0.58	0.70	⋯	a149	⋯
SDSS J123500.21+214436.4	188.75089	21.74347	18.31	0.41	0.23	⋯	c126	⋯
SDSS J123705.70+331559.6	189.27379	33.26658	20.10	0.20	0.00	⋯	a225	⋯
SDSS J123825.49+075209.1	189.60622	7.86920	19.84	0.58	0.25	⋯	b138	⋯
SDSS J123842.36+031825.2	189.67651	3.30701	19.67	0.21	0.00	⋯	b139	⋯
SDSS J124127.34+435147.1	190.36395	43.86309	17.34	0.47	0.31	⋯	a078	⋯
SDSS J125312.97+484235.0	193.30406	48.70975	18.68	0.95	0.00	⋯	b143	⋯
SDSS J125503.07+433442.3	193.76281	43.57842	18.14	0.76	0.01	⋯	a293	⋯
SDSS J125606.71+110027.6	194.02797	11.00769	19.82	0.73	0.00	⋯	a223	⋯
SDSS J125743.34+385722.3	194.43059	38.95621	18.58	0.79	0.17	⋯	b144	⋯
SDSS J125755.81+045852.3	194.48255	4.98120	18.59	0.47	0.50	Targ	⋯	⋯
SDSS J125825.39+514226.0	194.60580	51.70724	19.61	0.60	1.00	⋯	b147	⋯
SDSS J130122.06+052353.0	195.34195	5.39806	20.18	0.93	0.00	⋯	b150	⋯
SDSS J130300.80+511954.7	195.75336	51.33188	18.37	0.60	0.09	Obs	⋯	⋯

Table 12
(Continued)

Identifier	R.A. (deg)	Decl. (deg)	r	b/a	Bulge	Status	Internal	Cross-ID
SDSS J130427.11+060319.7	196.11297	6.05549	20.24	0.43	0.14	···	b153	···
SDSS J130849.99+481852.8	197.20831	48.31468	17.54	0.70	0.60	···	a094	···
SDSS J131103.53+595504.0	197.76473	59.91778	18.88	0.65	0.53	···	a093	···
SDSS J132259.87+270659.1	200.74948	27.11643	13.69	0.82	0.89	Obs	s008	IC 4234
SDSS J132809.31+571023.3	202.03882	57.17315	16.81	0.38	0.14	Obs	···	···
SDSS J132816.05+351051.9	202.06688	35.18109	19.78	0.72	0.61	···	b161	···
SDSS J132821.46+453045.1	202.08943	45.51255	18.81	0.31	0.37	···	a253	···
SDSS J133150.72+082720.3	202.96137	8.45566	19.89	0.69	0.00	···	b163	···
SDSS J133529.16+430802.8	203.87153	43.13412	19.99	0.70	0.00	···	b164	···
SDSS J133538.98+073000.3	203.91243	7.50009	20.85	0.20	0.00	Targ	a185	···
SDSS J134147.14+043319.5	205.44646	4.55543	19.84	0.48	0.49	···	b170	···
SDSS J134849.88+353213.1	207.20786	35.53699	20.48	0.17	0.97	···	b172	···
SDSS J134900.13+452456.5	207.25058	45.71571	19.49	0.29	0.50	Obs	c103	···
SDSS J135027.27+500925.0	207.61363	50.15695	19.38	0.26	0.12	···	a232	···
SDSS J135055.29+333207.4	207.73040	33.53542	20.77	0.44	0.00	Targ	···	···
SDSS J135414.65+153118.5	208.56107	15.52182	18.94	0.23	0.77	···	b175	···
SDSS J135436.02+465701.4	208.65009	46.95042	20.01	0.31	0.17	Obs	b177	B3 1352+471
SDSS J135706.06+491844.7	209.27528	49.31244	18.06	0.85	0.00	···	b179	···
2MASX J13582118+0329136.0	209.58814	3.48704	15.48	0.82	0.84	···	s009	···
SDSS J135856.20+432708.6	209.73420	43.45239	19.06	0.37	0.00	···	c035	···
SDSS J140917.76+325925.4	212.32403	32.99040	18.31	0.71	0.25	···	b183	···
SDSS J140932.69+415107.0	212.38622	41.85195	20.13	0.21	0.00	···	b184	···
SDSS J141558.81+132023.7	213.99505	13.33992	19.05	0.41	0.43	···	a109	···
SDSS J142305.86+215735.5	215.77444	21.95988	18.18	0.63	0.14	···	a314	···
SDSS J142558.12+300931.2	216.49217	30.15869	18.22	0.56	0.24	···	a229	···
SDSS J142606.19+402432.0	216.52580	40.40889	19.85	0.34	1.00	···	b191	···
SDSS J142647.80+581756.3	216.69918	58.29900	20.08	0.46	0.00	···	c071	···
SDSS J143340.75+635830.4	218.41979	63.97513	16.20	0.56	0.98	···	s010	···
SDSS J143447.95+165631.8	218.69981	16.94218	21.21	0.80	0.68	···	b195	···
SDSS J143507.46+225414.0	218.78112	22.90389	20.62	0.66	0.00	···	b196	···
SDSS J143554.21+360853.0	218.97591	36.14807	18.66	0.93	0.06	···	a337	···
SDSS J143643.83+080728.3	219.18263	8.12454	14.49	0.68	1.00	Targ	s011	CGCG 047−115
SDSS J143854.46−015646.9	219.72696	−1.94637	18.52	0.30	0.01	···	s012	···
SDSS J143934.48+531437.0	219.89368	53.24363	19.34	0.35	0.00	···	b197	···
2MASX J14425854+5209018	220.74427	52.15058	17.92	0.67	1.00	···	s013	···
SDSS J144714.49+424723.4	221.81040	42.78985	19.18	0.39	0.01	···	b198	···
SDSS J144915.64+335835.7	222.31517	33.97660	19.87	0.46	0.16	···	b201	···
SDSS J145218.00+052105.5	223.07501	5.35155	20.06	0.38	0.00	···	a212	···
SDSS J145753.81+283218.7	224.47424	28.53854	16.22	0.68	0.48	Obs	b203	4C +28.38
SDSS J145847.52+561035.6	224.69800	56.17658	19.32	0.83	1.00	···	b204	···
SDSS J145914.09+315740.9	224.80874	31.96139	18.09	0.23	0.27	···	b205	···
SDSS J150326.21+304817.1	225.85924	30.80477	21.21	0.11	0.47	···	b206	···
SDSS J150440.06+071109.6	226.16693	7.18602	18.95	1.00	1.00	···	b207	···
SDSS J150543.38+195304.0	226.43077	19.88447	20.01	0.53	0.00	···	a317	···
SDSS J150903.21+515247.9	227.26340	51.87999	19.59	0.67	1.00	Obs	a154	···
SDSS J151356.33+572523	228.48475	57.42310	18.04	0.42	0.82	···	b210	···
SDSS J151659.24+051751.5	229.24684	5.29764	15.29	0.57	0.93	Obs	c051	···
SDSS J151918.35+103505.1	229.82646	10.58477	20.02	0.55	0.07	···	c127	···
SDSS J155046.42+173630.2	229.87631	6.56453	19.57	0.51	0.00	Targ	···	···
SDSS J152207.70+325113.3	230.53209	32.85372	22.54	0.60	0.00	···	s021	···
SDSS J152838.43+242025.6	232.15475	24.23822	18.95	0.66	0.00	Targ	···	···
SDSS J152955.47+344955.2	232.48115	34.83201	19.92	0.11	0.00	···	a250	···
SDSS J152955.55+344943.0	232.48146	34.82862	20.63	1.00	1.00	···	a283	···
SDSS J153200.95+272528.9	233.00397	27.42470	18.66	0.91	0.16	Targ	b217	···
SDSS J153233.17+241525.7	233.13823	24.25716	19.80	0.71	0.61	···	b218	···
SDSS J153250.68+573424.9	233.21118	57.57359	17.39	0.83	0.15	···	a080J	···
SDSS J153637.22+120746.1	234.15512	12.12948	19.43	0.55	0.05	···	a286	···
SDSS J153917.23+075953.1	234.82183	7.99809	19.69	0.22	0.00	···	a276	···
SDSS J154053.15+533002.0	235.22150	53.50057	18.15	0.88	0.00	···	a339	···
SDSS J154502.82+513500.8	236.26176	51.58356	17.55	0.68	1.00	···	b224	···
SDSS J154814.62+483502.0	237.06093	48.58390	19.86	0.46	1.00	···	a192	···
SDSS J154826.32+581313.9	237.10968	58.22055	19.06	0.72	1.00	···	b226	···
SDSS J155046.42+173630.2	237.69342	17.60840	17.28	0.80	0.68	Targ	···	···

Table 12
(Continued)

Identifier	R.A. (deg)	Decl. (deg)	r	b/a	Bulge	Status	Internal	Cross-ID
SDSS J155126.62+534814.7	237.86092	53.80410	20.55	0.06	0.00	⋯	b228	⋯
SDSS J155203.47+073141.9	238.01446	7.52833	18.73	0.53	0.20	⋯	a331	⋯
SDSS J155549.80+241409.9	238.95751	24.23610	21.52	0.44	0.00	⋯	b229	⋯
SDSS J155619.77+511848.8	239.08240	51.31356	18.32	0.83	0.60	⋯	a139	⋯
SDSS J155641.93+245941.1	239.17475	24.99477	20.58	0.48	0.96	⋯	a177	⋯
SDSS J160057.30+051438.4	240.23876	5.24402	21.24	0.11	0.00	⋯	c092	⋯
SDSS J161358.61+301809.4	243.49423	30.30263	19.00	0.40	0.00	Obs	a325	B2 1611+30
SDSS J161449.71+321054.5	243.70714	32.18181	20.45	0.75	0.61	⋯	b233	⋯
SDSS J161948.86+300607.8	244.95360	30.10218	17.94	0.93	0.58	Targ	⋯	⋯
SDSS J163218.08+475616.3	248.07534	47.93787	22.63	0.09	1.00	⋯	b237	⋯
SDSS J163300.85+084736.4	248.25358	8.79346	17.84	0.58	0.49	Obs	a287	⋯
SDSS J163624.97+243230.8	249.10407	24.54191	19.69	0.38	0.00	Obs	b238	⋯
SDSS J163901.65+243139.8	249.75690	24.52775	21.86	0.74	0.00	⋯	b239	⋯
SDSS J164351.20+424953.6	250.96333	42.83157	19.34	0.66	0.00	⋯	b240	⋯
SDSS J164604.10+513024.0	251.51710	51.50668	21.65	0.05	0.96	⋯	b241	⋯
2MASX J16462838+3831156	251.61841	38.52112	16.66	0.64	0.95	Obs	s014	B2 1644+38
SDSS J165304.66+240409.2	253.26944	24.06925	17.93	0.41	0.25	Targ	b245	⋯
2MASX J16562058+6407529	254.08586	64.13138	16.96	0.44	0.53	Obs	s015	⋯
SDSS J170008.72+291903.7	255.03634	29.31771	16.52	0.73	0.00	⋯	s022	⋯
SDSS J170953.87+410503.8	257.47449	41.08441	18.34	0.49	0.38	⋯	b248	⋯
SDSS J171845.25+364911.0	259.68856	36.81973	21.84	0.29	0.95	⋯	b250	⋯
SDSS J172107.89+262432.1	260.28291	26.40894	17.77	0.94	1.00	Obs	⋯	⋯
SDSS J172853.38+342348.1	262.22242	34.39671	19.71	0.69	0.29	⋯	a307	⋯
SDSS J214110.61+082132.6	325.29424	8.35906	19.25	0.45	0.70	Obs	⋯	⋯
SDSS J214530.21+104949.2	326.37591	10.83036	19.03	0.30	1.00	⋯	b255	⋯
SDSS J231620.15−010207.3	349.08399	−1.03537	18.79	0.62	0.63	⋯	s016	⋯

Note. Objects observed in the HST filler program are denoted by "Obs"; "Targ" indicates objects that were selected for the HST program but not observed due to the essentially random selection of targets for scheduling. Both these subsets reflect the observational selections going into the HST sample.

(This table is available in machine-readable form in the online article.)

ORCID iDs

William C. Keel https://orcid.org/0000-0002-6131-9539
O. Ivy Wong https://orcid.org/0000-0003-4264-3509
Heinz Andernach https://orcid.org/0000-0003-4873-1681
Alexei Moiseev https://orcid.org/0000-0002-0507-9307
Brooke D. Simmons https://orcid.org/0000-0001-5882-3323

References

Aguado, D. S., Ahumada, R., Almeida, A., et al. 2019, ApJS, 240, 23
Ahn, C. P., Alexandroff, R., Allende Prieto, C., et al. 2014, ApJS, 211, 17
Afanasiev, V. L., & Moiseev, A. V. 2005, AstL, 31, 194
Afanasiev, V. L., & Moiseev, A. V. 2011, BaltA, 20, 363
Alam, S., Albareti, F. D., Allende Prieto, C., et al. 2015, ApJS, 219, 12
Albareti, F. D., Allende Prieto, C., Almeida, A., et al. 2017, ApJS, 233, 25
Andernach, H., Jiménez Andrade, E. F., Maldonado Sánchez, R. F., et al. 2012, Science from the Next Generation Imaging and Spectroscopic Surveys (European Southern Observatory), P1
Bagchi, J., Ray, S., Dhiwar, S., et al. 2025, MNRAS, 538, 1628
Bagchi, J., Vivek, M., Vikram, V., et al. 2014, ApJ, 788, 174
Baldwin, J. A., Phillips, M. M., & Terlevich, R. 1981, PASP, 93, 5
Banfield, J. K., Wong, O. I., Willett, K. W., et al. 2015, MNRAS, 453, 2326
Becker, R. H., White, R. L., & Helfand, D. J. 1995, ApJ, 450, 559
Beckmann, R. S., Smethurst, R. J., Simmons, B. D., et al. 2024, MNRAS, 527, 10867
Belfiore, F., Maiolino, R., Maraston, C., et al. 2016, MNRAS, 461, 3111
Best, P. N., & Heckman, T. M. 2012, MNRAS, 421, 1569
Best, P. N., Kauffmann, G., Heckman, T. M., et al. 2005, MNRAS, 362, 25
Bisigello, L., Giulietti, M., Prandoni, I., et al. 2025, OJAp, 8, 101
Buta, R. J., Corwin, H. G., & Odewahn, S. C. 2007, in The de Vaucouleurs Atlas of Galaxies, ed. R. J. Buta, H. G. Corwin, & S. C. Odewahn (Cambridge Univ. Press)
Capetti, A., de Ruiter, H. R., Fanti, R., et al. 2000, A&A, 362, 871
Cid Fernandes, R., Stasińska, G., Mateus, A., et al. 2011, MNRAS, 413, 1687
Clarke, C. J., Kinney, A. L., & Pringle, J. E. 1998, ApJ, 495, 189
Clews, L., Croston, J. H., Dickinson, H., et al. 2025, MNRAS, 541, 3452
Condon, J. J. 1997, PASP, 109, 166
Condon, J. J., Cotton, W. D., Greisen, E. W., et al. 1998, AJ, 115, 1693
de Grijs, R. 1997, Ph.D. Thesis, Univ. Groningen, Kapteyn Astronomical Institute
de Koff, S., Best, P., Baum, S. A., et al. 2000, ApJS, 129, 33
Dey, A., Schlegel, D. J., Lang, D., et al. 2019, AJ, 157, 168
Duric, N., & Seaquist, E. R. 1988, ApJ, 326, 574
Emonts, B. H. C., Tadhunter, C. N., Morganti, R., et al. 2009, MNRAS, 396, 1522
Fanaroff, B. L., & Riley, J. M. 1974, MNRAS, 167, 31P
Fasano, G., Falomo, R., & Scarpa, R. 1996, MNRAS, 282, 40
Fitzpatrick, M. J., Olsen, K., Economou, F., et al. 2014, SPIE, 9149, 91491T
Ford, H. C., Bartko, F., Bely, P. Y., et al. 1998, SPIE, 3356, 234
Gallimore, J. F., Axon, D. J., O'Dea, C. P., et al. 2006, AJ, 132, 546
Garon, A. F., Rudnick, L., Wong, O. I., et al. 2019, AJ, 157, 126
Gopal-Krishna, Mhaskey, M., Wiita, P. J., et al. 2012, MNRAS, 423, 1053
Górski, K. M., Hivon, E., Banday, A. J., et al. 2005, ApJ, 622, 759
Hao, L., Strauss, M. A., Tremonti, C. A., et al. 2005, AJ, 129, 1783
Harnett, J. I., Whiteoak, J. B., Reynolds, J. E., et al. 1990, MNRAS, 244, 130
Heckman, T. M., Miley, G. K., Balick, B., et al. 1982, ApJ, 262, 529
Heckman, T. M., Smith, E. P., Baum, S. A., et al. 1986, ApJ, 311, 526
Hodges-Kluck, E. J., & Reynolds, C. S. 2011, ApJ, 733, 58
Hota, A., Sirothia, S. K., Ohyama, Y., et al. 2011, MNRAS, 417, L36
Huchra, J. P., Wyatt, W. F., & Davis, M. 1982, AJ, 87, 1628
Hunt, L. K., & Malkan, M. A. 1999, ApJ, 516, 660
Hurley-Walker, N., Callingham, J. R., Hancock, P. J., et al. 2017, MNRAS, 464, 1146

Hurley-Walker, N., Johnston-Hollitt, M., Ekers, R., et al. 2015, MNRAS, 447, 2468

Jackson, N., Beswick, R., Pedlar, A., et al. 2003, MNRAS, 338, 643

Jamrozy, M., Kozieł-Wierzbowska, D., Zoła, S., et al. 2011, JApA, 32, 467

Jansen, R. A., Fabricant, D., Franx, M., et al. 2000, ApJS, 126, 331

Jones, D. H., Read, M. A., Saunders, W., et al. 2009, MNRAS, 399, 683

Jones, D. H., Saunders, W., Colless, M., et al. 2004, MNRAS, 355, 747

Kauffmann, G., Heckman, T. M., Tremonti, C., et al. 2003, MNRAS, 346, 1055

Kaviraj, S., Shabala, S. S., Deller, A. T., et al. 2015, MNRAS, 454, 1595

Keel, W. C. 1980, AJ, 85, 198

Keel, W. C., Chojnowski, S. D., Bennert, V. N., et al. 2012, MNRAS, 420, 878

Keel, W. C., Oswalt, T., Mack, P., et al. 2017, PASP, 129, 015002

Keel, W. C., Tate, J., Wong, O. I., et al. 2022, AJ, 163, 150

Keel, W. C., White, R. E., Owen, F. N., et al. 2006, AJ, 132, 2233

Kewley, L. J., Dopita, M. A., Sutherland, R. S., et al. 2001, ApJ, 556, 121

Kinney, A. L., Schmitt, H. R., Clarke, C. J., et al. 2000, ApJ, 537, 152

Koss, M., Trakhtenbrot, B., Ricci, C., et al. 2017, ApJ, 850, 74

Krause, M. G. H., Hardcastle, M. J., & Shabala, S. S. 2019, A&A, 627, A113

Lacy, M., Baum, S. A., Chandler, C. J., et al. 2020, PASP, 132, 035001

Lagos, C. D. P., Padilla, N. D., Strauss, M. A., et al. 2011, MNRAS, 414, 2148

Laine, S., Knapen, J. H., Muñoz-Mateos, J.-C., et al. 2014, MNRAS, 444, 3015

Lamer, G., Newsam, A. M., & McHardy, I. M. 1999, MNRAS, 309, 1085

Leahy, J. P. 1993, LNP, 421, 1

Ledlow, M. J., & Owen, F. N. 1996, AJ, 112, 9

Ledlow, M. J., Owen, F. N., & Keel, W. C. 1998, ApJ, 495, 227

Ledlow, M. J., Owen, F. N., Yun, M. S., et al. 2001, ApJ, 552, 120

Lu, K.-X., Zhao, Y., Bai, J.-M., et al. 2019, MNRAS, 483, 1722

Lupton, R., Blanton, M. R., Fekete, G., et al. 2004, PASP, 116, 133

Malkan, M. A., Gorjian, V., & Tam, R. 1998, ApJS, 117, 25

Mao, M. Y., Blanchard, J. M., Owen, F., et al. 2018, MNRAS, 478, L99

Mao, M. Y., Owen, F., Duffin, R., et al. 2015, MNRAS, 446, 4176

Marocco, F., Eisenhardt, P. R. M., Fowler, J. W., et al. 2021, ApJS, 253, 8

Masters, K. L., Nichol, R., Bamford, S., et al. 2010, MNRAS, 404, 792

Matthews, T. A., Morgan, W. W., & Schmidt, M. 1964, ApJ, 140, 35

McConnell, D., Hale, C. L., Lenc, E., et al. 2020, PASA, 37, e048

McLean, B., Rodriguez, D., & Hack, W. 2020, AAS, 235, 109.29

Middelberg, E., Norris, R. P., Cornwell, T. J., et al. 2008, AJ, 135, 1276

Mingo, B., Croston, J. H., Hardcastle, M. J., et al. 2019, MNRAS, 488, 2701

Miraghaei, H., & Best, P. N. 2017, MNRAS, 466, 4346

Morganti, R., Holt, J., Tadhunter, C., et al. 2011, A&A, 535, A97

Mulcahy, D. D., Mao, M. Y., Mitsuishi, I., et al. 2016, A&A, 595, L8

Mutie, I. M., Williams-Baldwin, D., Beswick, R. J., et al. 2024, MNRAS, 527, 11756

Nagar, N. M., Wilson, A. S., Mulchaey, J. S., et al. 1999, ApJS, 120, 209

Nicholson, R. A., Bland-Hawthorn, J., & Taylor, K. 1992, ApJ, 387, 503

Nikutta, R., Fitzpatrick, M., Scott, A., et al. 2020, A&C, 33, 100411

Norris, R. P., Afonso, J., Appleton, P. N., et al. 2006, AJ, 132, 2409

Oei, M. S. S. L., van Weeren, R. J., Hardcastle, M. J., et al. 2023, MNRAS, 518, 240

Osterbrock, D. E. 1981, ApJ, 249, 462

Padilla, N. D., & Strauss, M. A. 2008, MNRAS, 388, 1321

Pedlar, A., Kukula, M. J., Longley, D. P. T., et al. 1993, MNRAS, 263, 471

Quillen, A. C., Brookes, M. H., Keene, J., et al. 2006, ApJ, 645, 1092

Rakshit, S., Stalin, C. S., Hota, A., et al. 2018, ApJ, 869, 173

Reshetnikov, V. P., Mosenkov, A. V., Moiseev, A. V., et al. 2016, MNRAS, 461, 4233

Roche, N., & Eales, S. A. 2000, MNRAS, 317, 120

Ryon, J. E., & Stark, D. V. 2023, ACS Instrument Handbook for Cycle 32 v23.0 (STScI)

Sandage, A. 1966, ApJ, 145, 1

Sandage, A., & Bedke, J. 1994, The Carnegie Atlas of Galaxies (Carnegie Institution of Washington Publishing) No. 638

Sandage, A., & Tammann, G. A. 1987, A Revised Shapley-Ames Catalog of Bright Galaxies (2nd ed.; Carnegie Institution)

Sethi, S., Kuźmicz, A., Hunik, D., et al. 2025, A&A, 699, L4

Shimwell, T. W., Hardcastle, M. J., Tasse, C., et al. 2022, A&A, 659, A1

Shimwell, T. W., Röttgering, H. J. A., Best, P. N., et al. 2017, A&A, 598, A104

Shimwell, T. W., Tasse, C., Hardcastle, M. J., et al. 2019, A&A, 622, A1

Singh, V., Ishwara-Chandra, C. H., Sievers, J., et al. 2015, MNRAS, 454, 1556

Skrutskie, M. F., Cutri, R. M., Stiening, R., et al. 2006, AJ, 131, 1163

Smethurst, R., Beckmann, R., Simmons, B., et al. 2024, in EAS2024, European Astronomical Society Annual Meeting (EAS), 241

Smith, E. P., & Heckman, T. M. 1989, ApJS, 69, 365

Steiman-Cameron, T. Y., Kormendy, J., & Durisen, R. H. 1992, AJ, 104, 1339

Tadhunter, C. 2016, A&ARv, 24, 10

Tody, D. 1986, SPIE, 627, 733

Tody, D. 1993, ASPC, 52, 173

Tovmassian, H. M., & Yam, O. 2011, RMxAA, 47, 357

Tully, R. B., Pierce, M. J., Huang, J.-S., et al. 1998, AJ, 115, 2264

Turner, R. J., Yates-Jones, P. M., Shabala, S. S., et al. 2023, MNRAS, 518, 945

van Breugel, W., Heckman, T., Butcher, H., et al. 1984, ApJ, 277, 82

van Haarlem, M. P., Wise, M. W., Gunst, A. W., et al. 2013, A&A, 556, A2

Veron, P., & Veron-Cetty, M.-P. 1995, A&A, 296, 315

Véron-Cetty, M. P., & Véron, P. 2001, A&A, 375, 791

Vietri, A., Järvelä, E., Berton, M., et al. 2022, A&A, 662, A20

Wayth, R. B., Lenc, E., Bell, M. E., et al. 2015, PASA, 32, e025

Wong, O. I., Garon, A. F., Alger, M. J., et al. 2025, MNRAS, 536, 3488

Wright, E. L. 2006, PASP, 118, 1711

Wright, E. L., Eisenhardt, P. R. M., Mainzer, A. K., et al. 2010, AJ, 140, 1868

Wu, Z., Ho, L. C., & Zhuang, M.-Y. 2022, ApJ, 941, 95

Xanthopoulos, E., Thean, A. H. C., Pedlar, A., et al. 2010, MNRAS, 404, 1966

Yates-Jones, P. M., Shabala, S. S., & Krause, M. G. H. 2021, MNRAS, 508, 5239